EXPLORING PHYSICAL PROPERTIES OF NANOPARTICLES FOR BIOMEDICAL APPLICATIONS

by

RAJ KUMAR DANI

B.SC., TRIBHUVAN UNIVERSITY, KATHMANDU, NEPAL, 1998
M.SC., TRIBHUVAN UNIVERSITY, KATHMANDU, NEPAL, 2001

AN ABSTRACT OF A DISSERTATION

submitted in partial fulfillment of the requirements for the degree

DOCTOR OF PHILOSOPHY

Department of Chemistry
College of Arts and Sciences

KANSAS STATE UNIVERSITY
Manhattan, Kansas

2012

Abstract

The research work in this thesis aims at investigating the basic physic-chemical properties of magnetic and metal nanoparticles (NPs) for biomedical applications such as magnetic hyperthermia and controlled drug release.

Magneto-plasmonic properties of magnetic NPs are important to evaluate potential applications of these materials. Magnetic property can be used to control, monitor and deliver the particles using a magnetic field while plasmonic property allows the tracking of the position of the particles, but aggregation of NPs could pose a problem. Here, the aggregation of NPs is investigated via the Faraday rotation of gold coated Fe_2O_3 NPs in alternating magnetic fields. In addition, the Faraday rotation of the particles is measured in pulsed magnetic fields, which can generate stronger magnetic fields than traditional inductive heaters used in the previous experiments.

In the second project, the formation of protein-NPs complexes is investigated for hyperthermia treatment. The interactions between gold and iron-platinum NPs with octameric mycobacterial porin A from *Mycobacterium smegmatis* (MspA) and MspA^{cys} protein molecules are examined to assemble a stable, geometrically suitable and amphiphilic proteins-NPs complex.

Magnetic NPs show promising heating effects in magnetic hyperthermia to eliminate cancer cells selectively in the presence of alternating magnetic field. As a part of investigation, the heating capacity of a variety of magnetic NPs and the effects of solvent viscosity are investigated to obtain insight into the heating mechanism of these particles.

Finally, the controlled drug release of magnetic NPs loaded liposomes by pulsed magnetic field is investigated. The preliminary data indicate about 5-10% release of drug after the application of 2 Tesla magnetic pulses. The preliminary experiments will serve as the initial stage of investigation for more effective magnetic hyperthermia treatment with the help of short magnetic pulses.

EXPLORING PHYSICAL PROPERTIES OF NANOPARTICLES FOR BIOMEDICAL
APPLICATIONS

by

RAJ KUMAR DANI

B.SC., TRIBHUVAN UNIVERSITY, KATHMANDU, NEPAL, 1998
M.SC., TRIBHUVAN UNIVERSITY, KATHMANDU, NEPAL, 2001

A DISSERTATION

submitted in partial fulfillment of the requirements for the degree

DOCTOR OF PHILOSOPHY

Department of Chemistry
College of Arts and Sciences

KANSAS STATE UNIVERSITY
Manhattan, Kansas

2012

Approved by:

Major Professor
Prof. Dr. Viktor Chikan

Copyright

RAJ KUMAR DANI

2012

Abstract

The research work in this thesis aims at investigating the basic physic-chemical properties of magnetic and metal nanoparticles (NPs) for biomedical applications such as magnetic hyperthermia and controlled drug release.

Magneto-plasmonic properties of magnetic NPs are important to evaluate potential applications of these materials. Magnetic property can be used to control, monitor and deliver the particles using a magnetic field while plasmonic property allows the tracking of the position of the particles, but aggregation of NPs could pose a problem. Here, the aggregation of NPs is investigated via the Faraday rotation of gold coated Fe_2O_3 NPs in alternating magnetic fields. In addition, the Faraday rotation of the particles is measured in pulsed magnetic fields, which can generate stronger magnetic fields than traditional inductive heaters used in the previous experiments.

In the second project, the formation of protein-NPs complexes is investigated for hyperthermia treatment. The interactions between gold and iron-platinum NPs with octameric mycobacterial porin A from *Mycobacterium smegmatis* (MspA) and MspA^{cys} protein molecules are examined to assemble a stable, geometrically suitable and amphiphilic proteins-NPs complex.

Magnetic NPs show promising heating effects in magnetic hyperthermia to eliminate cancer cells selectively in the presence of alternating magnetic field. As a part of investigation, the heating capacity of a variety of magnetic NPs and the effects of solvent viscosity are investigated to obtain insight into the heating mechanism of these particles.

Finally, the controlled drug release of magnetic NPs loaded liposomes by pulsed magnetic field is investigated. The preliminary data indicate about 5-10% release of drug after the application of 2 Tesla magnetic pulses. The preliminary experiments will serve as the initial stage of investigation for more effective magnetic hyperthermia treatment with the help of short magnetic pulses.

Table of Contents

List of Figures

List of Tables

List of Abbreviations and symbols

1,2-dipalmitoyl-*sn*-glycero-3-phosphocholine	DPPC
1,2-distearoyl-*sn*-glycero-3-phosphocholine	DSPC
4-(2-hydroxyethyl)-1-piperazineethanesulfonic acid	HEPES
5(6)-Carboxyfluorescein	CF
Alternating current	AC
Anisotropy constant	K
Boltzmann constant	k_B
Brownian relaxation time	τ_B
Capacitance	C
Coercive force	H_C
Critical size	D_c
Curie temperature	T_C
Cysteine mutant of MspA	$MspA^{cys}$
Domain wall energy	E_{dw}
Dynamic light scattering	DLS
Effective relaxation time	τ
Electric field	E
Exciton Bohr radius	r_B
Faraday rotation	φ
Faraday rotation	FR
Frequency	f
Helium-Neon	He-Ne

High-Performance Liquid Chromatography		HPLC
Hydrodynamic volume		V_H
Hydroxylamine Hydrochloride		$NH_2OH.HCl$
Inductance	(Chapter 6)	L
Internal diameter		ID
Iron acetylacetonate		$Fe(acac)_2$
Length	(Chapter 2)	L
Lifetime	(Chapter 2)	τ
Localized surface plasmon resonance		LSPR
Loss power density		P
Magnetic field		B
Magnetic field strength		H
Magnetic hyperthermia		MHT
Magnetic resonance imaging		MRI
Magnetoliposomes		MLs
Maxwell Garnet		MG
Mercaptosuccinic acid		MSA
Multilamellar vesicles		MLV
Mycobacterium smegmatis		MspA
Nanoparticles		NPs
Néel relaxation time		τ_N
Néel temperature		T_N
Neutron activation analysis		NAA

Phase transition temperature	t_c
Phosphate buffered saline	PBS
Photoluminescence	PL
Platinum acetylacetonate	$Pt(acac)_2$
Polyethylene glycol	PEG
Quantum dots	Q-Dots
Quantum yield	Φ
Radiative decay engineering	RDE
Refractive index	n
Resistance	R
Resistor – Inductor – Capacitor	RLC
Resonance energy transfer	RET
Reticuloendothelial system	RES
Saturation magnetization	M_S
Sodium citrate	$Na_3C_6H_5O_7 \cdot 2H_2O$
Specific absorption rate	SAR
Specific heat capacity	C
Specific loss power	SLP
Surface Enhanced Raman Scattering Spectroscopy	SERS
Surface plasmon	SP
Surface Plasmon fluorescence Spectroscopy	SPFS
Surface plasmon resonance-enhanced magneto-optics	SuPREMO
Tetramethylammonium Hydroxide	TMAOH

Total Internal Reflection fluorescence Spectroscopy   TIRF

Transmission electron microscopy   TEM

Ultra-violet   UV

Unilamellar Vesicles   ULV

Verdet constant υ

Viscosity η

Wavelength λ

Acknowledgements

Ms. Lisa Percival, and Ms. Michelle Bergman) in the office for constantly providing help in all kinds of situations.

I am very much thankful to our departmental technicians, Jim Hodgson, Tobe Eggers, and Ron Jackson for fixing and engineering the necessary equipment whenever needed. I would like to thank all former and present group members: Dr. Naween Dahal, who synthesized some of the NPs (Fe/Pt II, CoAu, FeAu) that I used in my research, Dr. Pankaj Kanti Mandal, Dr. Pinar Dagatepe, Dr. Christopher Tuinenga, Santanu Roy, George Podaru, and Hongfu Luo for their co-operations.

I would like to thank to all my family and relatives. First and for most, I am grateful to my parents, Maiya Dani and Tilak Dani, for their unlimited and unconditional love, encouragement, support and guidance. I am really indebted to you. I am really grateful to my lovely son, Asmin Dani, for making me a cheerful dad. I am thankful to my brother, Ram Sharan Dani, and sister, Niru Dani, for their love and support.

Finally, I wish to thank all those helping hands who have been directly and indirectly involved in my course of study. Without them, I could not have completed this project. Funding agencies; National Science Foundation (NSF), the Kansas Bioauthority, Terry C. Johnson Center for Basic Cancer Research at KSU, National Institutes of Health, the State of Kansas and the Department of Chemistry at Kansas State University for their support on this work.

Dedication

To my parents

Mother Maiya Dani and Father Tilak Dani

To my lovely son

Asmin Dani

Chapter 1 - Introduction

Historical background

The term "nano" stands for dwarf in Greek, meaning very small. Quantitatively, it is a prefix for one billionth. For length, one nanometer means one billionth of a meter. By comparison, one nanometer is approximately 1/50,000 to 1/100,000 as thick as a human hair, or 3.5 atoms of gold lined up in a row equal 1 nm. All particles with at least one dimension between 1 to 100 nanometers fall in the category of nanoparticles (NPs). NPs have attracted great attention of scientists as they bridge bulk materials with atomic or molecular structures. The branch of science and engineering that deals with the design, the synthesis, the characterization, and the applications of NPs is called nanotechnology.[1] Nanotechnology is a new frontier in science and technology because existing materials can be stronger, lighter, and more durable when coupled with nanotechnology.[2]

Nanotechnology has the ability to work at the atomic and molecular level and it has been used by nature since the beginning of the evolution of biological species.[3] The history of artificial NPs by humans dates back to Roman times when they used noble metal NPs for decorative purposes.[4] A good example is "Lycurgus Cup", containing silver and gold bimetallic NPs of around 50-100 nm size and is currently at British Museum. This cup is red in color with transmitted light and is green in color with reflected light.[5] In the middle ages, a gold colloid that contains metallic gold with slightly pink color was known as "drinkable gold". This "drinkable gold" was described as "a solution where solid is present in such a degree of communication that it is not visible to the human eye" and were largely used to cure some diseases like dysentery, epilepsy, tumors and for the diagnosis of syphilis.[6] Later in 1857, Michael Faraday discovered

the first metallic gold colloidal solution while he was conducting research on the optical properties of gold. He described the various colors of gold particles by using different preparation methods.[7] However, the modern history of nanotechnology starts with a physicist, Richard P. Feynman. He shared his vision of "what very small things are and how they would behave" at the annual meeting of the American Physical Society (26th December, 1959) on his talk titled "There's Plenty of Room at the Bottom" and suggested to start from bottom or nano-level which is the key of the advancement of nanotechnology.[8]

Now scientists are eager to use NPs in chemistry, biology, medicine, engineering, and communication. NPs have significant application in drug and gene delivery,[9-14] magnetic resonance imaging (MRI),[15] magnetic hyperthermia (MHT),[16] protein detection,[17] cell labeling,[18] tissue engineering,[19] energy storage,[20] cosmetics,[21] photonics and telecommunication.[22]

Why nanoparticles?

As already mentioned, NPs have been utilized in the biomedical area because the size of NPs is smaller than cells (10-100 µm) and comparable with viruses (20-450 nm), proteins (5-50 nm) and genes (2 nm wide by 10-100 nm long).[23] It means that NPs can communicate closely with biomolecules and they can cross biological membranes and genes. Figure 1.1 shows the comparison of different NPs and cells and biological entities.
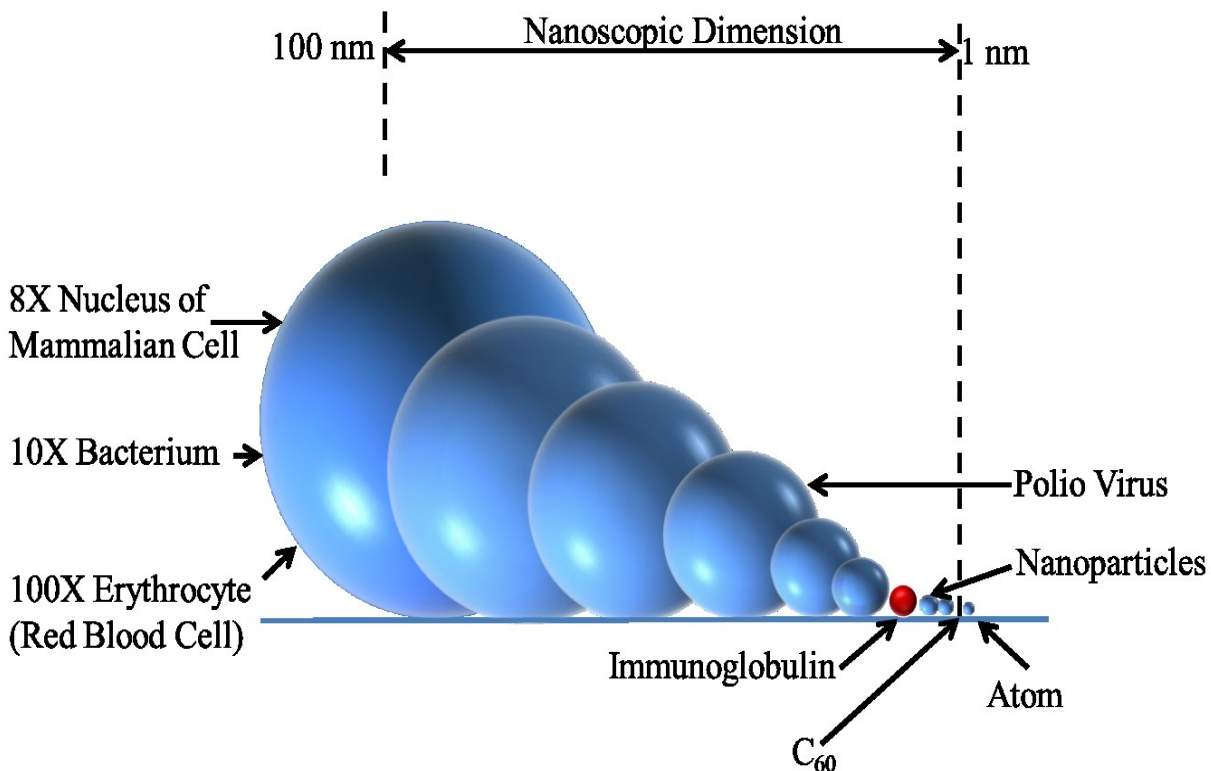
Figure 1.1 Comparison of sizes of atoms, nanoparticles and biological entities (reproduced from[24]).

The properties of NPs are interesting and sometimes exceptionally different from their counterpart atomic or bulk properties. In an average NP, the number of atoms ranges from few hundreds up to approximately a million.[25] This is a size regime where quantum chemistry and solid state physics meets. In the nano size, the material can exhibit properties from both phase regions. Quantum chemistry investigates chemical systems where the charge carriers are confined in the electrostatic potential of nuclei. On the other hand, solid state physics discusses infinitely large systems where these charged carriers could move as quasi free particles.

Regardless of size, bulk materials always have the same physical properties. The properties of NPs including optical, magnetic, specific heat, melting point and surface activities are size dependent, which make the NPs unique. At the nano-level, the fundamental electronic,

optical, magnetic, chemical and biological properties of a material are changed. NPs have very high surface area to volume ratio. This is because the surface area is the function of square of radius $(4\pi r^2)$ while volume the function of cube of radius $\left(\frac{4}{3}\pi r^3\right)$. For a typical NP, half or more atoms will on near the surface but in bulk, only a relatively small fraction of atoms will be near the surface. The calculated surface to bulk ratios of atoms versus size of a spherical NP is shown Figure 1.2, where around 50% of the atoms or ions are on the surface for 3 nm diameter particle.[26] These atoms provide more coordination sites and hence more probability to be manipulated easily so that they can achieve the required conditions to make them very reactive. Therefore, the surface plays a crucial role in determining the properties of the material.
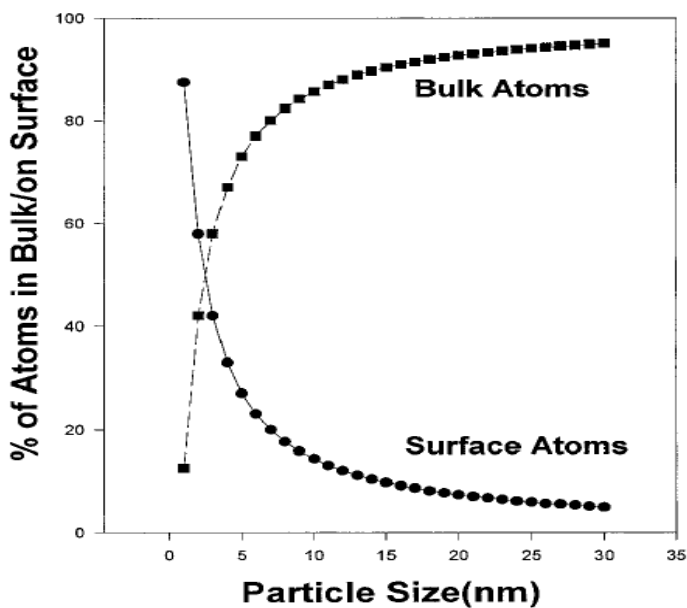
Figure 1.2 Calculated surface to bulk ratios of atoms versus size of a spherical NP.[26]

Not only the properties of NPs are different form their counterparts' atom and bulk materials but also depending on the nanoparticles' shape, size, and surface characteristics, properties of the nanoparticles of the same materials are not necessarily the same. Such distinct difference shows the importance of the study of properties of nanoparticles. NPs with different

features can be utilized for different purposes making the selection of NPs for a specific application crucial.

For magnetic hyperthermia (MHT), any magnetic NPs can produce heat when they are exposed to an alternating magnetic field. But any type of magnetic NPs cannot be used for MHT application. MHT needs non-toxic, biocompatible, superparamagnetic NPs with robust heating efficiency. Depending on the magnetic nature, size of NPs, biocompatibility, a suitable NP has to be chosen so that minimum amount of NPs will produce maximum required effect with minimal side effects. Same thing is true if NPs are used for the drug delivery. On the other hand, the imaging and sensing agents that used in biomedical application should exhibit good optical property. Plasmonic (noble metals) NPs show promising optical property. The combination of magnetic and plasmonic nanomaterial gives a different kind of NPs which is known as magneto-plasmonic NPs with both, magnetic and plasmonic, properties.

Overall, following properties are the reasons that NPs are being used in biomedical applications.

- Exhibit intermediate properties of both, atomic/molecular and bulk, regions
- Easy method of preparations with controllable sizes in nanometer range
- Tunable physical properties by adjusting composition, size and shape
- Suitable size to communicate closely with biomolecules and facilitate intimate interactions with cells and molecular constituents
- Easy to manipulate the surface property through surface modification and functionalization to make them biocompatible and detectable
- Magnetic property of NPs: superparamagnetism in magnetic materials for drug delivery, imaging, releasing heat

5

- Plasmonic property of NPs: dielectric confinement in plasmonic materials for detection and thermal ablation

The major types of the NPs and their properties that can be used in biomedical applications are discussed below.

Semiconductor nanoparticles

Quantum confined semiconductor NPs are also known as quantum dots (Q-Dots). Q-Dots were discovered by Louis E. Brus at Bell Labs[27] (now at Columbia University) in 1980 and he was awarded first Kavli Prize in Nanoscience in 2008 for his pioneering efforts in this field.[28] Quantum dots are semiconductor materials in the nano scale, normally in the size range of 1-20 nm. Most of the Q-Dots are composed of group II-VI and III-V elements of periodic table. Some examples of Q-Dots are CdSe (Cadmium Selenide), CdS (Cadmium Sulfide), CdTe (Cadmium Telluride), GaAs (Gallium Arsenide), InAs (Indium Arsenide) etc. Currently Q-Dots are being used in imaging, labeling, sensing,[29] solar cells.[30] Q-Dots promise to play a significant role in the technological industries in the future.[31] They have advantages over the conventional organic dyes.[14] They are an inherently new class of fluorescence probes and are able to provide bright, stable, and sharp fluorescence for use in many biological labeling applications. To stabilize and to reduce the toxicity of the Q-Dots, another semiconductor, like ZnS, with a wider band-gap is co-crystallized to form a shell over the core.

The energy gap between valence and conduction band (also known as the band gap) plays an important role in determining the properties of a solid. Any change in the gap significantly alters the properties of the material. Q-Dots can be excited over a broad range of wavelengths, and it is possible to choose an excitation radiation far from the emission peak resulting in large

Stokes shifts with high quantum yields.[32] For semiconductor NPs, the band gap depends on the size and chemical composition of NPs, since the spacing between adjacent conduction energy states is inversely proportional to the volume of the particle.[33] Well-controlled size and chemical composition of Q-Dots are able to manipulate fluorescence emission from the near-ultraviolet to the near-infrared via visible region with typically narrow, symmetric with a full-width at half max of 25-40 nm.[34] When semiconductor material absorbs light of a given photon energy (hv), a valence electron will be excited to the conduction band, leaving a hole in the conduction band. The hole (absence of an electron) is assumed to behave as a particle with specific effective mass with positive charge. The bound pair of electron-hole is known as exciton.[35] The physical separation of electron and hole is known as exciton Bohr radius(r_B) and can be calculated by using following expression[36]

$$r_B = \frac{\varepsilon \hbar^2}{\mu e^2}$$
1.1

where ε is the dielectric constant of the semiconductor and μ is the exciton reduced mass.

The calculated exciton Bohr radii of some selected semiconductors are tabulated in the following table 1.1.[37]

Materials	Exciton Bohr radius (r_B), nm
ZnO	1.8
ZnS	5.0
Si	5.5
CdSe	6.1
CdTe	10.0
PbS	20.4

CdS	31.5
InAs	34.0
PbSe	46.0
InSb	54.0

Table 1.1 Calculated value of exciton Bohr radii of some semiconductors.[37]

The value of r_B is very small compared to the size of a bulk semiconductor, allowing the exciton to move freely within the material. In case of Q-Dots, the value of r_B is comparable to the diameter of Q-Dots. Hence the exciton cannot move freely and quantum confinement of the exciton occurs. In quantum mechanics, quantum confinement is the phenomenon where a particle is captured in a potential space that is comparable to the wavelength of that particle. Here, the box is a 3D arrangement of the nuclei where the exciton consisting of an electron and a hole is confined. The confinement is strong when the diameter of Q-Dots is smaller than the exciton Bohr radius. When the diameter of Q-Dots is much larger than the exciton Bohr radius, the confinement is weak.[38]

According to Brus, the relationship between the size of Q-Dots and band gap energy is given by[35]

$$E_{g,QD} = E_{g,B} + \left(\frac{h^2}{8R^2}\right)\left(\frac{1}{m_e} + \frac{1}{m_h}\right) - \left(\frac{1.8e^2}{4\pi\varepsilon_0\varepsilon R}\right) \hspace{2cm} 1.2$$

, where $E_{g,QD}$ and $E_{g,B}$ are the band gap energies of the Q-Dots and bulk solid, R is the radius of Q-Dots, m_e and m_h are the effective mass of the electron and the hole in the valence band and in the conduction band, respectively, e is the elementary charge of the electron, h is the Plank's constant, ε is the dielectric constant of the solid, and ε_0 is the vacuum permittivity. The middle

term of the equation at right is the confinement term and the third term is the Columbic interaction term for electron-hole pairs that account for the increased relaxation of oppositely charged carriers in this confined space. The relationship between the Q-Dots size and the band gap of CdS is shown in the Figure 1.3.
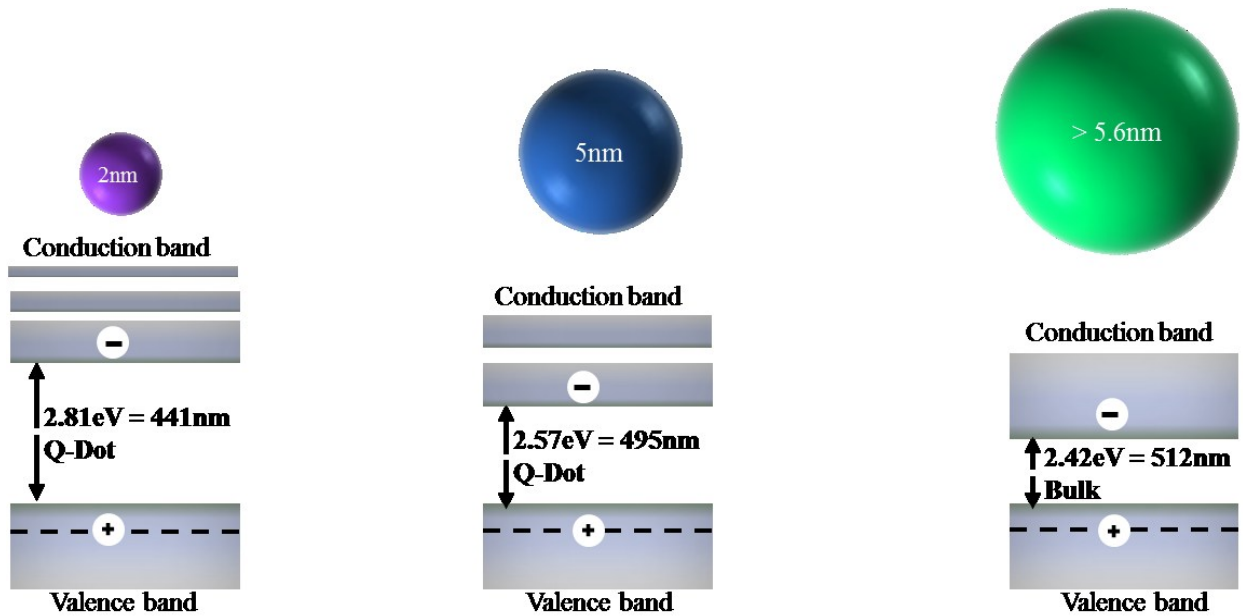
Figure 1.3 A schematic representation of the band structure CdS (reproduced from[35]).

Another consequence of effect of quantum confinement can also be seen in the density of states. Quantum confinement in Q-Dots converts a continuous band of allowed energy states of bulk semiconducting material into discrete energy states, which changes the density of states. The density of states is the number of energy states between energy E and $E + dE$, that is, the number of states per interval of energy levels which are available to be occupied by electrons. It indicates how densely the quantum states are packed in the material. The discreteness of the electronic energy state substantially changes the fundamental electronic and optical properties of reduced sized materials.[39] The average spacing of the energy level is characterized by the Kubo gap and is given by,

$$\delta = \frac{3E_f}{2N} \qquad\qquad 1.3$$

where E_f is the Fermi energy and N is the number of valence electrons in the nano-system. As the Kubo gap increases, the density of state decreases.

The number of states is crucial to determine the optical properties of the material. For a bulk semiconductor (3D), it is given by $E^{1/2}$ and is zero at the bottom and increases with increasing electron energy in the conduction band. In the quantum well (2D), the density of state is step function because of z-directional confinement and is in dependence of E. On the other hand, quantum wires (1D) are confined along a line and the density of state has a functional dependence of $E^{-1/2}$. Q-Dots are zero dimensional and their density of state is proportional to $\sum_{En} \delta(E - E_n)$ [38] and gives non-zero discrete energy value. These discrete values are responsible for sharp absorption and emission of Q-Dots. Density of states of electrons in one band of the semiconductor as a function of dimension is shown in the Figure 1.4.
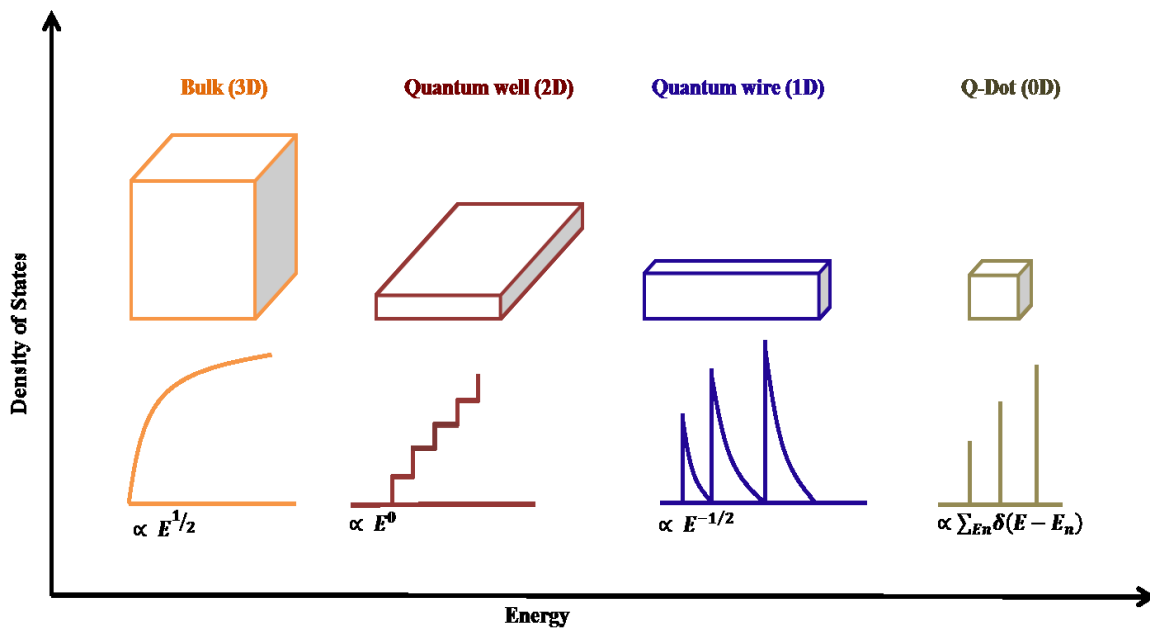
Figure 1.4 Density of states of electrons in one band of a semiconductor as a function of dimension (reproduced from[40]).

Plasmonic nanoparticles

Plasmonic nanoparticles are made of metals that show a special plasmonic property in UV-vis-near infrared region of the electromagnetic spectrum. Surface plasmons (SPs) are electromagnetic waves that are trapped on the surface because of their interaction with the free electrons of the metal. SPs can be either propagating, in planar bulk metal surface, or localized, in the case of NPs. Therefore, the surface plasmon resonance caused by NPs is also known as localized surface plasmon resonance (LSPR) and is not characterized by a wave vector.[38] The light incident on the NPs induces the conduction electrons in them to oscillate collectively (as shown in Figure 1.5) with a resonant frequency that depends on the NPs' size, shape, and composition, and the dielectric property of the surroundings. NPs of silver and gold are the most commonly used plasmonic materials. However, theoretically SP are possible with all metal, alloy or semiconductor with a large negative real dielectric constant and small imaginary dielectric constant.[41] Most metals exhibit plasmon resonance in the far ultraviolet region, but in case of Au, Ag, and Cu, there is a d→s interband transition (3d→4s in copper, 4d→5s in silver and 5d→6d in gold) that mixes with the plasmon resonance and shifts it to the visible region of the electromagnetic spectrum.[40]

11
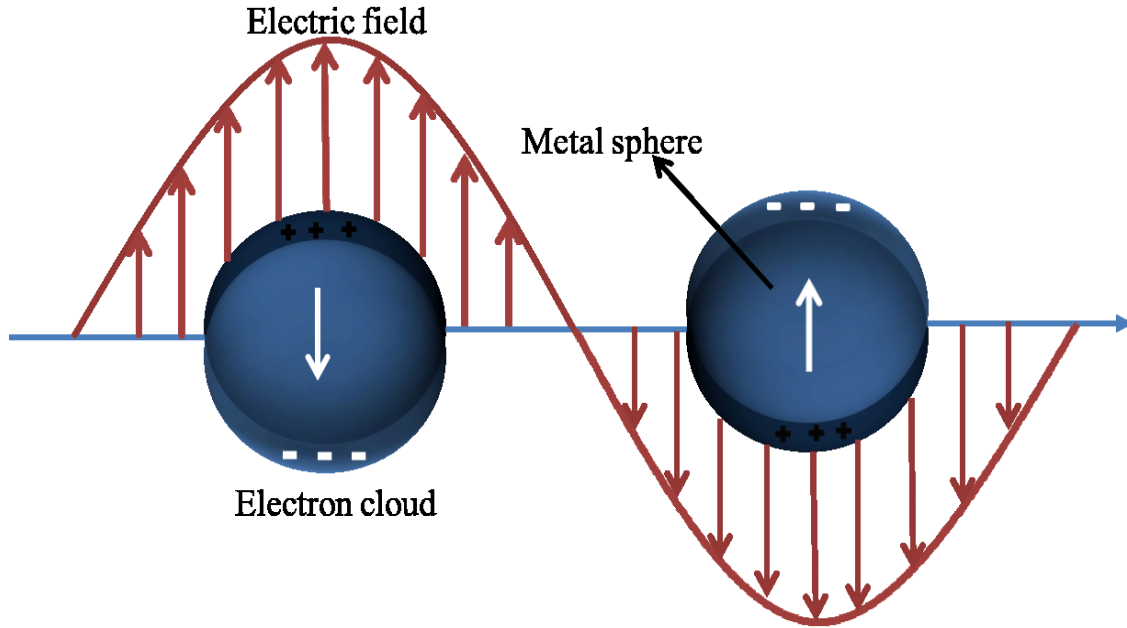
Figure 1.5 Schematic representation of plasmon oscillation for a sphere, showing the displacement of the conduction electron charge cloud relative to the nuclei (reproduced from[42]).

In early 1900s, Gustay Mei provided a theory to describe the scattering behavior of small spherical particles by solving Maxwell's equation for an electromagnetic light wave. For NPs much smaller than the wavelength of light (*2r ≪ λ*, or roughly *2r < λ/10*), only the dipole oscillation contributes significantly to the extinction cross-section (C_{ext}). The electrodynamic calculation of Mie theory for spherical particles gives[43]

$$C_{ext} = \frac{24\pi^2 r^3}{\lambda} \varepsilon_m^{3/2} \frac{\varepsilon_2}{(\varepsilon_1 + 2\varepsilon_m)^2 + \varepsilon_2^2} \qquad 1.4$$

where r is the radius of the particle, λ is the wavelength of the radiated light, ε_m is the dielectric constant of the surrounding medium, $\varepsilon = \varepsilon_1 + i\varepsilon_2$, is the complex dielectric constant of the particle. Whenever $\varepsilon_1 = -2\varepsilon_m$ is satisfied, a resonance peak appears. The surface plasmon resonance does not give rise to the most intense absorption for very small clusters but rather strongly damped and the absorption becomes weak and broad and absorption peak completely

disappears for NPs less than about 2 nm in diameter.[44] As the particles become smaller and smaller, the electrons reach the surface of the particles faster. Then the electrons can scatter on the surface and lose their coherence more quickly than in larger particles. As a result, the sharp plasmon band width increases with increasing particle size. Melikyan *et al;*[45] have tried to interpret the damping of the SP using the electron-phonon interaction. According to their claim, the radiation damping of SP plays an insignificant role because radiation damping is proportional to the number of electrons in the metallic NP. So, relatively larger NP is necessary to flow the energy out. The resonant coupling of SP oscillations with electronic transitions in the matrix is responsible for SP damping in small clusters. A typical experimental result of damping of plasmon of gold nanoparticle is shown in Figure 1.6.
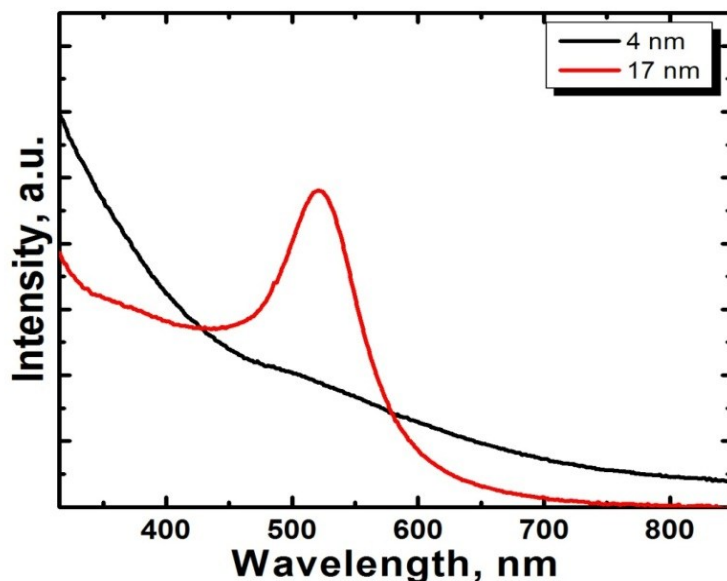
Figure 1.6 Damping of plasmon of gold NP as the size of nanoparticles decrease.

Furthermore, rod shaped NPs have two resonances; one due to plasmon oscillation along the short axis and another due to the plasmon oscillation along the long axis, which strongly depends

on the length to width (aspect) ratio. If the aspect ratio is increased, the long axis SP wavelength position shifts from the visible to near infra-red region.[46]

The LSPR also critically depends on the refractive index of the medium. From an experimental point of view, to measure the effect of changes in the refractive index of the medium into the LSPR is more complicated because of the very high susceptibility of the NPs to flocculate in solvent. However, there are some studies on gold colloids and on gold /silver colloids.[47, 48] The shift in SP with refractive index is approximately described as[41]

$$\Delta\lambda \approx m(n_{adsorbate} - n_{medium})\left(1 - e^{-\frac{2d}{l_d}}\right) \qquad 1.5$$

where m is the sensitivity factor, $n_{adsorbate}$ and n_{medium} are the refractive indices of the adsorbate and the medium surrounding the NP, respectively, d is the effective thickness of the adsorbate layer, and l_d is the electromagnetic field decay length. The shift could be manipulated by manipulating the NPs characteristic properties l_d, m, and even Δn. The variation of color of gold colloids with respect to their refractive indeces is shown in the following Figure 1.7.

Figure 1.7 Gold colloids in different refractive indices (1.336, 1.407, 1.481, 1.525, 1.583 respectively) of solution using mixtures of butyl acetate and carbon disulfide with water.[47]

The surface plasmon resonance and related phenomena in metallic nanostructures are currently being utilized for many applications including molecular sensing and tagging, near-field optical microscopy, subwavelength photonics, optical materials, immunoassays, biochemical sensors and surface-enhanced spectroscopies.[41, 49] Surface enhanced spectroscopy combines the excitation of a surface plasmon mode as an interfacial light source[50] with the well-established detection schemes of fluorescence spectroscopy. A chromophore close (within the decay length of evanescent field for excitation) to a surface can be excited by the evanescent wave. Surface Plasmon fluorescence Spectroscopy (SPFS), Total Internal Reflection fluorescence Spectroscopy (TIRF), Surface Enhanced Raman Scattering Spectroscopy (SERS) are the examples where surface plasmons are used to excite chromophores. The resonating surface plasmons excite the chromophores that are attached to the analyte and the emitted fluorescence are measured. SERS depends on enhancement of the Raman scattering (exchange of energy between photons and molecular vibration) by electromagnetic fields near the surface of the plasmonic materials due to the presence of surface plasmon. The Raman scattering of a single molecule is observed with enhancement of the scattering cross section by factor up to 10^{14} which shows the importance of surface plasmon in spectroscopic technique.[51] The basic principle[52] of TIRF is the surface-associated evanescent electromagnetic field that is created when light is internally reflected at a planar interface between two transparent materials with different refractive indices. In TIRF, an evanescent wave is formed at dielectric interface by total internal reflection and the chromophore is excited in the penetration depth of the evanescent wave. This provides an extremely high penetration depth resolution that is not achieved in confocal imaging microscopy.[53]

Magnetic nanoparticles

Metallic NPs that show magnetic behavior are defined as the magnetic NPs. Magnetic NPs are abundant in nature, in the human brain, in bacteria, algae, birds, ants, bees[54-56] and are also found in many biological objects.[57] Interestingly, some vertebrates use nanoparticle-assisted natural navigation system for their long distance migration.[58] Nanoscale magnetic NPs are of interest for applications in ferrofluids, high density magnetic storage, high-frequency electronics, high-performance permanent magnets, magnetic refrigerants etc.[59] The intrinsic magnetic properties of bulk magnetic materials like saturation magnetization (M_S), Coercive force (H_C), and Curie temperature (T_C) depend only on chemical and crystallographic structures. The shape and the size of the bulk material are not crucial to determine the magnetic property. On the other hand, the properties of magnetic NPs not only depend on size and shape but also depend on chemical composition, type and degree of defects of the crystal lattice, interaction of the particles with the surrounding materials and the neighbor particles.[60] Magnetic NPs show different properties from their counterparts atom and bulk materials because these NPs have very high magnetic anisotropy with different Néel (T_N), and Curie (T_C) temperatures. By tuning all the properties mentioned above, properties of the magnetic NPs can be manipulated. Depending upon the properties of the magnetic materials, they can be classified into different classes. Diamagnetic materials have negative susceptibility and show weak repulsion with the external magnetic field while in paramagnetic materials, the magnetic moments are randomly orientated due to the thermal fluctuations. When a magnetic field is applied these randomly orientated magnetic moments start to align parallel to the field. Hence, paramagnetic materials are weakly attracted to the external magnetic field. They exhibit small and positive susceptibility. Ferromagnetic materials such as iron, cobalt, nickel, have higher tendency to align with the applied magnetic

field and they are highly attracted towards the applied external magnetic field. They have very high positive magnetic susceptibility and show hysteresis. Diamagnetic and paramagnetic materials do not show any magnetic properties when the applied external magnetic field is removed. They show a linear response with the applied magnetic field. Ferromagnetic materials remain magnetized even after the removal of the external magnetic field.

When the size of the ferromagnetic materials decreases to a limit, they are no longer able to show ferromagnetic properties. This transition introduces another property known as superparamagnetism. A superparamagnetic material consists of small particles of ferromagnetic material and is able to flip direction of its spin due to thermal fluctuations. As a result, superparamagnetic materials show magnetic properties only in the presence of magnetic field. When the magnetic field is removed, thermal energy disrupts the magnetic moment of the material. For superparamagnetic particles, the net magnetic moment is zero in the absence of magnetic field. When a magnetic field is applied, there will be a net statistical alignment of magnetic moments which is analogous to paramagnetism, except the magnetic moment is not that of a single atom, but for a single domain and a single domain contains thousand to millions of atoms. Hence the term superparamagnetism is used, which denotes a much higher susceptibility value than that for simple paramagnetism.

Superparamagnetism can be understood considering single-domain particles. The magnetic anisotropy energy of a particle is responsible for holding magnetic moment along the certain direction and is given by $E(\theta) = KVsin^2\theta$ where K is the anisotropy constant, V is the volume of the particle, and θ is the angle between the direction of magnetization and the easy axis. The energy barrier KV separates the two energetically equivalent easy directions of magnetization.[61] With decreasing particle size, the thermal energy, k_BT, exceeds the energy

17

barrier, *KV*, (as shown in Figure 1.8) and the magnetization is easily flipped the direction then it shows the superparamagentic behavior.
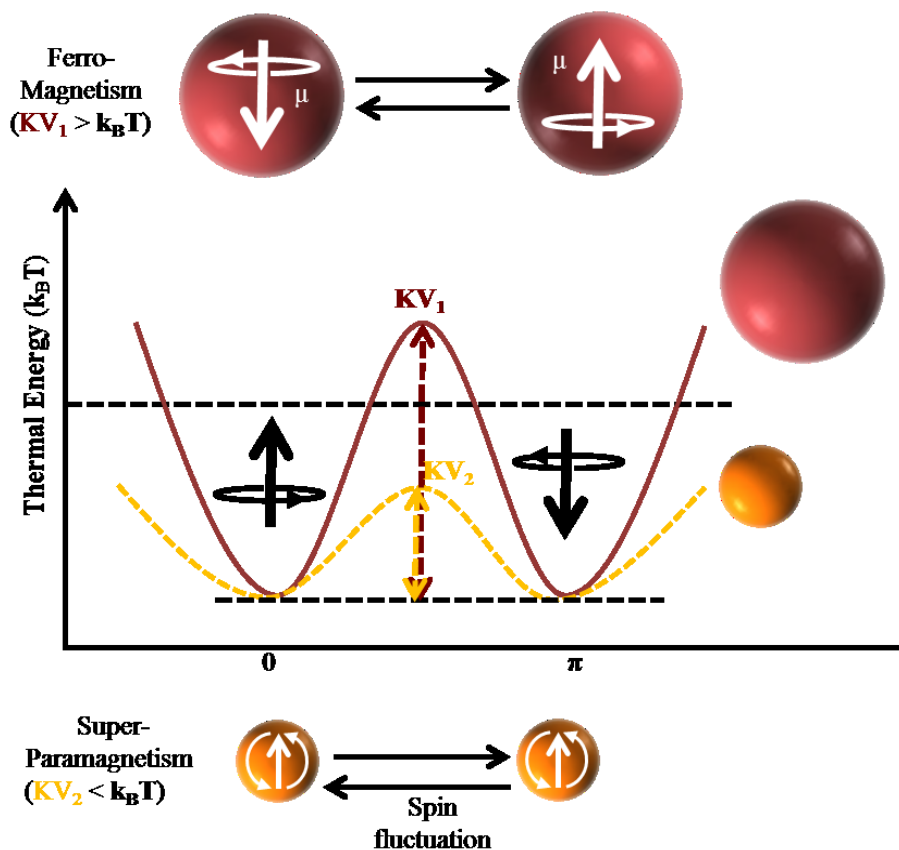
Figure 1.8 Energy diagram of magnetic nanoparticles with different magnetic spin alignment, showing ferromagnetism in a large particle and superparamagnetic in a small nanoparticle (reproduced from[62]).

The size below which magnetic materials show superparamagnetic behavior is called critical size (D_c). The critical size depends on the saturation magnetization of the particles, anisotropy energy, and exchange interactions between individual spins.[63] Ferromagnetic materials contain number of small magnetic regions and are called magnetic domains. The boundaries between the domains are called domain walls. In large NPs, energetic considerations favor the formation of a domain wall but when the size decreases below a certain level, the

formation of domain walls becomes unfavorable. The multi-domain state is energetically favorable if the energy consumption for the formation of domain walls is lower than the difference between the magnetostatic energies (ΔE_{MS}) of the single-domain and multi-domain states. When an external magnetic field is applied, creation, extinction and growth of domain size may happen.[64] The creation of domain depends on the magnetostatic energy and the domain wall energy(E_{dw}). When the size of the materials decreases, the number of domain walls per unit area increases which is energetically unstable and force the material into a single domain configuration. The size below which the materials exist in a single domain is determined by the above mentioned two energies. ΔE_{MS} increases with volume of the material and E_{dw} increases with the interfacial area between domains. When these two energies become equal, then the following relation holds for critical size, D_c,[61]

$$D_c \approx 18\frac{\sqrt{AK}}{\mu_0 M_s^2} \hspace{4cm} 1.6$$

where A is the exchange constant, K is the anisotropy constant, μ_0 is the vacuum permeability and M_s is the saturation magnetization. Typical values of D_c for some important magnetic materials are listed in the following table 1.2.

Materials	M_s [#], (emu/g)	D_c [##], (nm)
Iron (α-Fe)	217.9	7-11
Nickel	57.5	~110
Cobalt	162.7	~60
Magnetite, Fe_3O_4	91.6	20-30
$CoFe_2O_4$	80.8	40
Hematite, α-Fe_2O_3	~1	13

NdFeB	171	~300
SmCo₅	164	750
BaFe₁₂O₁₉	72	900

at room temperature   ## for spherical particles

Table 1.2 Estimated single-domain size for different spherical magnetic particles.[64]

The relationship between magnetization and the applied magnetic field gives a hysteresis loop. The different types of magnetic materials give different types of hysteresis loops.
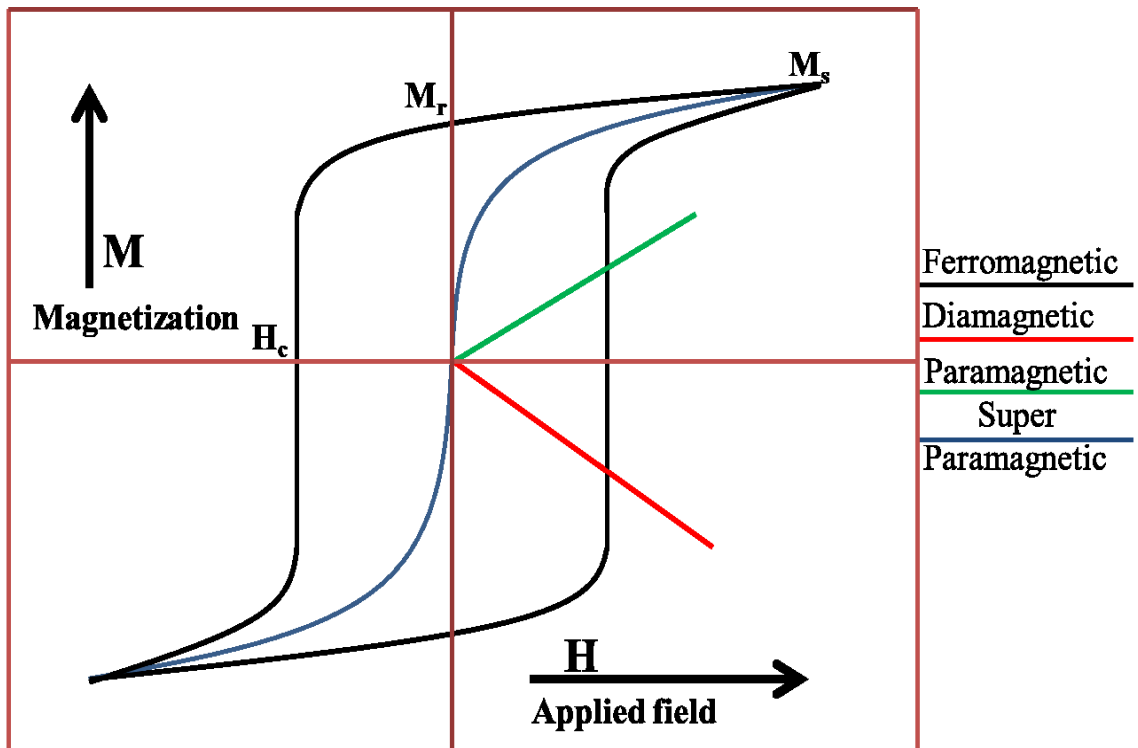
H_c is coercive force, M_r is magnetization remanence, M_s is saturation magnetization

Figure 1.9 Hysteresis of different magnetic materials.[65]

Magnetization is reversed by the movement of domain wall in ferromagnetic materials, but in superparamagnetic materials the reversal is due to the spin rotation of the magnetic moment. Superparamagnetism is useful in biomedical application because as the applied

magnetic field is removed, if magnetization disappears then there will be no agglomeration of NPs. The superparamagnetic behavior can be characterized in terms of a relaxation time, τ, which is the time it take the system to achieve zero magnetization after the removal of the external magnetic field. The relaxation time, τ, for a particle is given by Néel expression:[66]

$$\tau = \tau_0 exp\left(\frac{\Delta E}{k_B T}\right) \hspace{4cm} 1.7$$

where τ_0 is the characteristic time of the order 10^{-10} to 10^{-12} s for non-reacting particles and weakly depends on temperature, ΔE (= KV) is the energy barrier to moment reversal, and $k_B T$ is the thermal energy. If the particle magnetic moment reverses at times shorter than the experimental time scales, the system is in superparamagnetic state, if not, it is in the so-called blocked state. The temperature, which separates these two states, is so-called the blocking temperature, T_B.[61]

Area of Research Project

The main focus of this research is to explore some of the properties of nanoparticles that can be used in biomedical applications. Following are the outline of the research.

Enhanced Faraday rotation of gold coated Fe$_2$O$_3$ NP in alternating and pulsed magnetic field:

In this thesis, a magnetic material has been used to achieve magneto-optical and high-frequency devices such as an isolator, a circulator, and so on. To increase the effectiveness of such devices, the magneto-optical effect of the magnetic material needs to be improved. One of the prospective methods to enhance the magneto-optical effect is to utilize surface plasmon resonance[67] by incorporating plasmonic material on to the surface of magnetic materials. Such materials act as multi-component hybrid NPs. Multi-component hybrid NPs are composed of multi-components

and they can exhibit several functions for applications that are difficult or even impossible to achieve from single-component NPs.[68] A thin shell of gold coated Fe_2O_3 core is one good example of a multi-component hybrid nanoparticle. The thin shell of gold not only provides a relatively passive surface but also provides strong plasmon resonance on the magnetic material Fe_2O_3. Plasmon allows light to be localized on length scales much shorter than its wavelength, which makes it possible to integrate photonics and electronics on the nano-scale. Magneto-optical materials are appealing for applications in plasmonics because they open up the possibility of using external magnetic fields in plasmonic devices.[69] In magneto-plasmonic material, plasmon resonance is used to track the position of the individual nanoparticles, and the magnetic material is used to control, monitor, and deliver the particles to the certain place under a large magnetic field gradient. Therefore, the study of magneto-optical properties of such magneto-plasmonic material is one of the main areas of research. In our research, alternating magnetic field is used to investigate the enhanced Faraday rotation of magneto-plasmonic NPs (Fe_2O_3/Au Core-Shell). The study of enhanced Faraday rotation of gold coated Fe_2O_3 (a magneto-plasmonic) and aggregation analysis are done experimentally. The surface plasmon enhanced Faraday rotation of gold shell coated Fe_2O_3 NPs is calculated theoretically as well. This will be discussed in chapter 3. In chapter 4, Faraday rotation of gold and a thin gold shell coated Fe_2O_3 NPs in pulsed magnetic field will be discussed. In pulsed magnetic field, a strong magnetic field could be achieved and measurement using strong magnetic field would provide wider and sensitive data that cannot be obtained in low alternating magnetic field.

Interaction of different types of nanoparticles (gold, iron platinum) with
macromolecules (MspA):

Combining nanoparticles with macromolecules, like nanometer sized protein, is desirable to extend the functionality and transferability of both protein and nanoparticles. Several groups have been working to create the nanoparticle/biomacromolecule complex,[70-72] but challenges remain because when nanoparticles form the complex with proteins, the proteins lose their natural environment. Due to this, proteins lose their structural properties and limit potential uses of these complexes. To address some of the concerns of such type of complex formation, octameric porin A from *Mycobacterium smegmatis* (MspA) is used to form complexes with gold and iron-platinum NPs. The detail will be discussed in chapter 5.

Heating efficacy of magnetic nanoparticles in presence of alternating magnetic field:

Magnetic NPs can be used in magnetic hyperthermia application in which tumor cells are selectively killed using alternating magnetic field. When colloidal magnetic NPs are placed in alternating magnetic field, they convert magnetic energy into the heat energy. In case of single-domain NPs, Néel relaxation together with Brownian relaxation is responsible for the production of heat. Néel relaxation largely depends on the anisotropy energy of the material and Brownian relaxation depends on the carrier viscosity of the medium. In any case, a large heating power of the material is desirable[73] in order to reduce the amount of material to be used to the patients. In order to use NPs for clinical applications, the heating effect of different NP needs to be understood. Because heating capability of NPs depends on number of factors like size, size distribution, shape, bulk and surface chemical compositions, frequency and amplitude of the magnetic field, viscosity of the carried medium.[23] In our experiment, almost equal size of different NPs (two types of Fe/Pt, CoAu, and FeAu) are used to evaluate their heating capacity.

To study the viscosity dependent heating capacity of magnetic NPs, commercially available Fe$_3$O$_4$ (EMG 707) is used. The detail will be discussed in chapter 6.

Magnetoliposomes for magnetic field triggered control drug release:

Liposomes (vesicles formed by amphiphilic phospholipid molecules in water) have already been known as drug carrier for a long time because of unique surface chemical property of lipids that can be modified with specific ligands.[74, 75] Among several promising new drug delivery system, liposomes represent an advanced technology to deliver a load to the site of action. Drugs can be entrapped either in the inner aqueous or in the lipid bilayers, depending on the relative hydrophobicity to hydrophilicity ratio. Water soluble (polar) components are entrapped inside the core and oil soluble (non-polar) components are entrapped between the bilayers.[76] By combining liposomes with magnetic NPs, known as magnetoliposomes (ML), the flow of liposomes could be manipulated effectively using external magnetic field gradient. In our experiment, an effort is made to prepare ML and to optimize the drug release using different types of superparamagnetic NPs (hydrophobic, hydrophilic, amphiphilic) under the influence of pulsed magnetic field. The detail will be discussed in chapter 7.

References

1.   Salata, O., *Journal of Nanobiotechnology* **2004,** *2:3*.

2.   Valiev, R., *Nature* **2002,** *419* (6910), 887-+.

3.   Kasemo, B., *Current opinion in solid state & materials science* **1998,** *3* (5), 451-459.

4.   Giljohann, D.; Seferos, D.; Daniel, W.; Massich, M.; Patel, P., *Angewandte Chemie (International ed. in English) 49* (19), 3280-3294.

5.   Freestone, I.; Meeks, S.; Higgitt, C., *Gold Bull.* **2007,** *40* (4), 270-277.

6.   Daniel, M. C.; Astruc, D., *Chem. Rev. (Washington, DC, U. S.)* **2004,** *104* (1), 293-346.

7.   Tweney, R. D., *Perspectives on Science* **2006,** *14* (1), 97-121.

8.   Feynman, R. P., *Journal of Microelectromechanical Systems* **1992,** *1* (1), 60-66.

9.   Riviere, C.; Roux, S.; Tillement, O.; Billotey, C.; Perriat, P., *European journal of control* **2006,** *31* (3), 351-367.

10.   R, D., *Wiley interdisciplinary reviews. Nanomedicine and nanobiotechnology* **2009,** *1* (6), 583-609.

11.   Portney, N. G. N. G. G., *Anal. Bioanal. Chem.* **2006,** *384* (3), 620-30.

12.   Kumar, C. S. S. R.; Mohammad, F., *Adv. Drug Delivery Rev. 63* (9), 789-808.

13.   Goldberg, M., *Journal of biomaterials science. Polymer edition* **2007,** *18* (3), 241-268.

14.   Ghaderi, S.; Ramesh, B.; Seifalian, A., *J. Drug Targeting 19* (7), 475-486.

15.   De, M., *Adv. Mater. (Weinheim, Ger.)* **2008,** *20* (22), 4225-4241.

16.   Mohammad, F., *The journal of physical chemistry. C 114* (45), 19194-19201.

17.   Nam, J. M.; Thaxton, C. S.; Mirkin, C. A., *Science* **2003,** *301* (5641), 1884-1886.

18.   Singh, R.; Nalwa, H., *J. Biomed. Nanotechnol.* **2011,** *7* (4), 489-503.

19.   De Santis, R.; Gloria, A.; Russo, T.; D'Amora, U.; Zeppetelli, S., *J. Appl. Polym. Sci.* **2011,** *122* (6), 3599-3605.

20.   Rakhi, R. B.; Alshareef, H. N., *J. Power Sources* **2011,** *196* (20), 8858-8865.

21.   Andreani, T.; Doktorovova, S.; Lopes, C. M.; Souto, E. B., *International Journal of Nanotechnology* **2011,** *8* (1/2), 66-83.

22.   Barnes, W. L.; Dereux, A.; Ebbesen, T. W., *Nature* **2003,** *424* (6950), 824-830.

23.   Duguet, E.; Vasseur, S.; Mornet, S.; Devoisselle, J.-M., *Nanomedicine* **2006,** *1* (2), 157-168.

24.   Gu, H.; Xu, K.; Xu, C.; Xu, B., *Chem. Commun. (Cambridge, U. K.)* **2006,** (9), 941-949.

25.   Klabunde, K. J., *Nanoscale Materials in Chemistry*. John Wiley & Sons: 2001.

26.   Klabunde, K. J.; Stark, J.; Koper, O.; Mohs, C.; Park, D. G., *J. Phys. Chem.* **1996,** *100* (30), 12142-12153.

27.   Bogue, R., *Sensor Review* **2010,** *30* (4), 279-284.

28.   *Nat. Nanotechnol.* **2010,** *5* (6), 381-381.

29.   Medintz, I. L., *Nat. Mater.* **2005,** *4* (6), 435-46.

30.   Kim, J.; Choi, H.; Nahm, C.; Moon, J.; Kim, C., *J. Power Sources* **2011,** *196* (23), 10526-10531.

31.   Pickett, N. L.; O'Brien, P., *Chem. Rec.* **2001,** *1* (6), 467-479.

32.   Goldman, E. R.; Uyeda, H. T.; Hayhurst, A.; Mattoussi, H., Luminescent Biocompatible Quantum Dots: A Tool for Immunosorbent Assay Design. In *Quantum Dots Applications in Biology*, Bruchez, M. P.; Hotz, C. Z., Eds. Humana Press Inc.: Totowa, New Jersey, 2007.

33.   Halperin, W. P., *Reviews of Modern Physics* **1986,** *58* (3), 533-606.

34.   JianBo, L.; XiaoHai, Y.; XiaoXiao, H.; KeMin, W.; Qing, W., *SCIENCE CHINA Chemistry* **2011,** *54* (8), 1157-1176.

35.   Mansur, H., *Wiley interdisciplinary reviews. Nanomedicine and nanobiotechnology 2* (2), 113-129.

36.   Burda, C., *Chem. Rev. (Washington, DC, U. S.)* **2005,** *105* (4), 1025-1102.

37.   Fahlman, B. D., *Materials Chemistry*. Springer Science: 2007.

38.   Prasad, P. N., *Nanophotonics*. Wiley - Interscience: 2004.

39.   Alivisatos, A. P., *Science* **1996,** *271* (5251), 933-937.

40.   Choi, C.; Alivisatos, A. P., *Annu. Rev. Phys. Chem.* **2010,** *61* (1), 369-389.

41.   Anker, J.; Hall, W. P.; Lyandres, O.; Shah, N.; Zhao, J., *Nat. Mater.* **2008,** *7* (6), 442-453.

42.   Kelly, K. L.; Coronado, E.; Zhao, L. L.; Schatz, G. C., *J. Phys. Chem. B* **2003,** *107* (3), 668-677.

43.   Hu, M.; Chen, J.; Li, Z.-Y.; Au, L.; Hartland, G., *Chem. Soc. Rev.* **2006,** *35* (11), 1084-1094.

44.   Link, S.; El Sayed, M. A., *Int. Rev. Phys. Chem.* **2000,** *19* (3), 409-453.

45.   Melikyan, A.; Minassian, H., *Applied physics. B, Lasers and optics* **2004,** *78* (3-4), 453-455.

46.   Mody, V. V.; Siwale, R.; Singh, A.; Mody, H. R., *J. Pharm. Bioallied. Sci.* **2010,** *2* (4), 282-289.

47.   Underwood, S.; Mulvaney, P., *Langmuir* **1994,** *10* (10), 3427-3430.

48.   Chumanov, G.; Sokolov, K.; Gregory, B. W.; Cotton, T. M., *J. Phys. Chem.* **1995,** *99* (23), 9466-9471.

49.   Yu, E. T.; Derkacs, D.; Lim, S. H.; Matjeu, P.; Schaadt, D. M., *Plasmonics: Nanoimaging, Nanofabrication, and Their Applications IV* **2008,** *7033*, 70331V-1-70331V-9.

50.   Knoll, W.; Yu, F.; Neumann, T.; Niu, L.; Schmid, E. L., Principles and Applications of Surface-Plasmon Field-Enhanced Fluorescence Techniques. In *Radiative Decay Engineering*, Geddes, C. D.; Lakowicz, J. R., Eds. Springer: New York, 2005.

51.   Maier, S. T., *Plasmonics: Fundamentals and Applications*. Springer: 2007.

52.   Thompson, N. L.; Pero, J. K., Total Internal Reflection Fluorescence Microscopy: Applications in Biophysics. In *Fluorescence Spectroscopy in Biology*, Hof, M.; Hutterer, R.; Fidler, V., Eds. Springer: 2005.

53.   Kim, K.; Kim, D.; Cho, E.-J.; Suh, J.-S.; Huh, Y.-M., *Nanotechnology* **2008,** *20* (1), 015202.

54.   Wiltschko, R.; Wilschko, W., *Magnetic Orientation in Animals*. Springer, Berlin 1995.

55.   Kirschvink, J. L., *Bioelectromagnetics* **1989,** *10*, 239.

56.   Stokroos; Litinetsky, L.; Ishay, J. S., *Nature* **2001,** *411* (6838), 654-654.

57.   Frankel, R. B.; Blakemore, R. P.; Wolfe, R. S., *Science* **1979,** *203* (4387), 1355-1356.

58.   Walker, M. M.; Diebel, C. E.; Haugh, C. V.; Pankhurst, P. M.; Montgomery, J. C., *Nature* **1997,** *390* (6658), 371-376.

59.   Koksharov, Y. A., Magnetism of Nanoparticles: Effect of Size, Shape, and Interactions. In *Magnetic Nanoparticles* Gubin, S. P., Ed. WILLEY-VCH: 2007.

60.   Gubin, S. P.; Koksharov, Y. A.; Khomutov, G. B.; Yurkov, G. Y., *Russ. Chem. Rev.* **2005,** *74* (6), 489-520.

61.   Lu, A.-H.; Salabas, E. L.; Schueth, F., *Angewandte Chemie (International ed. in English)* **2007,** *46* (8), 1222-1244.

62.   Jun, Y. W.; Seo, J. W.; Cheon, J., *Acc. Chem. Res.* **2007,** *41* (2), 179-189.

63.   Batlle, X.; Labarta, A., *Journal of Physics D-Applied Physics* **2002,** *35* (6), R15-R42.

64.   Goya, G. F.; Grazu, V.; Ibarra, M. R., *Current nanoscience* **2008,** *4* (1), 1-16.

65.   Arruebo, M.; Fernandez Pacheco, R.; Ibarra, M. R.; Santamaria, J., *Nano Today* **2007,** *2* (3), 22-32.

66.   Pankhurst, Q. A.; Connolly, J.; Jones, S. K.; Dobson, J., *Journal of physics. D, Applied physics* **2003,** *36* (13), R167-R181.

67.   Uchida, H.; Masuda, Y.; Fujikawa, R.; Baryshev, A. V.; Inoue, M., *J. Magn. Magn. Mater.* **2009,** *321* (7), 843-845.

68.   Peng, S.; Lei, C.; Ren, Y.; Cook, R.; Sun, Y., *Angewandte Chemie (International ed. in English)* **2011,** *50* (14), 3158-3163.

69.   Belotelov, V. I.; Akimov, I. A.; Pohl, M.; Kotov, V. A.; Kasture, S., *Nat. Nanotechnol.* **2011,** *6* (6), 370-376.

70.   Mukherjee, P.; Ahmad, A.; Mandal, D.; Senapati, S.; Sainkar, S. R., *Nano Lett.* **2001,** *1* (10), 515-519.

71.   Katz, E.; Willner, I., *Angewandte Chemie (International ed. in English)* **2004,** *43* (45), 6042-6108.

72.   Niemeyer, C. M., *Angewandte Chemie (International ed. in English)* **2001,** *40* (22), 4128-4158.

73.   Hergt, R.; Andra, W.; d'Ambly, C. G.; Hilger, I.; Kaiser, W. A., *IEEE Trans. Magn.* **1998,** *34* (5), 3745-3754.

74.   Elersic, K.; Pavlic, J. I.; Iglic, A.; Vesel, A.; Mozetic, M., *Chem. Phys. Lipids* **2012,** *165*, 120-124.

75.   Sen, T.; Sheppard, S. J.; Mercer, T.; Elhissi, A., *NSTI-Nanotech* **2010,** *1*, 924-927.

76.   Sharma, A.; Sharma, U. S., *Int. J. Pharm.* **1997,** *154*, 123-140.

Chapter 2 - Experimental techniques

For the research described in this thesis, two important methodologies have been used, photoluminescence (PL) spectroscopy and Faraday rotation (FR) spectroscopy. To investigate the complex formation between metal nanoparaticles and MspA, photoluminescence (PL) spectroscopy is used. In addition to PL spectroscopy, the optical properties of nanoparticles (Fe_2O_3/Au core shell, Fe_2O_3, Au) are investigated by Faraday rotation spectroscopy.

Photoluminescence (PL) spectroscopy

Photoluminescence is the spontaneous emission of light from a given substance from its electronically excited state to its ground state. Photoluminescence spectroscopy is a spectrochemical technique and is widely used to study molecules including peptides and proteins. The aromatic amino acids, tryptophan, tyrosine, and phenylalanine offer intrinsic fluorescent probes of protein conformation, dynamics, and intermolecular interactions.[1] In a typical photoluminescence study, a sample is excited at certain wavelength of light then PL light is collected at different wavelength. The emission spectrum provides both qualitative and quantitative information of the sample. A simple schematic diagram of a photoluminescence experiment is shown in the following Figure 2.1.
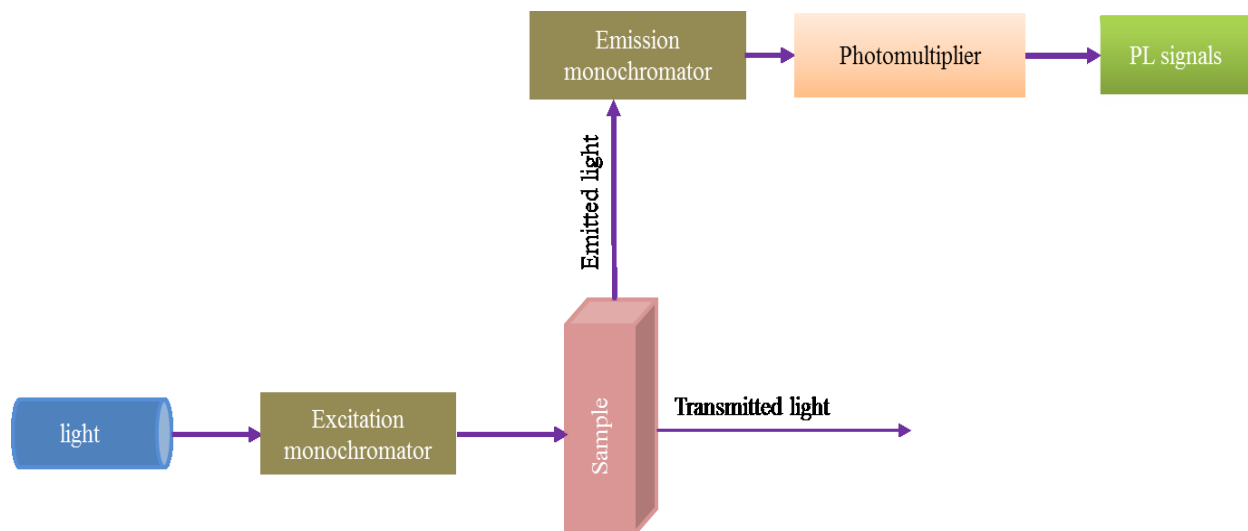
Figure 2.1 A schematic diagram of photoluminescence experiment.

Due to absorption of light, the valence electron(s) of a molecule in its ground state is forced to move to an excited state. The excited state of the molecule is metastable and can relax back to the ground state. During the relaxation process, the amount of energy absorbed from the excitation will be released in the form of photons and vibrational excitation (heat). Depending upon the nature of the excited state, photoluminescence is divided into two categories; fluorescence and phosphorescence. If the emission takes place from a singlet excited state to singlet ground state, the process is known as fluorescence. Fluorescence is a spin allowed process and takes place relatively fast. On the other hand, if the emission takes place from triplet excited state to singlet ground state, the process is known as phosphorescence. Phosphorescence is a spin forbidden process and it takes place comparatively slower than fluorescence. Beyond fluorescence and phosphorescence, there are several photo-physical processes that can deactivate the excited state molecules into the ground state. These processes are shown in a so-called Jablonski diagram in Figure 2.2.
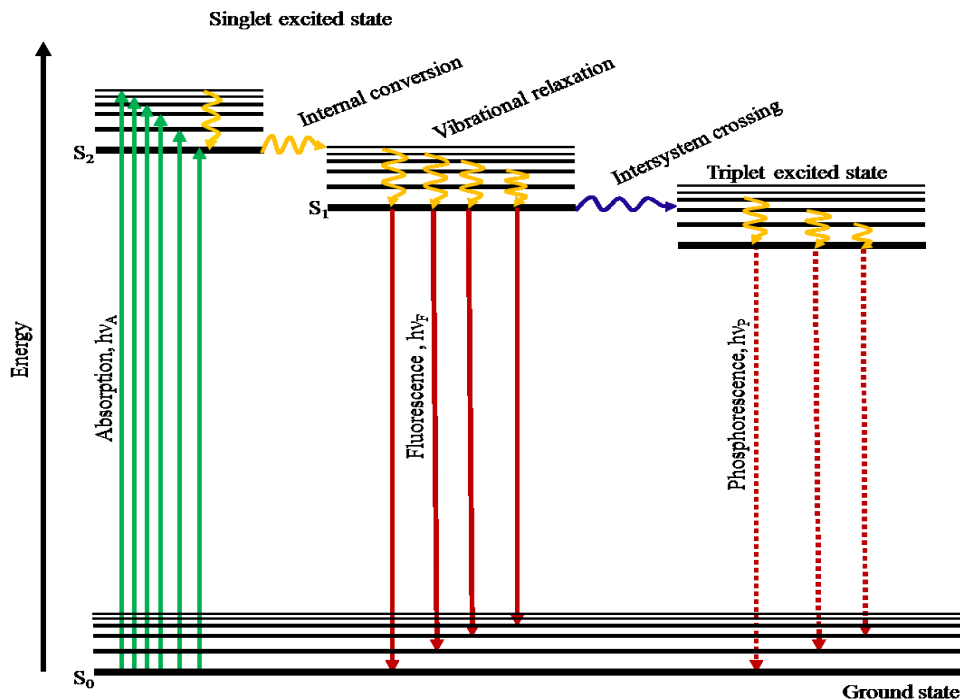
Figure 2.2 A simple Jablonski diagram showing singlet and triplet state with their vibrational energy levels.

When a photon is absorbed by a molecule, the molecule acquires the electronically excited state. The absorption of a photon takes place very fast (10^{-15} s). Next, relaxation of excited state to the ground state may involve radiative or non-radiative process. Fluorescence and phosphorescence are the radiative processes. Non-radiative processes contributing to the deactivation of excited state are internal conversion, vibrational relaxation, intersystem crossing, external conversion etc. In internal conversion, relaxation takes place from a ground vibrational energy level of an excited electronic state into a high vibrational energy level of a lower energy electronic state of the same spin. In vibrational relaxation, relaxation takes place form a higher excited vibrational level to the lower vibrational energy level of the same electronic state. On the other hand, in the inter system conversion, relaxation takes place from ground vibrational energy level of an excited electronic states into a high vibrational energy

level of a lower energy electronic state of a different spin. If the relaxation takes place by transferring the excess energy into the solvent or any other component present in the matrix is called external conversion. The external conversion is also known as collisional deactivation. All the deactivation processes are tabulated with their characteristic properties in the following table 2.1.

Transition type	Time scale second	Process
Absorption	10^{-15}	Radiative
Fluorescence	10^{-9}-10^{-7}	Radiative
Phosphorescence	10^{-4}-10^{-1}	Radiative
Internal conversion	10^{-14}-10^{-11}	Non-radiative
Vibrational relaxation	10^{-14}-10^{-11}	Non-radiative
Intersystem crossing	10^{-8}-10^{-3}	Non-radiative

Table 2.1 Excited state deactivation process with their characteristic properties.

There are some characteristics of fluorescence emission.

i.   Stokes shift: Emission during photoluminescence has less energy than that of absorption. Fluorescence usually occurs at lower energy or higher wavelength region which is known as Stokes shift. The Stokes shift is observed because some energy will be lost to the surrounding during vibrational relaxation, internal conversion, energy transfer, complex formation, excited state reaction, and solvent effects.

ii.   Kasha's rule: Fluorescence emission spectrum is typically independent of the wavelength of excitation radiation. When a molecule is excited to higher energy level, the excess energy is quickly dissipated and the molecule relaxes to the lowest

vibrational level of S_1 and usually emission occurs from the lowest vibrational level of S_1 and sometimes overlapping of nearby equal energy level may take place. The exception of this rule indicates a different geometric arrangement of nuclei between ground and excited state.

iii.   Mirror image rule: The emission is the mirror image of the $S_0 \rightarrow S_1$ absorption, not of the total absorption spectrum. Since the energy spacing between the vibrational levels in S_0 and S_1 is of the same size and the same transitions being involved in both absorption and emission.

Quantum yield and life time

To quantify the efficiency of fluorophore, terms quantum yield (Φ) and lifetime (τ) are used. Quantum yield is the ratio of number of emitted photons to the number of absorbed photons. Mathematically, it is given by[2]

$$\Phi = \frac{\Gamma}{\Gamma + k_{nr}}$$ 2.1

where Γ is the radiative decay rate and k_{nr} is the sum of non-radiative decay rates.

For the standard steady state spectrophotometer, quantum yield is usually determined by fluorescence intensity and spectra comparison with those of standard compounds of known fluorescence quantum yield. In most cases, the value of fluorescence quantum yield is less than unity because of the Stokes shift and other relaxation processes. However, sometime same number of photons emitted back, but those photons will be less energetic red photons. If non-radiative decay is very small compared to radiative decay, $k_{nr} \ll \Gamma$, the quantum yield is close to unity.

On the other hand, lifetime of fluorescence is the average time spends by a molecule at excited state before returning to ground state and is given by

$$\tau = \frac{1}{\Gamma + k_{nr}} \qquad\qquad 2.2$$

The fluorescence lifetime can be calculated directly from the decay curve of fluorescence intensity following a short excitation pulse or by detecting the emission response delay (phase shift) to the intensity modulated excitation light.[3] In absence of non-radiative decay, the lifetime of fluorescence is the reciprocal of the radiative decay rate and is called natural lifetime, denoted by τ_n.

$$\tau_n = \frac{1}{\Gamma} \qquad\qquad 2.3$$

Theoretically, the natural lifetime can be calculated from absorption spectra, extinction coefficient, and emission spectra of the fluorophore. Radiative decay rate can be calculated using following expression[2]

$$\Gamma \simeq 2.88 \times 10^9 n^2 \frac{\int F(\bar{v})d\bar{v}}{\int F(\bar{v})d\bar{v}/\bar{v}^3} \int \frac{\varepsilon(\bar{v})}{\bar{v}} d(\bar{v})$$

$$= 2.88 \times 10^9 \, n^2 < \bar{v}^{-3} >^{-1} \int \frac{\varepsilon(\bar{v})d\bar{v}}{\bar{v}} \qquad\qquad 2.4$$

where $F(\bar{v})$ is the emission spectrum plotted on the wavenumber scale, $\varepsilon(\bar{v})$ is the absorption spectrum and n is the refractive index of the medium. Fluorophores with high radiative rate have high quantum yields and short lifetime.

The radiative decay rate is determined by the oscillator strength (extinction coefficient) of the electronic transition[4] and the extinction coefficient of fluorophore is almost independent of its environment and hence there is no significant control over the radiative decay rate, Γ. Radiative decay rate for a given fluorophore is essentially constant. The change in lifetime and quantum yield of a fluorophore is due to the non-radiative decay rate, k_{nr}, if isolated fluorophore is considered.

Fluorescence quenching

Fluorescence quenching is the process that decreases the intensity of the fluorescence. Many energy transfer processes can result in quenching of the fluorescence. Collisional quenching and resonance energy transfer (Förster resonance energy transfer) are some examples. Collisional quenching occurs when the excited state fluorophore is deactivated after meeting with other molecules in solution. For collisional quenching, the decreased intensity is defined by the ratio of the intensity of fluorescence in absence of quencher and in presence of quencher and is given by Stern-Volmer equation:[5]

$$\frac{I_0}{I} = 1 + k_q \tau_0 [Q] = 1 + K_{SV}[Q] \qquad\qquad 2.5$$

where k_q is the bimolecular quenching constant, τ_0 is the unquenched lifetime, K_{SV} is the Stern-Volmer quenching constant, and $[Q]$ is the concentration of the quencher. The lifetime of the quenched fluorophore is decreased by the additional non-radiative process to the ground state.

Another important process of fluorescence quenching is resonance energy transfer (RET). Resonance energy transfer occurs when energy passes non-radiatively from one excited molecule to a second molecule. The first is called donor molecule and the later is called accepter molecule. RET occurs when the emission spectrum of the donor overlaps with the absorption spectrum of the acceptor.[6] However, the efficiency of RET is only significant when donor and acceptor are very close to each other (1-10 nm). Emission of light from excited state does not take place in RET and is not a result of the absorption of the light by acceptor molecule. The donor and acceptor are coupled by a dipole-dipole interaction. The extent of energy transfer is determined by the distance between the donor and the acceptor along with the extent of spectral overlap. If Förster distance, R_0, is the distance at which 50% of excitation energy of the donor is

transferred to the acceptor and the rest is dissipated by other process, is used to described the

spectral overlap, the rate of energy transfer is given by[2]

$$k_T(r) = \frac{1}{\tau_D}\left(\frac{R_0^6}{R_0^6 + r^6}\right)$$

2.6

where r is the distance between the donor and the acceptor, τ_D is the lifetime of the donor in the

absence of energy transfer. Then the energy transfer efficiency for a single donor-acceptor pair at

fixed distance is

$$E = \frac{R_0^6}{R_0^6 + r^6}$$

2.7

The Förster distance is given by[7]

$$R_0 = (JK^2 Q_D n^{-4})^{1/2} \times 9.7 \times 10^3 \text{Å}$$

2.8

where Q_D is the quantum yield of the donor, n is the refractive index of the medium between the

donor and the acceptor, K^2 is the orientation factor for dipole-dipole interaction, which depends

on the relative orientation of the donor emission transition moment and acceptor absorption

transition moment. The value of K^2 varies from 4 to 0 for parallel and perpendicular transition

moments and J is the spectral overlap between the donor and the acceptor and is given by

$$J = \frac{\int F(\lambda)\, \varepsilon(\lambda)\lambda^4 d\lambda}{\int F(\lambda) d\lambda}$$

2.9

where $F(\lambda)$ is the fluorescence intensity of the donor at the wavelength λ, and $\varepsilon(\lambda)$ is the

extinction coefficient of the acceptor. The medium between donor and acceptor has insignificant

effect (n^{-4}). The extent of transfer depends on distance r. The Förster distances are comparable

in size to biological macromolecules: 10 to 60 Å. For this reason energy transfer can be used to

measure the distance between sites on proteins.

Effect of metallic nanoparticle surfaces on fluorescence

Both quenching and energy transfer processes provide the non-radiative pathways to ground state. The rate of radiative decay is almost independent of quenching and the energy transfer process. The radiative rate of fluorophore in free space, a homogeneous and non-conducting medium, mostly depends on the excitation coefficient and the absorption spectrum of the fluorophore.[4] In any other medium, fluorescence lifetime of an excited state is not only the function of the fluorophore but also the function of the environment. Changing the environment around the fluorophore changes the radiative as well as non-radiative decay rate and the lifetime as well.[8] A metallic surface or a conducting medium can modify the radiative decay rate of the excited molecule. Some studies showed enhancement of fluorescence[9, 10] and some studies showed quenching of fluorescence.[11, 12] The interaction of a fluorophore with the metal surface can be assumed as the interaction of a fluorophore oscillating dipole with a conducting metal surface because the incident light induces electron oscillations in the fluorophore. The oscillations act as dipole that oscillates at high frequency and radiates short wavelengths. The nearby metal surfaces can respond to the oscillating dipoles and modify the rate of emission and the spatial distribution of the radiated energy. The electric field felt by a fluorophore depends on two types of interactions.[13] First is the interaction between incident light waves with the nearby metal surface and second is the interaction of the fluorophore oscillating dipole with the metal surface. The oscillating dipole of fluorophore can induce a field in the metal surface. All these interactions are responsible to increase or to decrease field incident on the fluorophore and consequently increase or decrease the radiative decay rate. In fact, the interaction is distance dependent.[14]

When a metal surface is near to the fluorophore, three dominant interactions between fluorophore and metals can take place. Fluorescence may be quenched at short distance from

metal (k_m), there can be an increase in rate of excitation (E_m), which is called the lightening-rod effect and there can be an increase in rate of radiative decay (Γ_m).[2] Jabloski diagram is helpful to demonstrate the effects of the metal surface which is shown in Figure 2.3.
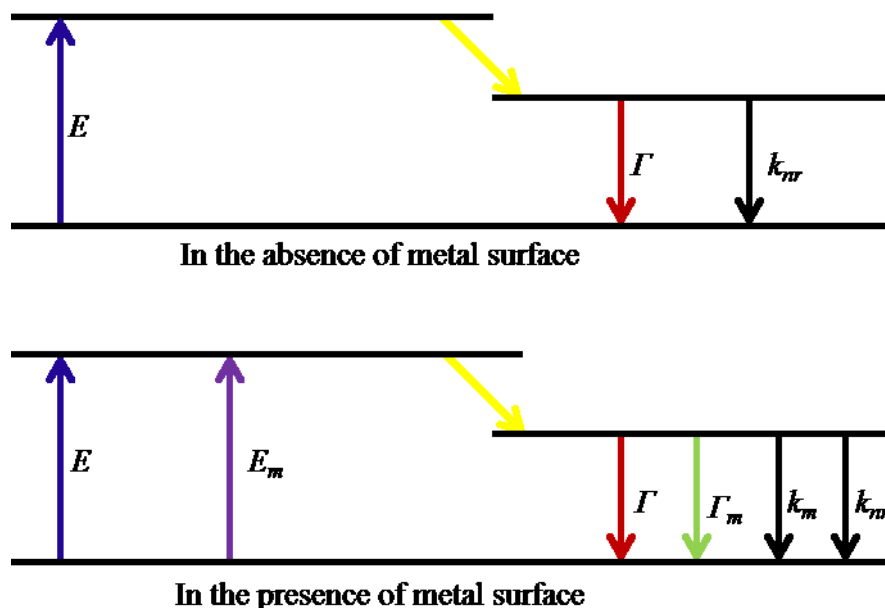
Figure 2.3 Jabloski diagram without and with the effect of near metal surface, E is the rate of excitation without metal and E_m is the additional excitation in presence of metal (reproduced from[2]).

In such case, the quantum yield and the lifetime of the fluorophore near to the metal surface is given by

$$Q_m = \frac{\Gamma + \Gamma_m}{\Gamma + \Gamma_m + k_{nr}}$$
2.10

$$\tau_m = \frac{1}{\Gamma + \Gamma_m + k_{nr}}$$
2.11

As Γ_m increases, the quantum yield increases and the lifetime decreases.

When the fluorophore and metal surface are very close to each other, less than 5 nm, non-radiative decay rate of fluorophore will be enhanced and consequently fluorescence intensity will be quenched. The quenching of intensity of fluorescence is due to the damping of dipole

39

oscillation of the fluorophore by the metal surface. At certain distance, the radiative decay rate over comes the non-radiative decay rate, leading to the enhancement of the fluorescence and reduced the emission lifetime. For the enhancement of the fluorescence, the following two factors are considered to be responsible:[15] first is the electromagnetic field enhanced near metallic surface due to the localized surface plasmon resonance (SLPR) which modifies the intensity of the electromagnetic field around the fluorophore and can lead to increase in the fluorescence intensity. Second is the coupling between the molecular dipole of fluorophore molecule and the surface plasmon field of the metal which leads to an increase of the radiative decay rate (stronger fluorescence emission), which is also known as radiative decay engineering (RED).[13] The effect of metallic particle on transitions of fluorophore is shown in Figure 2.4. Depending upon the distance between metallic NPs and fluorophore, nanoparticles can cause quenching (k_m), can concentrate the incident light field (E_m), and can increase the radiative decay rate (Γ_m).[16]
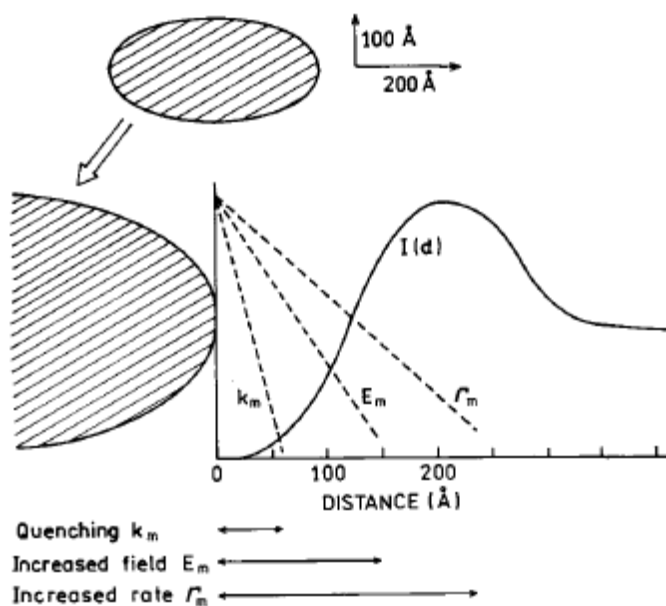
Figure 2.4 The effect of metallic particles on transitions of fluorophore.[16]

40

In our experiment, photoluminescence is used to observe the interactions between two different sizes (approx. 4 nm and 17 nm) of gold nanoparticles and Fe/Pt magnetic nanoparticle with octameric porin A from *Mycobacterium smegmatis* (MspA). MspA contains altogether 32 tryptophan molecules at different positions.[17] Tryptophan ($C_{11}H_{12}N_2O_2$) is an essential amino acid and an important biomolecule. Tryptophan level is abnormally high in people who are suffering from migraine headache and monitoring and controlling of tryptophan level may be helpful.[18] Most of the intrinsic fluorescence emission from a protein molecule is due to the excitation of tryptophan residues. Fluorescence emission spectra, quantum yields, and decay rates from the tryptophan has long been known to be highly sensitive to the polarity of its local environment and the presence of nearby quenchers.[19] Our expectation is the different interaction of small gold nanoparticles with MspA than that of large gold nanoparticles since small gold nanoparticles can go very close to the tryptophan molecule of MspA but large nanoparticles cannot. The different interaction should result different spectral features. This will be explained detail in chapter 5(A). On the other hand, Fe/Pt NPs should interact differently with MspA from gold NPs because magnetic property of Fe/Pt brings NPs closer to each other. The interaction of Fe/Pt with MspA will be discussed in chapter 5(B).

Faraday rotation (FR)

A chiral compound has a chiral center and its molecular mirror image is not superimposable on itself. Chiral compounds are optically active and they can rotate the plane of polarized light to a certain angle either in positive or in negative direction. Other compounds which do not have chiral center cannot rotate the plane of polarized light and are optically inactive. But in 1945, Michael Faraday discovered that when some optically inactive materials are exposed to a strong

magnetic field, they can also rotate the plane of polarized light.[20] The rotation of the polarization of light in a magnetic field can be observed either in reflection or in transmission. The rotation of polarization of reflected light is called Kerr rotation while the rotation of plane of polarization of transmitted light is called Faraday rotation to honor renowned scientists John Kerr and Michael Faraday, respectively. Both effects are collectively called as magneto-optical effect. Except Faraday and Kerr rotation, there is one more magneto-optical phenomenon which is called Cotton-Mouton effect. Cotton-Mouton effect involves the elliptization of plane of polarized light by a transverse magnetic field.[21] Kerr effect and Cotton-Mouton effects are beyond the scope of our research.

Magneto-optical effect provides physical information on electronic and spin structure of materials.[22] Faraday rotation can be seen in solids, liquids and gases.[23, 24] The direction of rotation depends on whether the impinging light is traveling parallel or antiparallel to the direction of the applied magnetic field. Faraday rotation effect can be found in wide use to measure the optical rotatory power, optical isolators,[25] optical switches, and for the remote sensing of magnetic field and electric current.[26] The measurement of Faraday rotation can also be used to infer the susceptibility of materials and to measure carrier densities in semiconductors if the carrier effective mass is known.[27]

Faraday rotation is the rotation of the plane of polarization of polarized light as it propagates through a dielectric medium in a magnetic field. The rotation is due to magnetic-field-induced circular birefringence in a material.[28] In a non-absorbing or weakly absorbing medium, a linearly polarized monochromatic light beam is passing through the material along the direction of the applied magnetic field experiences circular birefringence, which results in rotation of the plane of polarization of the incident light beam. The angle of rotation is

proportional to both applied magnetic field and optical path length. So, the angle of rotation (φ) can be expressed as

$$\varphi = vBL = \frac{\pi \Delta n L}{\lambda} \qquad\qquad 2.12$$

where Δn is the magnitude of the circular birefringence (a difference in refractive index of the left and the right circularly polarized light in the medium), L is the optical path length, λ is the wavelength of light, B is the applied magnetic field, and v is a constant and known as Verdet constant.

The rotation of the plane of polarization of a linearly polarized light can be measured by changing the amplitudes of two orthogonally linear polarized components.[29] The measurement of change in intensity of linearly polarized light by means of analyzer is the fundamental basis of the Faraday rotation measurement.

Experimental set up
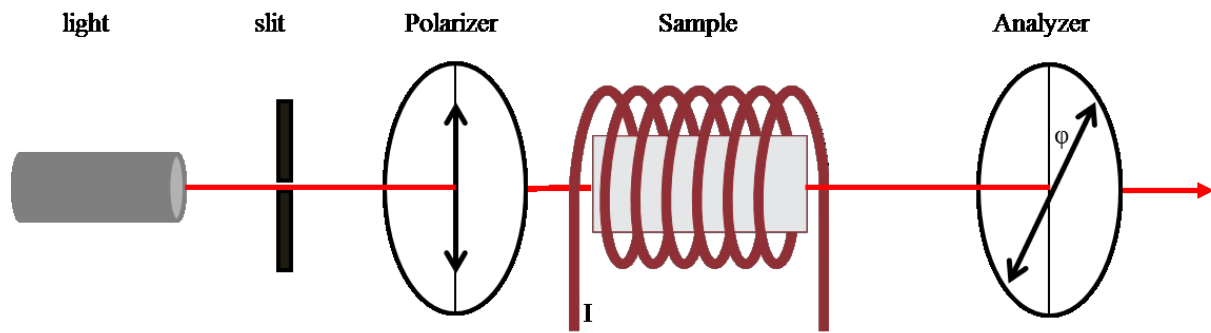
Figure 2.5 Schematic diagram of Faraday rotation measurement set up.

A simple Faraday rotation measurement set up is shown in Figure 2.5. It consists of a light source, a pair of polarizers (polarizer and analyzer), and a photodiode as a detector. The polarizer makes the light beam from the source polarized and that polarized light travels through the sample and reaches to the analyzer and then to the photodiode. If the sample is not

magnetized, the plane of polarization of the light beam is not affected and the amount of light energy that reaches to the photodiode depends on the angle between polarizer and analyzer.[30] When the sample is magnetized, the polarization of the transmitted light rotates slightly. The direction of rotation depends on the direction of magnetization. The effect of the magnetization variation is the same as the rotation of the analyzer and the current of the photodiodes have been changed accordingly. The magneto-optic effects are the difference rotation angle for two opposite magnetization directions and the rotation is calculated from the current or voltage of photodiode.

Theory of Faraday rotation

The electric field of a linearly polarized light beam propagating in the z direction and polarized along the x-axis can be expressed in Jones matrix as[28]

$$E_0 = \begin{pmatrix} 1 \\ 0 \end{pmatrix} A_0 exp(-i\omega t + ikz) \tag{2.13}$$

where A_0 is the amplitude of the electric field of incident light beam, k is the wave vector, ω is the angular frequency, and t is the time.

After passing through the sample, the polarization direction of the light is changed by an angle, φ, which is the Faraday rotation of the sample. Then the electric field of the transmitted light beam becomes

$$E = \begin{pmatrix} \cos\varphi \\ \sin\varphi \end{pmatrix} A_0 exp(-i\omega t + ikz) \tag{2.14}$$

Then the light traverses through an analyzer which is set at an angle, θ, with respect to the first polarizer. Then the electric field of the light beam after transmitting analyzer is

$$E = \begin{pmatrix} \cos(\theta - \varphi)\cos\theta \\ \cos(\theta - \varphi)\sin\varphi \end{pmatrix} A_0 exp(-i\omega t + ikz) \tag{2.15}$$

Then the light beam reaches to the detector, the intensity of light beam at the detector is

given by

$$I = cos^2(\theta - \varphi)A_0^2 \hspace{6cm} 2.16$$

The polarizer needs to be fixed in an optimal angle to get the maximum modulation of

light beam. By taking the first derivative of I with respect to angle, φ, the condition can be

obtained and is

$$\frac{\partial I}{\partial \varphi} = sin2(\theta - \varphi)A_0^2 \hspace{5.5cm} 2.17$$

Here, the angle of rotation, φ, is very small ($\ll 1º$), so when $\theta = 45º$, the maximum

modulation of light beam will be obtained. Thus when the analyzer is set at 45º, the intensity of

light beam that reaches to the detector photodiode is given by

$$I = \frac{1}{2}(1 + 2\varphi)A_0^2 \hspace{5.7cm} 2.18$$

This light beam intensity and the magnetic field are recorded in oscilloscope (LeCroy

WaveRunner 6050A) and the digitized data are transferred to a computer and analyzed. To

analyze the recorded data, Matlab programs are used. The codes that are used to analyze the data

are attached in appendix.

In order to generate the alternating magnetic field, an induction heater, manufactured by

Superior Induction Company, CA, is used. The heater contains a copper coil which has one inch

diameter with four turns and is continuously cooled with cold water. The heater operates with 5

kA/m field amplitude with 366 kHz frequency. For the pulsed magnetic field Faraday rotation

experiment, pulsed magnetic field (PMF) generator is established in our lab. The detail of the

setup of PMF is described in pulsed magnetic field Faraday rotation experiment chapter.

Verdet constant

Verdet constant is the characteristic rotation of a material per unit field per unit optical path length. Verdet constant is the material property and gives a quantitative measure of the Faraday rotation ability of the material. By convention, a positive Verdet constant corresponds to l-rotatory when the light propagates parallel to the applied magnetic field and d-rotatory when the light propagates antiparallel to the magnetic field.

Wavelength dependence

Villaverde et al;[31] measured the Verdet constant of different organic and inorganic liquids, in the spectral range from 347.2 nm to 694.3 nm, by measuring the magnetic field that requires to rotate the plane of polarization of the light beam by a preset angle. For diamagnetic materials, Verdet constant depends on both wavelength of the light and the change in index of refraction per change in wavelength (optical dispersion) in the medium and is given by Becquerel equation[32]

$$\nu = \frac{e}{2mc} \lambda \frac{dn}{d\lambda} \qquad\qquad 2.19$$

where λ is the wavelength of light, m is the mass of an electron, e is the charge in an electron, c is the velocity of light, n is the index of refraction of the medium and $\frac{dn}{d\lambda}$ is the optical dispersion.

The optical dispersion is theoretically related with electronic absorption spectrum through Wemple equation, which is based on the single electronic oscillator model in the region from UV to near-infrared as[33]

$$n^2 - 1 = \frac{E_d E_0}{E_0^2 - E^2} \qquad\qquad 2.20$$

where n is the refractive index, E is the energy of the photon, E_0 is the average electronic gap, and E_d is the electronic oscillator strength. Larger dispersion will be obtained when index of

refraction is large and is only true with smaller E_0 and/or large E_d. Wavelength dependence of the Verdet constant of some liquids is given in the following table 2.2.

Verdet Constant (min G^{-1} cm^{-1})					
Wavelength, nm	Methanol	Water	Toluene	Nitrobenzene	Ethanol
488.0	0.0143	0.0201	0.0421	0.0330	0.0170
501.7	0.0135	0.0191	0.0391	0.0306	0.0161
514.5	0.0127	0.0180	0.0367	0.0289	0.0153
580.0	0.0103	0.0141	0.0278	0.0229	0.0120
632.8	0.00824	0.0115	0.0227	0.0186	0.00997
694.3	0.00647	0.00913	0.0180	0.0149	0.00790

Table 2.2 Wavelength dependence Verdet constant of selected liquids.[31]

Temperature dependence

Barnes *et al.*[25] investigated the temperature dependence of Verdet constant and showed roughly *1/T* dependence. The differentiation of the rotation angle with respect to temperature gives the following equation

$$\frac{d\varphi}{dT} = \frac{\partial B}{\partial T} \nu L + \frac{\partial \nu}{\partial T} BL + \alpha \nu BL \qquad 2.21$$

Here, α is the coefficient of thermal expansion which value is very small and can be neglected the whole term. This equation, after dividing by $\varphi = \nu BL$, becomes

$$\frac{1}{\varphi}\frac{d\varphi}{dT} = \frac{1}{B}\frac{\partial B}{\partial T} + \frac{1}{\nu}\frac{\partial \nu}{\partial T} \qquad 2.22$$

φ and $\frac{d\varphi}{dT}$ both can be obtained from experiment, $\frac{\partial B}{\partial T}$ can be obtained from the manufacturer of the magnet and the remaining terms give the relationship between temperature with Verdet constant.

Figure 2.6 is showing the variation of angle of rotation of terbium gallium garnet with temperature at different wavelength in micrometer.
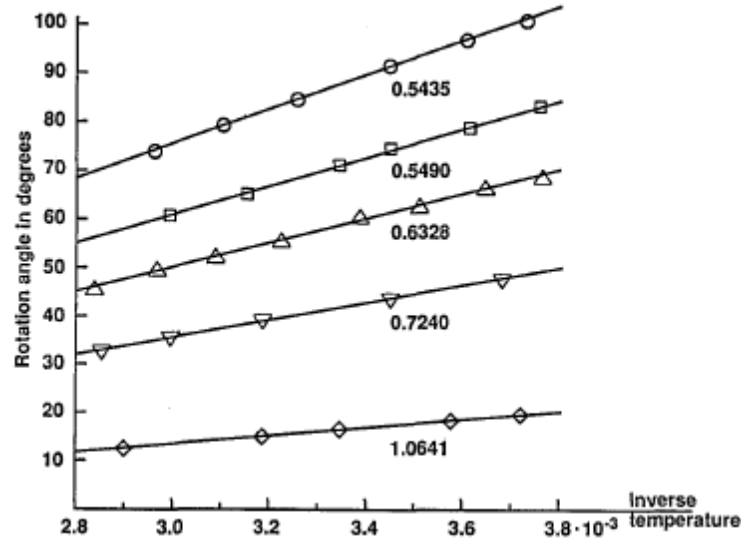
Figure 2.6 Variation of angle of rotation of terbium gallium garnet with inverse of temperature.[25]

Faraday rotation of nanoparticles

The noble metal NPs composites are interesting for their plasmonics. Plasmonics describe the propagation of optical signal due to the coupled localized surface plasmon resonances of nanometer scale metallic structures.[34] Potentially interesting effects arise when localized surface plasmon resonances from noble metal particles coupled with magnetic NPs. For example, magneto-optical properties of ferrite magnetic NPs have attracted a great attention due to their potential use in magneto-optical storage materials and high-frequency devices such as an isolator, and a circulator.[35] The practical uses sometime restricted due to the high Curie temperature of the materials because a high intensity of the laser pulse would require to heat a bit area of the recording media to overcome the Curie temperature in order for remagentization to occur during the writing process.[36] Superparamagnetic NPs could lower the temperature for the

48

reorientation of the magnetization vector. Besides this, nanometer size materials have shown promising enhanced optical rotation after coating magnetic NPs with plasmonic material.[37]

In our experiment, Fe_2O_3 NPs are used to investigate the Faraday rotation with successive coating of thin shell of gold around iron oxide NPs in alternating magnetic field. Enhancement of Faraday rotation is expected with the successive gold shell coating. Gold shell coating provides the coupling between the plasmon resonance of gold and magneto-optic electron transitions of magnetic nanoparticles. The drawback of magnetic materials is their high absorption losses[38] because of their large absorption coefficient. The large absorption coefficient causes the damping of plasmon resonance of the materials. Hence the localized surface plasmon of interface between magnetic material and dielectric medium is not well-defined because of strong damping$\left(\left|\frac{Re(\varepsilon_m)}{Im(\varepsilon_m)}\right| < 1\right)$. A feasible way to reduce the damping without losing magneto-optical activity is to combine noble material with the magnetic material. Since localized surface plasmon resonance of the noble metal is high$\left(\left|\frac{Re(\varepsilon_n)}{Im(\varepsilon_n)}\right| \gg 1\right)$. When there is good overlapping between plasmonic and magneto-optic resonance, a plasmon resonance can cause an enhancement in the magneto-optic resonance of the nearby nonplasmonic magnetic materials.[39] The detail will be discussed in chapter 3.

In chapter 4, Faraday rotation of gold and thin gold shell coated Fe_2O_3 NPs in pulsed magnetic field will be discussed. The resolution and sensitivity of measurements are limited by the maximum available magnetic field.[40] By using pulsed magnetic field, higher magnetic fields can be generated. If higher magnetic field is available, wider ranges of measurements can be achieved.

References

1.   Chen, Y.; Barkley, M. D., *Biochemistry* **1998,** *37* (28), 9976-9982.

2.   Lakowicz, J. R., *Principles of Fluorescence Spectroscopy*. Third ed.; Springer: 2006.

3.   Hof, M.; Fidler, V.; Hutterer, R., Basics of Fluorescence Spectroscopy in Biosciences. In *Fluorescence Spectroscopy in Biology*, Hof, M.; Hutterer, R.; Fidler, V., Eds. Springer: 2005.

4.   Strickler, S. J.; Berg, R. A., *The Journal of chemical physics* **1962,** *37* (4), 814-&.

5.   Geddes, C. D., *Meas. Sci. Technol.* **2001,** *12* (9), R53-R88.

6.   Cheng, P. C., The Contrast Formation in Optical Microscopy. In *Handbook of Biological Confocal Microscopy*, 3rd ed.; Pawley, J., Ed. Springer: New York, 2006.

7.   Stryer, L.; Stryer, *Annu. Rev. Biochem.* **1978,** *47* (1), 819-846.

8.   Anger, P.; Bharadwaj, P.; Novotny, L., *Phys. Rev. Lett.* **2006,** *96* (11).

9.   Shimizu, K. T.; Woo, W. K.; Fisher, B. R.; Eisler, H. J.; Bawendi, M. G., *Phys. Rev. Lett.* **2002,** *89* (11).

10.   Kramer, A.; Trabesinger, W.; Hecht, B.; Wild, U. P., *Appl. Phys. Lett.* **2002,** *80* (9), 1652-1654.

11.   Trabesinger, W.; Kramer, A.; Kreiter, M.; Hecht, B.; Wild, U. P., *Appl. Phys. Lett.* **2002,** *81* (11), 2118-2120.

12.   Dulkeith, E.; Ringler, M.; Klar, T. A.; Feldmann, J.; Javier, A. M., *Nano Lett.* **2005,** *5* (4), 585-589.

13.   Lakowicz, *Anal. Biochem.* **2001,** *298* (1), 1-24.

14.   Chen, H.; Ming, T.; Zhao, L.; Wang, F.; Sun, L.-D., *Nano Today* **2010,** *5* (5), 494-505.

15.   Iosin, M.; Baldeck, P.; Astilean, S., *Nuclear instruments & methods in physics research. Section B, Beam interactions with materials and atoms* **2009,** *267* (2), 403-405.

16.   Lakowicz, J. R., *Anal. Biochem.* **2001,** *298*, 1-24.

17.   Dani, R.; Kang, M.; Kalita, M.; Smith, P.; Bossmann, S.; Chikan, V., *Nano Lett.* **2008,** *8* (4), 1229-1236.

18.   Rativa, D.; Wachsmann Hogiu, S.; Farkas, D.; de Araujo, R., *J. Fluoresc.* **2008,** *18* (6), 1151-1155.

19.   Gryczynski; Malak, H.; Lakowicz, J. R., *Biospectroscopy* **1996,** *2* (1), 9-15.

20.   Hecht, E., *Optics*. Addison-Wesley: 2002.

21.   Walker, M. J.; Raymond, R. C., *Journal of the Optical Society of America* **1950,** *40* (11), 766-768.

22.   Kravets, V.; Lapchuk, A., *Appl. Opt.* **2010,** *49* (26), 5013-5019.

23.   Monk, G., *Light: Principles and Experiments*. Dover Publications, Inc., New York: 1963.

24.   Jenkins, F.; White, H., *Fundamentals of Optics*. McGraw-Hill, Inc., New York: 1976.

25.   Barnes, N. P.; Petway, L. B., *Journal of the Optical Society of America. B, Optical physics* **1992,** *9* (10), 1912-1915.

26.   Valev, V. K.; Wouters, J.; Verbiest, T., *European journal of physics* **2008,** *29* (5), 1099-1104.

27.   Alfano, R. R.; Baird, D. H., *J. Appl. Phys.* **1968,** *39* (6), 2931-2936.

28.   Jain, A.; Kumar, J.; Zhou, F. M.; Li, L.; Tripathy, S., *American journal of physics* **1999,** *67* (8), 714-717.

29.   Chang, C.-Y.; Wang, L.; Shy, J.-T.; Lin, C.-E.; Chou, C., *Rev. Sci. Instrum.* **2011,** *82* (6), 063112.

30.   Attaran-Kakhki, E., *Physica status solidi. C, Current topics in solid state physics* **2006,** *3* (9), 3257-3259.

31.   Villaverde, A. B.; Donatti, D. A., *The Journal of chemical physics* **1979,** *71* (10), 4021-4024.

32.   Pedrotti, F. L.; Bandettini, P., *American journal of physics* **1990,** *58* (6), 542-545.

33.   Yayama, H.; Fujino, S.; Morinaga, K.; Takebe, H.; Hewak, D. W., *J. Non-Cryst. Solids* **1998,** *239* (1-3), 187-191.

34.   Moolekamp, F.; Stokes, K., *IEEE Trans. Magn.* **2009,** *45* (10), 4888-4891.

35.   Uchida, H.; Masuda, Y.; Fujikawa, R.; Baryshev, A. V.; Inoue, M., *J. Magn. Magn. Mater.* **2009,** *321* (7), 843-845.

36.   Anderson, R. M.; Vestal, C. R.; Samia, A. C. S.; Zhang, Z. J., *Appl. Phys. Lett.* **2004,** *84* (16), 3115-3117.

37.   Wang, L.; Yang, K.; Clavero, C.; Nelson, A. J.; Carroll, K. J., *J. Appl. Phys.* **2010,** *107* (9), 09B303.

38.   Armelles, G.; González-Díaz, J. B.; Garcia Martin, A.; García-Martín, J. M.; Cebollada, A.; Gonzlez-Daz, J.; Garca-Martn, A.; Garca-Martn, J.; Uju-Gonzlez, M.; Acimovic, S.; Cesario, J.; Quidant, R.; Badenes, G., *Optics express* **2008,** *16* (20), 16104-16112.

39.   Jain, P.; Xiao, Y.; Walsworth, R.; Cohen, A., *Nano Lett.* **2009,** *9* (4), 1644-1650.

40.   Novickij, J., *Electronics and Electrical Engineering* **2007,** *78* (6), 29-34.

Chapter 3 - Enhanced Faraday rotation of gold coated Fe_2O_3 nanoparticles in alternating magnetic field

The magneto optical effect is the change of the propagation of electromagnetic waves when a quasi-static magnetic field is applied.[1] A typical example of that is Faraday rotation, when the phase velocity of the electromagnetic field is enhanced or decreased in a particular direction due to a slowly changing or static magnetic field.[2,3] Materials such as magnetic photonic crystals, which produce large Faraday response to small applied fields, are a desirable and active area of research.[4] Application of nanomaterials to produce Faraday response is advantageous because of the colloidal processing and the enhanced optical properties over the bulk material.[5] Particularly, nanomaterials that are sub 10 nm in size produce less scattering at visible and telecommunication wavelengths of light. The Faraday rotation of the materials, which is linearly proportional to the applied magnetic field and the thickness of the material,[6] is characterized by the Verdet constant expressed in units of radians per tesla per meter. While diamagnetic materials follow the linear response quite well over a large range of magnetic fields,[7] magnetic materials including magnetic nanomaterials tend to exhibit a saturation effect due to the saturation of magnetization of the materials.[8] This saturation effect mostly takes place at relatively high field strength. At lower field strength the linear response is still a good way to characterize the magneto optical response of the material.

In the past decade, several nanoparticles and their composites were explored to produce enhanced Faraday rotation in nanomaterials.[9-12] This enhancement in the Faraday rotation is allowed due to the complex composition of the material and the geometrical arrangement of the particles. E.g. Bamakov *et al*. found that the interparticle distance of Fe_3O_4 (magnetite)

nanoparticles strongly influences the Faraday rotation.[10] Their calculations based on the discrete-dipole approximation have shown qualitative agreement between their experimental findings and the theory, suggesting strong enhancement when the particles are spaced between 5-10 nm. Further increase of distance results in saturation of the Faraday rotation of the particles. Recently, calculations and experiments predict enhancement based on interaction of plasmonic and magnetic materials.[13-18] Smith *et al.* have carried out a calculation that shows this enhancement for composites such as silver-$CoFe_2O_4$.[15] Moolekamp *et al.* have created a colloidal gold and magnetite (Fe_3O_4) nanoparticles composite where the nanoparticles are chemically linked using a bifunctional organic ligand, creating clusters of the two nanoparticle components.[13] The addition of gold nanoparticles results in a change in the sign of the Faraday rotation as well as an enhancement of the ellipticity by about a factor of two at the wavelengths corresponding to the surface plasmon absorption peak of the gold nanoparticles. Similar plasmonic enhancements were found by Uchida *et al.* with localized surface plasmon resonance, which is obtained in a sample with Au nanoparticles embedded in a Bi-substituted yttrium iron garnet film.[14] Recently, enhanced optical Faraday rotation in gold-coated maghemite was reported by Jain *et al.*, which they call the surface plasmon resonance-enhanced magneto-optics or SuPREMO.[18] The experimental results clearly show that the magnetic enhancement of the Faraday rotation agrees well with the surface plasmon resonance of the gold coated Fe_2O_3 nanoparticles.

In this study, the SuPREMO effect is further investigated to observe the functional dependence of the Faraday rotation enhancement of the Fe_2O_3 nanoparticles on the thickness of their gold overcoat. The experiments are carried out at fixed wavelength (632 nm) with subsequent growth of gold shell on the Fe_2O_3 nanoparticles. The results show that the Faraday

enhancement changes sign when the gold coating is applied, in agreement with the previous results. In addition to the magnitude of the Faraday signal, the Faraday phase of the AC measurement strongly depends on the clustering of the particles, which undergoes changes when the gold coating is applied.

Experiment

Experimental setup

The schematic diagram of the Faraday rotation experimental setup is shown Figure 3.1. It consists of a laser source (He-Ne, 632 nm, 5 mW power), a sheet polarizer (to control the laser power), a second polarizer, an iris, a water cooled copper induction coil (4 turns, 1" diameter to generate the alternating magnetic fields) connected with AC source, a cell (as a sample holder, 39 mm long, contains sample solution), a pickup coil (37 mm ID, to detect the signals of the alternating magnetic field), a Wollaston prism (to split the transmitted beam into two polarized light to the balanced photodiode to mirrors), a balanced photodiode (to collect the signals), an amplifier (to amplify the signals) and a computer (to record the signals). The polarizer allows controlling the laser power, which is fixed at 130 μW for all measurements. The laser beam becomes linearly polarized after passing through second polarizer. Then the light is passed through the sample solution, which is under the influence of the alternating magnetic field. This magnetic field induced birefringence results in a rotation of the polarization of the incident linearly polarized light. The amount of rotation, φ, is proportional to the magnitude of the magnetic field, B, and to the length of the sample, L,

$$\varphi = vBL = \frac{\pi \Delta n L}{\lambda} \hspace{5cm} 3.1$$

where v is the constant of proportionality known as the Verdet constant, Δn is the magnitude of circular birefringence (the difference in refractive index of left and right circularly polarized light

55

in the medium), λ is the wavelength of the light. The transmitted light beam is split into two perpendicular polarizations by a Wollaston prism. The light beams are focused on a balanced photodiode. The signal from the balanced photodiode is then amplified and recorded in a computer. The pickup coil collects the signals from the alternating magnetic field and is recorded along with the Faraday signal. The distance of the pickup coil is fixed in such a way that the distance between the pickup coil and the coil that produces the alternating magnetic field is always the same for all measurements.
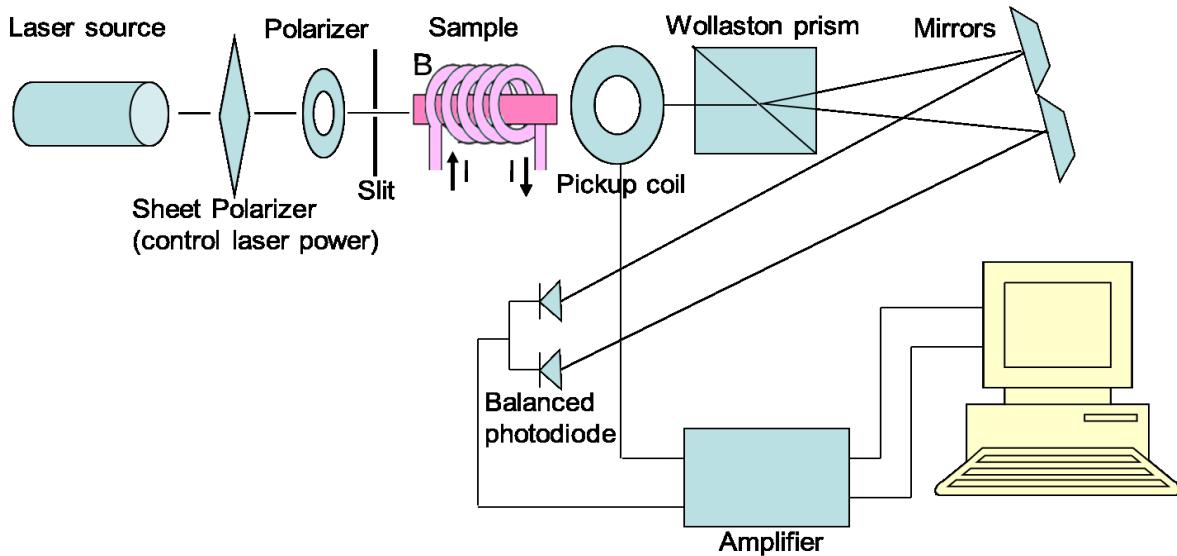
Figure 3.1 Experimental setup of Faraday rotation apparatus.

The Faraday setup is tested by using commercially available Fe_3O_4 nanoparticles. Figure 3.2 shows the signal obtained by the experimental setup for a commercially available colloidal solution of iron oxide nanoparticles. The upper figure shows the sinusoidal wave of the pickup coil signal and the Faraday signal generated by the nanoparticle solution as a function of time

and the lower figure shows the fitting data of these two signals. The fitting and analysis of the sinusoidal curves are done by using the equation a×sin(b×time + c) + d, where two important parameters 'a' and 'c' are the amplitude and phase of the signals, respectively. 'b' corresponds to the angular frequency of the alternating magnetic field and 'd' is an offset parameter to account for the baseline of the signals.
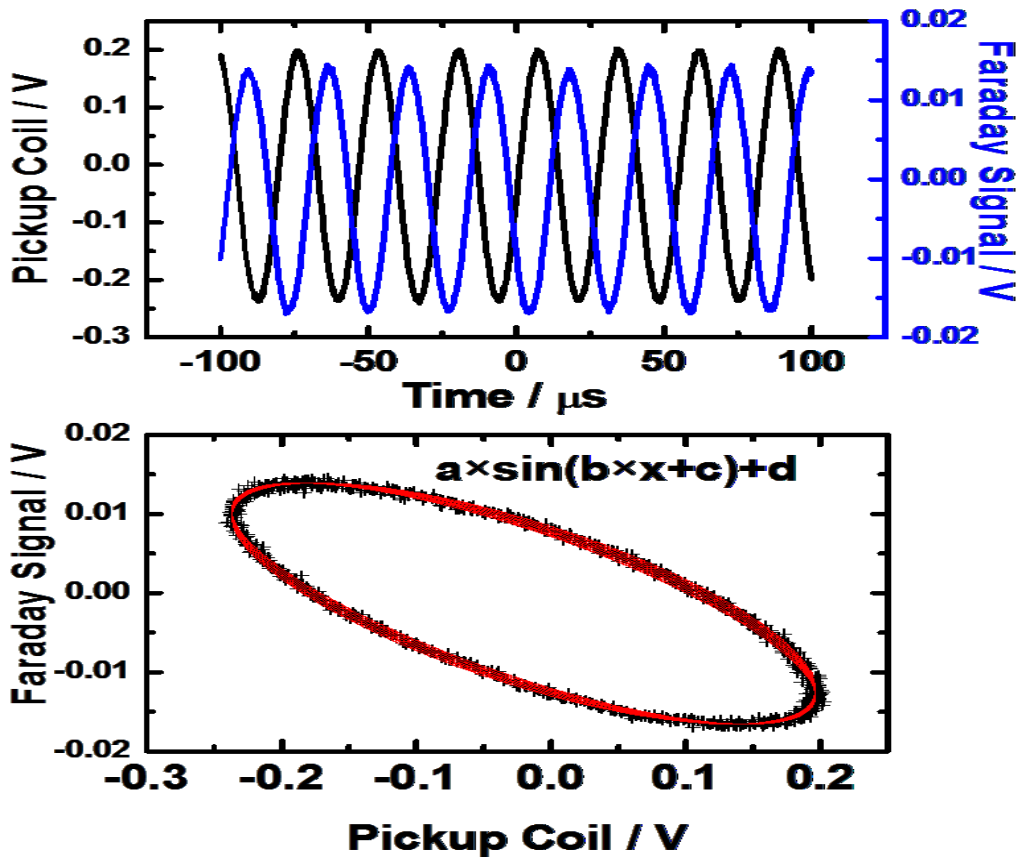
Figure 3.2 (UPPER) The time dependent magnetic field signal from the pickup coil (black) and Faraday signal (blue) of commercial iron oxide solution. (LOWER) The graph of the Faraday signal against the magnetic field signal. Both sets of data are fitted with sine function indicated by the solid line (see text).

	a	b	c	d
Magnetic field	1.0034 ±0.0025	2.250× 10^6±633	1.9944±0.0024	-0.0022±0.0017
Faraday signal	0.9972±0.0025	2.250× 10^6±684	-0.0040±0.0026	-0.0002±0.0018

Table 3.1 Fitting parameters used in Figure 3.2.

Chemicals

Hexahydrate ferric chloride ($FeCl_3.6H_2O$), tetrahydrate ferrous chloride ($FeCl_2.4H_2O$), sodium hydroxide (NaOH) is purchased from Acros Organics. Hydrochloric acid (HCl), nitric acid (HNO_3), tetraammonium hydroxide (TMAOH), hydroxylamine hydrochloride ($NH_2OH.HCl$), chloroauric acid trihydrate ($HAuCl_4.3H_2O$) are purchased from Sigma-Aldrich.

NPs synthesis and gold coating

Iron oxide nanoparticles are synthesized and coated with gold shell as described by Lyon *et al.*[19] Briefly, 20 mmol of $FeCl_3.6H_2O$ and 10 mmol of $FeCl_2.4H_2O$ are dissolved in 25 mL of distilled water containing 0.315 mL of HCl (density 1.19 g /ml). The solution is added drop wise to 250 mL of 1.5 M NaOH solution with vigorous stirring. The solution immediately produces black precipitate of Fe_3O_4. The precipitate is washed with water several times. Following this, the precipitate is dissolved in 250 mL of 0.1 M HNO_3 and centrifuged at 6000 rpm for 30 minutes. The precipitate is separated and dissolved in 250 mL of 0.01 M HNO_3 solution. The solution is heated to 90–100 °C for 30 minutes to oxidize the Fe_3O_4 nanoparticles into Fe_2O_3 nanoparticles. The color of the solution changes from black to brown red. The solution is cooled down to room temperature. The dark precipitate is separated again and washed with distilled water twice and with 100 mL of 0.1M tetramethylammonium hydroxide (TMAOH) once. Then the remaining precipitate is dissolved in 250 mL of 0.1 M TMAOH solution. The concentration of the

nanoparticles is found to be 1.12 g/L. Average particle size of thus prepared nanoparticles is 9.7 ± 2 nm. The TEM image and the size distribution are shown in Figure 3.3(a) and 3.3(b) respectively.
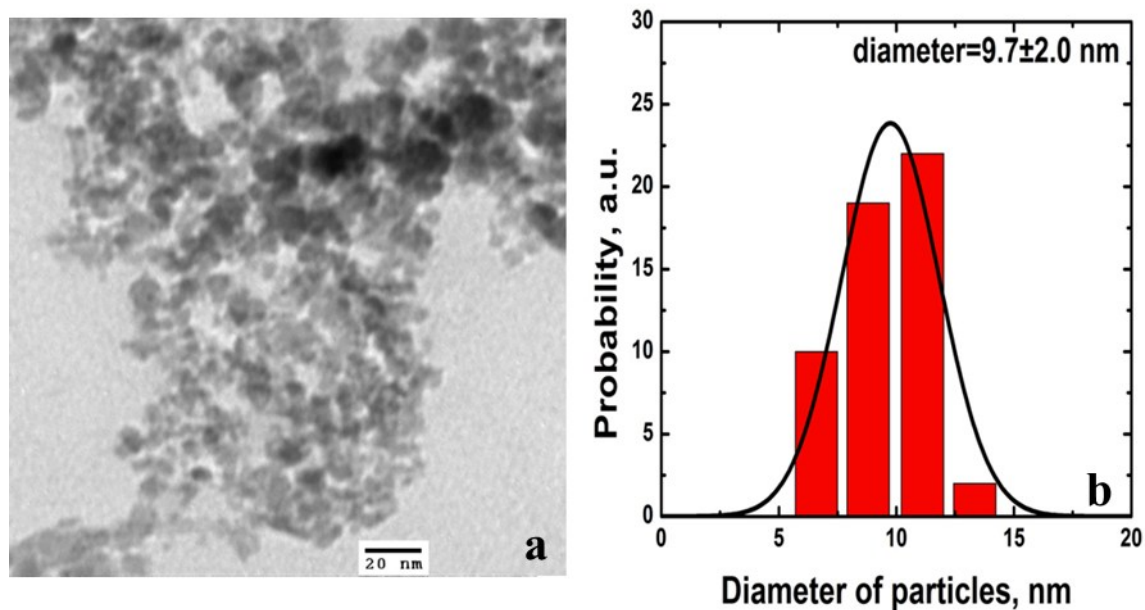
Figure 3.3 (a) TEM image of Fe$_2$O$_3$ nanoparticles used in the experiment and (b) Size distribution of the nanoparticles, average diameter is found to be 9.7 ± 2 nm.

Gold shell is coated on the surface of the nanoparticles by reducing Au^{3+} ions onto the surface of the Fe$_2$O$_3$ nanoparticles. For this purpose, 5.35 mL of nanoparticle solution is mixed with the same volume of 0.1 M sodium citrate solution. The solution is diluted by adding 100 mL of water and stirred for 15 minutes. The 535 μL of 0.2 M NH$_2$OH.HCl and 445 μL of 0.254 M HAuCl$_4$.3H$_2$O are mixed. After 15 minutes, 200 μL of NH$_2$OH.HCl and 360 μL of 0.254 M HAuCl$_4$.3H$_2$O are added to the solution for further shell coating. The same procedure is repeated with same amount of reagents for 8 times for the 1st batch. For the 2nd and 3rd batches, different volume of the NH$_2$OH.HCl and HAuCl$_4$.3H$_2$O are used. For the 2nd batch, in the 1st step 180 μL

of $NH_2OH.HCl$ and 445 µL $HAuCl_4.3H_2O$ is added. After this 66µL and 119µL of $NH_2OH.HCl$ and $HAuCl_4.3H_2O$ solutions respectively, are added in each step repeated up to 15 steps. In the 3rd batch, 270 µL and then 100 µL of $NH_2OH.HCl$ and 225 µL and then 178 µL of $HAuCl_4.3H_2O$ are added in the 1st step and repeated up to 20th steps. After every addition of $NH_2OH.HCl$ and $HAuCl_4.3H_2O$ solutions, 1 mL of the solution is taken to record the UV-visible absorption of the samples.

As the thickness of the gold shell increases with the addition of gold solution, the plasmon peaks shift to the shorter wavelength region as shown in Figure 3.4(a) for one of the batches. Figure 3.4(b) shows the color variation of the solutions after shell coating with gold. Color is changed from greenish brown to dark pink. The experimental relationship between the plasmon peak and amount of the gold is plotted in Figure 3.4(c). As the thickness increases the peak maximum shifts to the lower wavelength region showing similar behavior like pure gold nanoparticles.[19-21] A similar trend is obtained for calculation using Mie scattering theory, which is shown in the dotted black line.[22,23] The cluster size of the nanoparticles is measured by dynamic light scattering in every step after the addition of $NH_2OH.HCl$ and $HAuCl_4.3H_2O$. It has been found that the cluster size of Fe_2O_3 nanoparticles is around 160 nm before mixing with any reagent. Interestingly, with the addition of $NH_2OH.HCl$ and $HAuCl_4.3H_2O$, the cluster size decreases to 98 nm (1st step), then 90 nm (2nd step), then 87 nm (3rd step), and then the cluster size stabilizes at around 80 nm with ± 5 nm error for the other steps.
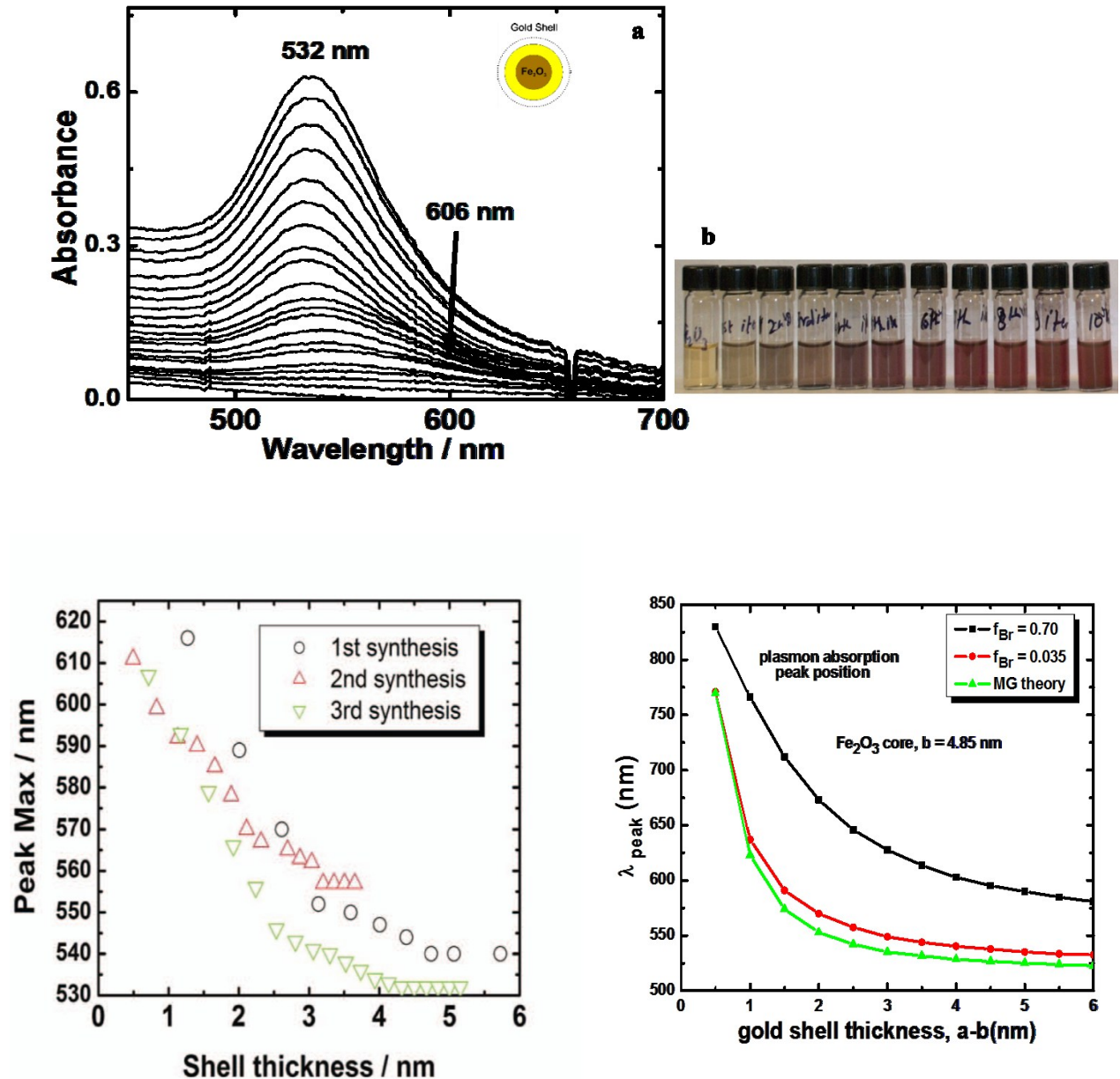
Figure 3.4 (a) UV-visible absorption spectrum of 3rd batch synthesis of gold coated Fe_2O_3 nanoparticles. The initial peak position is indicated by an arrow at 606 nm and shifts to 532 nm with increasing thickness of gold shell. **(b)** Variation of color change when the thickness of gold onto the surface of the nanoparticles is increased. **(c)** The relationship between the peak maximum and shell thickness of all three batches of the of the gold coated Fe_2O_3 nanoparticles. **(d)** The graph represents the theoretical shell thickness variation calculating using Mie scattering theory (see appendix[25] section for details).

Faraday rotation measurement and discussion

For the Faraday rotation measurements, 1 mL of solution is taken out after every addition of $NH_2OH.HCl$ and $HAuCl_4.3H_2O$ and is diluted with 5 mL of distilled water, to make the solution light penetrable. The relationship between Faraday rotation of the gold coated Fe_2O_3 nanoparticles with concentration of gold solution added is shown in Figure 3.5. In Figure 3.5(a), the Verdet constant of the composite solution at a particle concentration of $3.60 \times 10^{18}/m^3$ (water signal is subtracted) indicates continuous rise. The Verdet constant of a dilute NP solution is proportional to the volume fraction of NPs. When the Verdet constant is normalized by the nanoparticle volume fraction, the shape of this curve changes (Figure 3.5(b)).
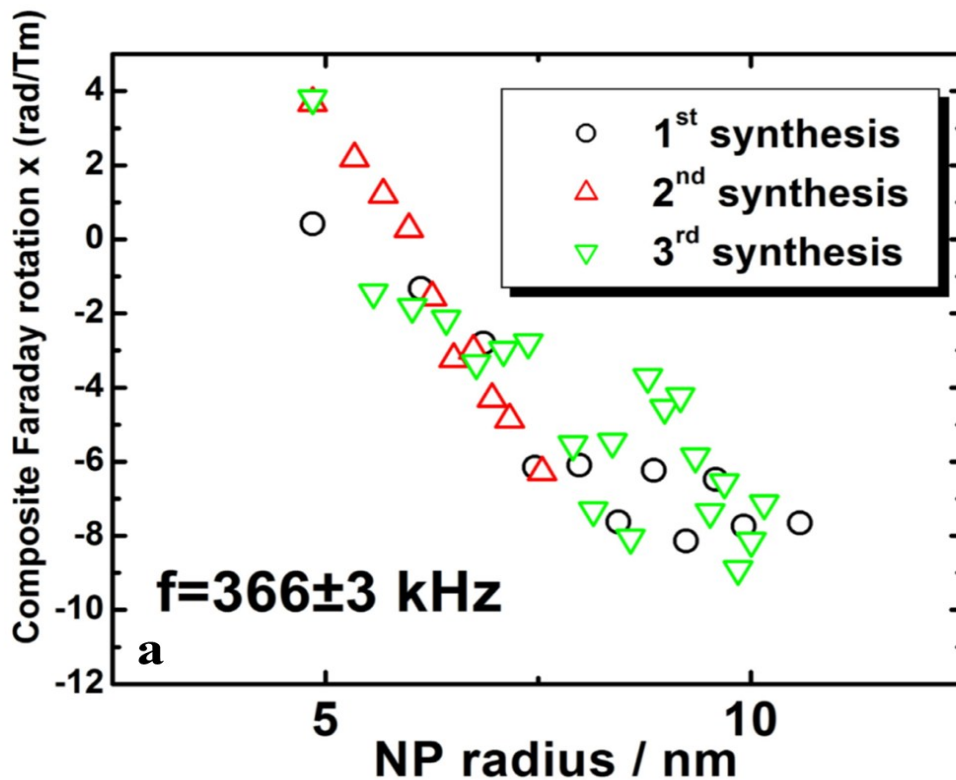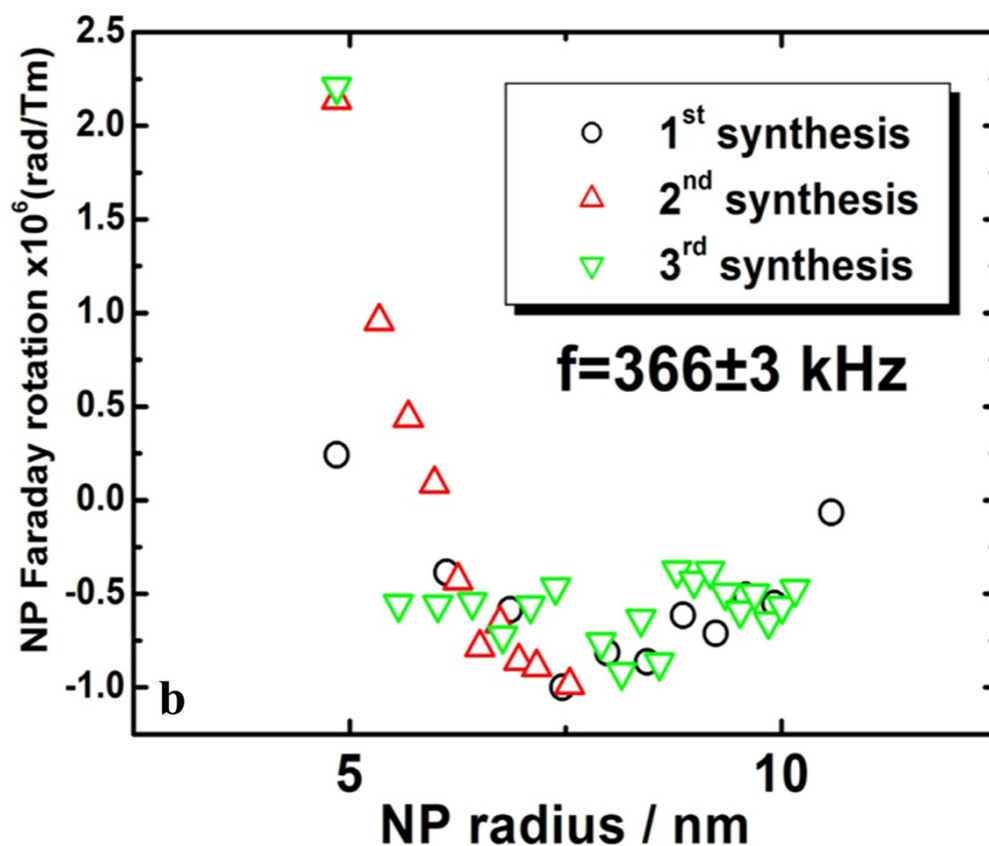
Figure 3.5 (a) Experimental Verdet constant of gold coated Fe₂O₃ nanoparticle solution as a function of gold shell thickness (b) Experimental Verdet constant of gold coated Fe₂O₃ nanoparticles only (normalized by the volume fraction of the particles) as a function of gold shell thickness.

The effective Verdet signal exhibits a saturation effect and turns around at a NP radius of 7 nm. The magnitude of the Verdet constant is in reasonable agreement with the Verdet constant of other magnetic nanoparticle solutions[24] and shows significant enhancement compared to traditional Faraday materials at 632 nm (e.g. terbium gallium garnet: 134 Rad/Tm at 632 nm.) While magnetic saturation effects could be important, at this field strength (0.00628 T) the nonlinearity of the Faraday signal can be ignored.

Figure 3.6 shows the relationship between phase lag of the Faraday signal relative to the magnetic field. Phase lag with Fe_2O_3 is relatively high and after addition of gold solution it decreases and is almost constant for other additions of the gold solution. The cluster size of the nanoparticles from dynamic light scattering experiments with the gold concentration is also shown in Figure 3.6. Similarly, the cluster size decreases with the addition of the gold solution for first three additions and remains almost constant for other additions. Clearly, this effect seems to show that on the time scale of the experiment, the nanoparticles show a dynamic alignment effect as a result of the rearrangement of the magnetic spins in a cluster consisting of many magnetic NPs. Based on the frequency used for the alternating magnetic field (366 ± 3 kHz), the estimated times of the full alignment of the magnetic spins are 0.65 and 0.17 μs for the bare vs. coated NPs, respectively. These data show that increasing cluster size results in slower relaxation in a cluster consisting of small magnetic nanoparticles.
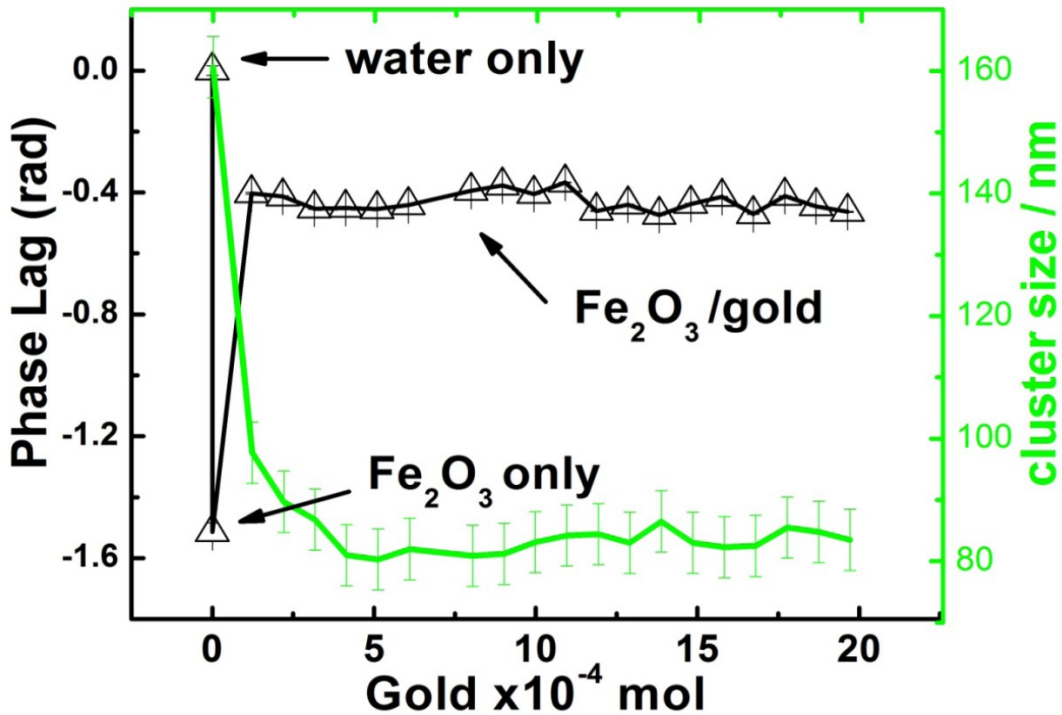
Figure 3.6 Phase lag between the signal of Faraday rotation and the magnetic field of gold coated Fe$_2$O$_3$ nanoparticles as a function of gold concentration. The cluster size of nanoparticles from dynamic light scattering is also shown in the figure.

In order to better understand the origin of the enhancement of the Faraday rotation of the gold coated iron oxide NPs, we made calculations based on classical electrodynamics in the Rayleigh limit.[26] We have included a Drude response due to free electrons, and importantly, another resonance that corresponds to bound electrons undergoing inter-band transitions in the gold. With only a Drude term as in Ref. 29, the plasmon resonance wavelength is predicted incorrectly to be near only 300 nm. Accounting for the bound electron response is essential; we made an approximation to the more correct treatment given by Inouye *et al.*[26] and applied more recently by Scaffardi and Tocho for gold NPs.[27]

The Faraday rotation of the particles is related to the difference in wave vector of left and right polarized light when the magnetic field is applied:

$$\varphi = \frac{1}{2} Re\{k_R - k_L\}z = \frac{\omega}{2c} \, Re \left\{-i \frac{\varepsilon_{xy}}{\sqrt{\varepsilon_{xx}}}\right\} \qquad\qquad 3.1$$

Here, k_R and k_L are the wavevector of the left and right polarized light, z is the path length, ω is the angular frequency of the light, c is the speed of light and ε_{xx} and ε_{xy} are diagonal and off diagonal elements of the dielectric tensor. The calculated Verdet constant of Fe$_2$O$_3$ NPs is a strong function of wavelength as shown in Figure 3.7 for 4.85 nm Fe$_2$O$_3$ core radius using the Maxwell Garnet (MG) theory. The Faraday rotation spectrum somewhat mirrors the optical absorption of the nanoparticles. According to the calculation, near the plasmon resonance the Faraday rotation exhibits both left and right rotation. In these experiments, the Faraday rotation spectrum is probed at fixed wavelength, therefore the calculated Faraday rotation of the gold coated particles at 633 nm is shown in figure 3.7(b) and 3.7(c). The two graphs show the Verdet

constant of the composite medium as well as the Verdet constant of the nanoparticles only (Verdet constant normalized to the volume fraction of the particles).
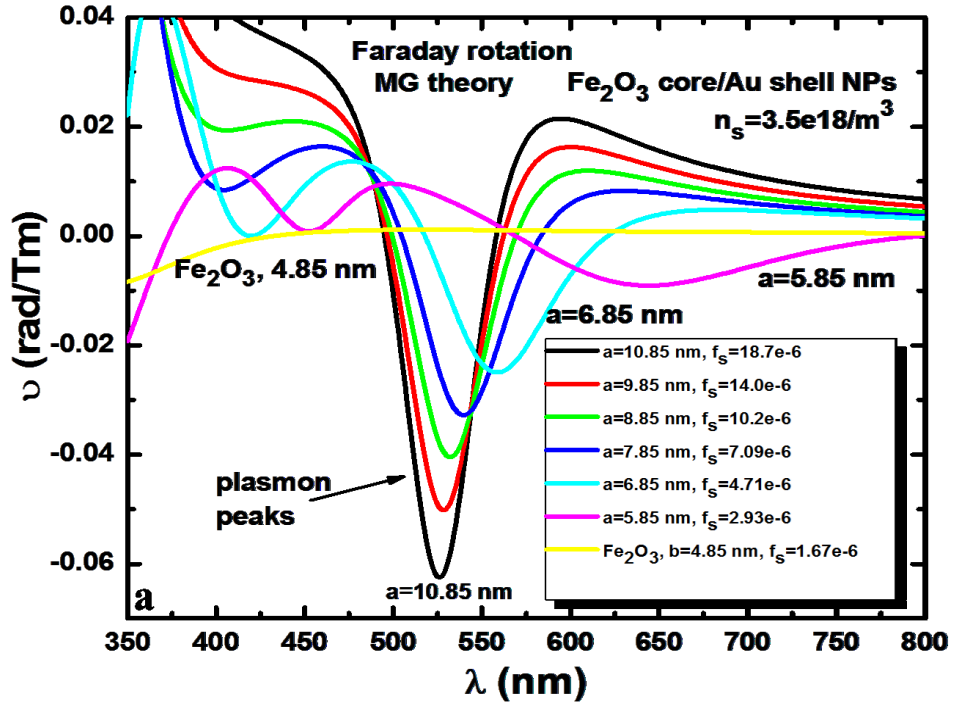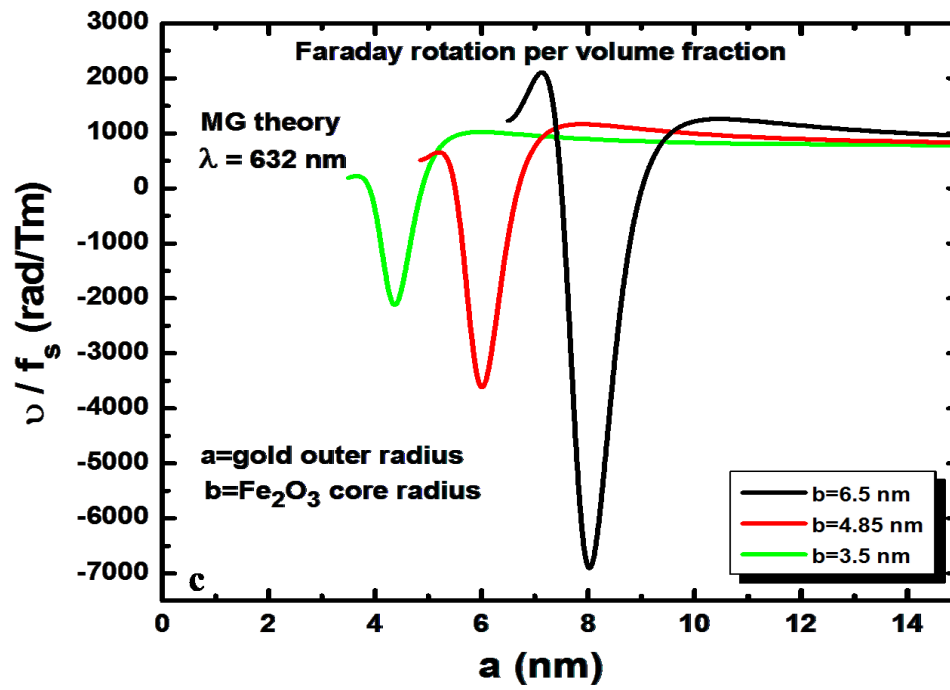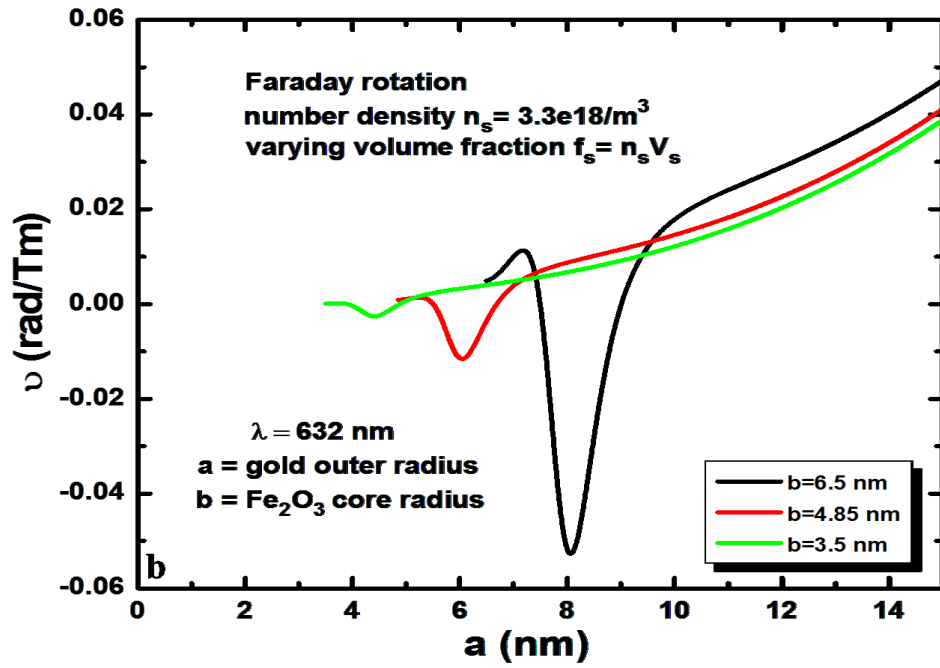
Figure 3.7 (a) Calculated wavelength dependent Faraday rotation (MG Theory) of core/shell nanoparticles in water, showing the variations with increasing gold shell thickness corresponding to the experiment. (b) Same as (a) at 632 nm. (c) Same as (b), but normalized by the NP volume fraction.

Interestingly, the Verdet constant at 633 nm is very sensitive to the core diameter variation, which is not expected to be observed in our experiments, because of the relatively large size distribution of the particles. The calculation indicates that as gold shell is coated on the Fe_2O_3 NPs, the Faraday rotation at 632 nm will change sign in agreement with the experimental observation. Furthermore, the Faraday signal is enhanced significantly when thicker gold shell is coated on the surface of Fe_2O_3 core. As the surface plasmon resonance of the NPs shifts from red to blue, the Faraday signal will reach a maximum and turns back. This is partly due to the actual shift in the plasmon peak position due the gold shell thickness. Since the experiments are done at fixed frequency the shell thickness increase continuously detunes from the plasmon resonance of the particles. This shift also originates from the increased scattering length of electrons due to thicker gold shell thickness. The increased scattering length is also accounted for in the calculations. Interestingly, we do not see the actual turn back feature in the experiment. There are multiple possible reasons why the turn back is not observed experimentally. First, in the experiment we could not go to any thicker shell material without sacrificing the solubility of the particles. Second, the calculation does not account for the size distribution of the particles, which in turn could result in the observed feature present in the experiment. From the experiments, the magnitude of the expected Faraday rotation appears to be larger than what is expected based on the calculations. This discrepancy could be the result of the overlap of the molecular transition and the plasmon shell of the Fe_2O_3 NP. This effect has been suggested by Jain *et al.* in the

68

original SuPREMO paper. Also, as we will show below, the clustering could have a major impact on the observed optical properties of the material.

Effective medium theories allow making a connection between the optical properties of the components and the average response of the composite optical medium. Since the dynamic light scattering data and the Faraday phase measurements indicate clustering, the Faraday signal is also calculated using a modification of the Maxwell Garnett theory to account for this observation. A simple way to account for clustering is using Bruggemann theory,[28] which is applied to systems where the particles are electrically connected and the volume fraction is relatively high. The results from this simulation are presented in Figure 3.8.

Bruggeman theory
$f_{Br}=0.70$

Fe_2O_3 core/Au shell NPs
$n_s=3.5e18/m^3$

υ (rad/Tm)

artifacts of model

plasmon peaks

a=10.85 nm

a=6.85 nm

a=7.85 nm

b

—	10.85 nm
—	9.85 nm
—	8.85 nm
—	7.85 nm
—	6.85 nm
—	5.85 nm
—	Fe2O3, b=4.85 nm

λ (nm)

Fe_2O_3 core radius, b = 4.85 nm
a = gold outer radius
number of density n_s = 3.5e18/m^3
varying volume fraction f_s = $n_s V_s$
Bruggeman cluster theory
λ = 632 nm

υ (rad/Tm)

c

—	f_{Br} = 0.70
—	f_{Br} = 0.035
—	f_{Br} = 1.0 (MG)

a (nm)

70
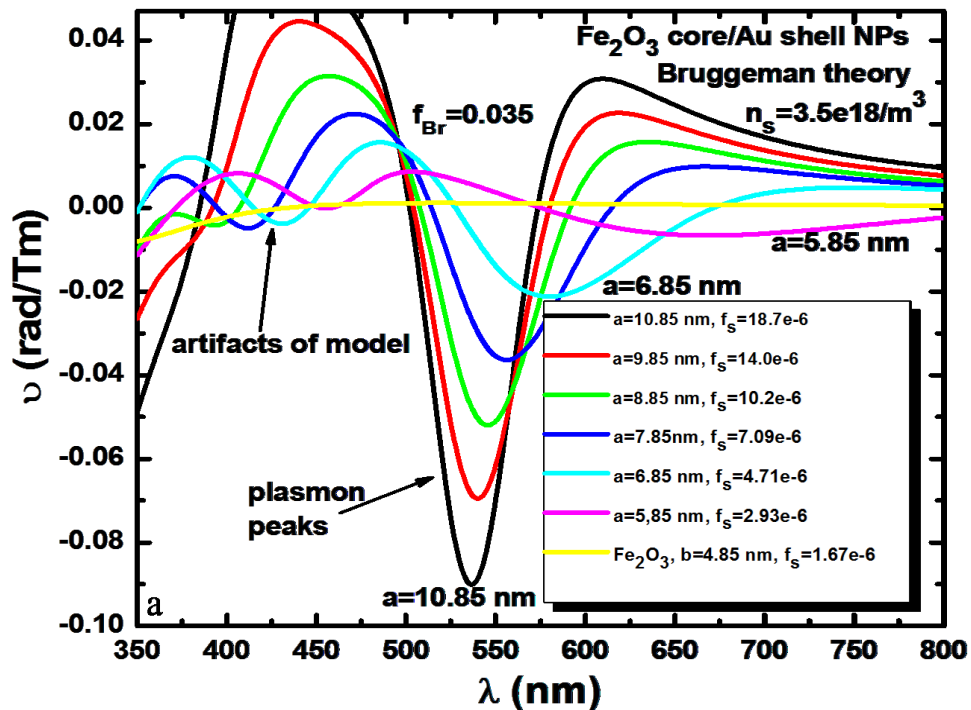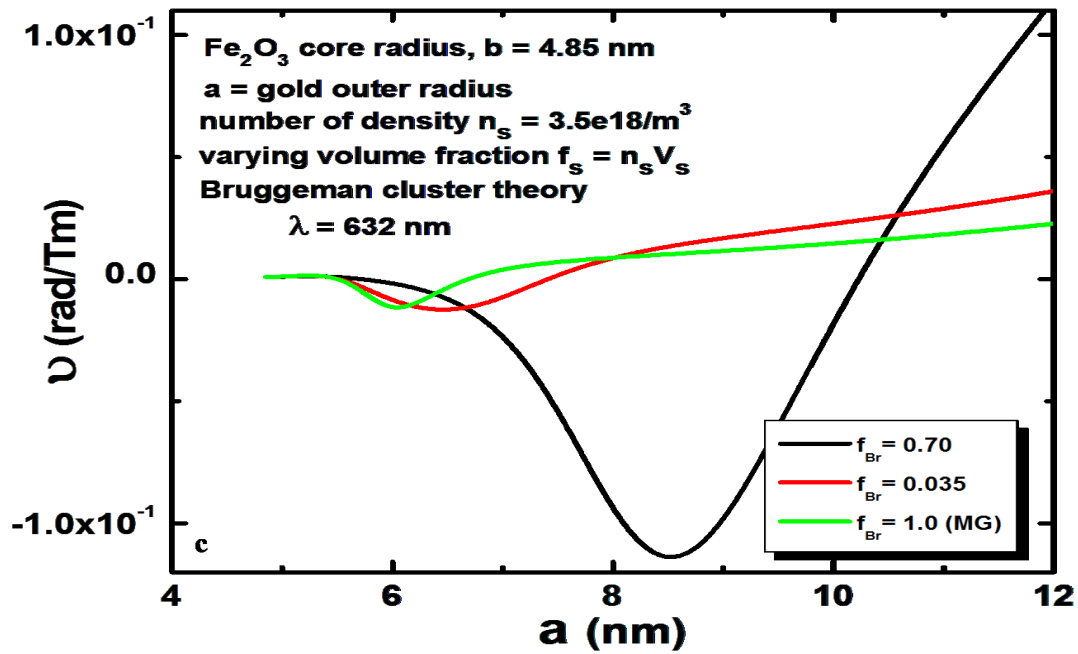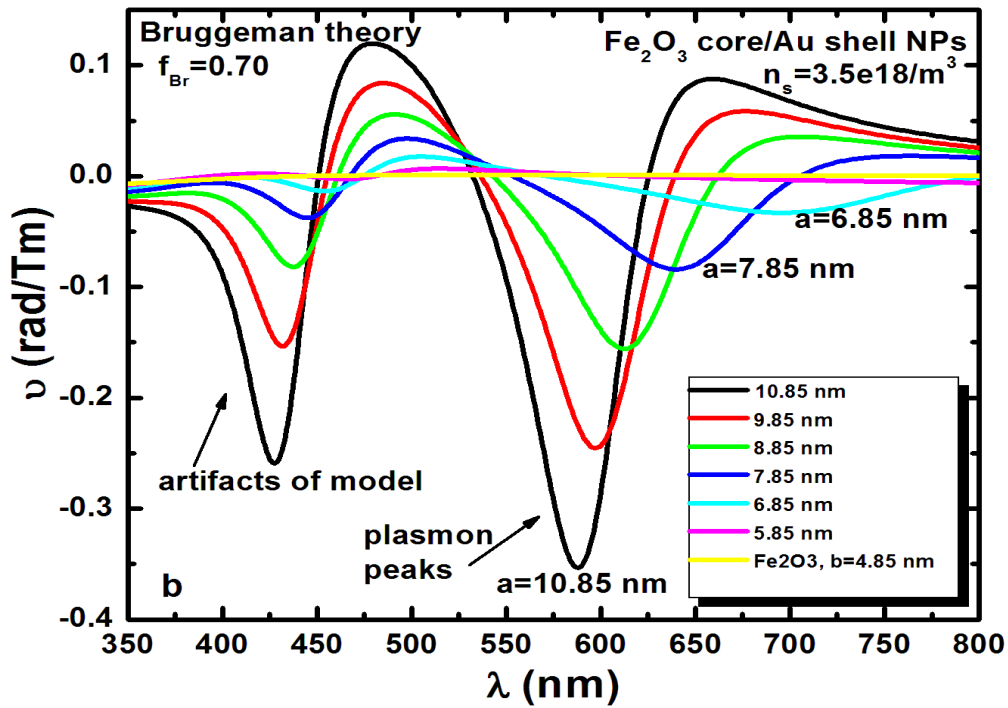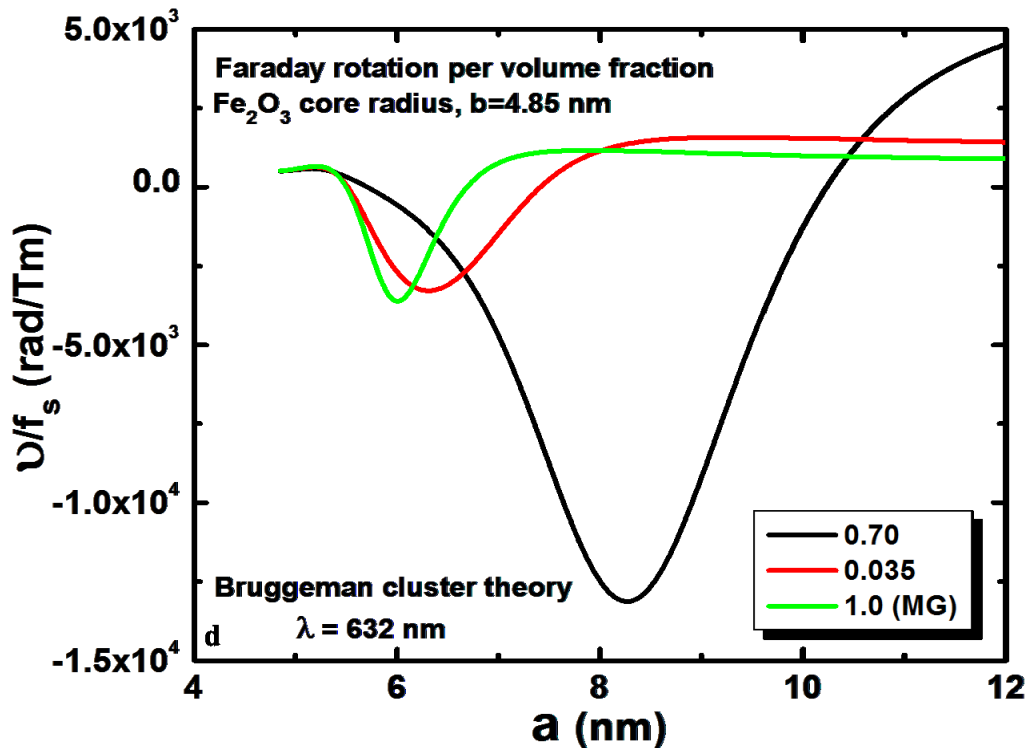
Figure 3.8 Calculated wavelength dependent Faraday rotation for core/shell particle solutions in water, including strong clustering effects via the Bruggeman theory (a) for 0.035 volume fraction and (b) 0.7 volume fraction. The peaks below 450 nm are artifacts due to the single resonance assumed for bound gold electrons. The plasmon peak does is slightly higher than that found without clustering effects. (c) Same as (a) at 632 nm (d) Same as (c), but normalized by the NP volume fraction.

Qualitatively, the Bruggeman theory shows that the spectral features present in the Faraday rotation spectrum become broader and red shifted relative to the MG theory. As a result of the spectral changes, the Verdet constant at 632 nm does not show a maximum, but a continuous increase of the Verdet constant with increasing gold shell thickness. By comparing experiment and theory, the experimentally measured Faraday rotation seems to be more

consistent with the clustering model at a fairly large packing fraction like 70%. Our conclusion from the calculation and from the Faraday phase shift is that clustering is important in solution in determining the average optical response (Faraday rotation) of the composite material consisting of magnetic nanoparticles and water. However, probably a more complete description of nanoparticle interactions is needed to consistently describe both the absorption and Faraday rotation spectra of these nanoparticle solutions simultaneously.

While the primary goal of this work was to investigate the relationship of the Faraday rotation and shell thickness of gold, it is interesting to compare the results in terms of the plasmon resonance wavelength of the particles. This comparison eliminates the need of calculating the shell thickness from experiment. The experiment show (Figure 3.9(a)) that the composite Faraday rotation signal crosses zero at long wavelengths (thin shell), the signal bottoms out at around 550 nm (~4 nm shell thickness or ~8nm particle radius). The calculations (Figure 3.9(b)-(d)) based on MG and Bruggeman theory exhibit the general features of zero crossing at long wavelengths and a minimum between 550-650 nm wavelengths. Interestingly this wavelength does not correspond to the measurement wavelength of the FR signal. The theory predicts that the minimum shifts to thicker shell if there is more clustering.
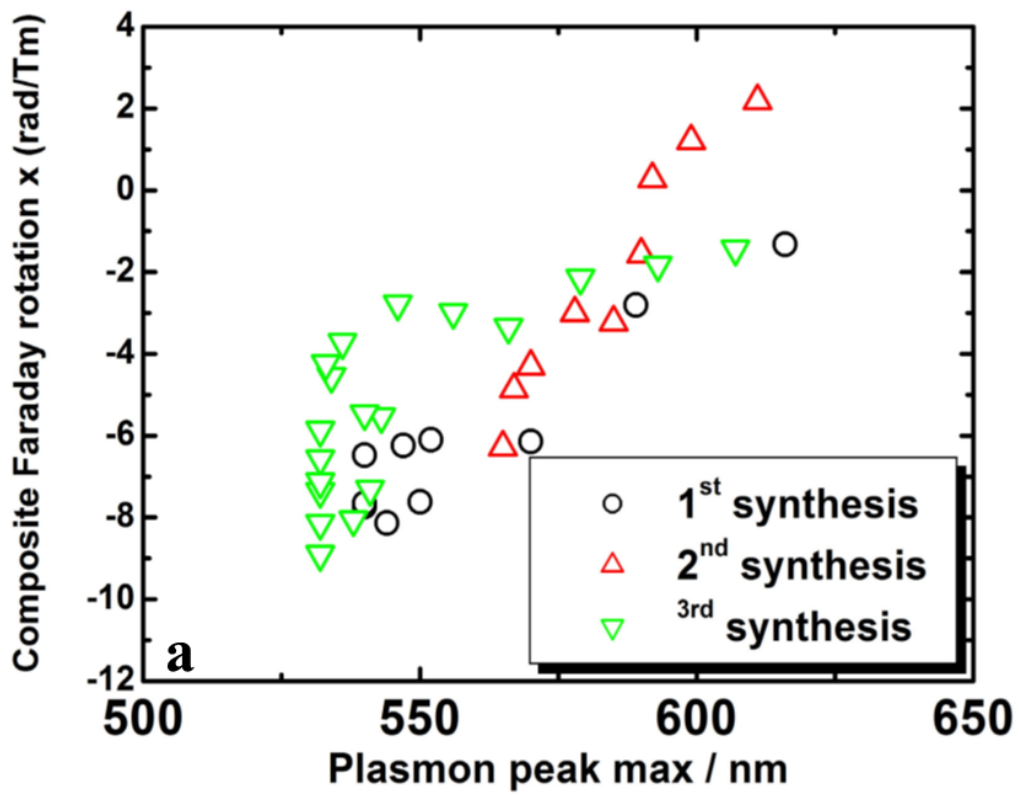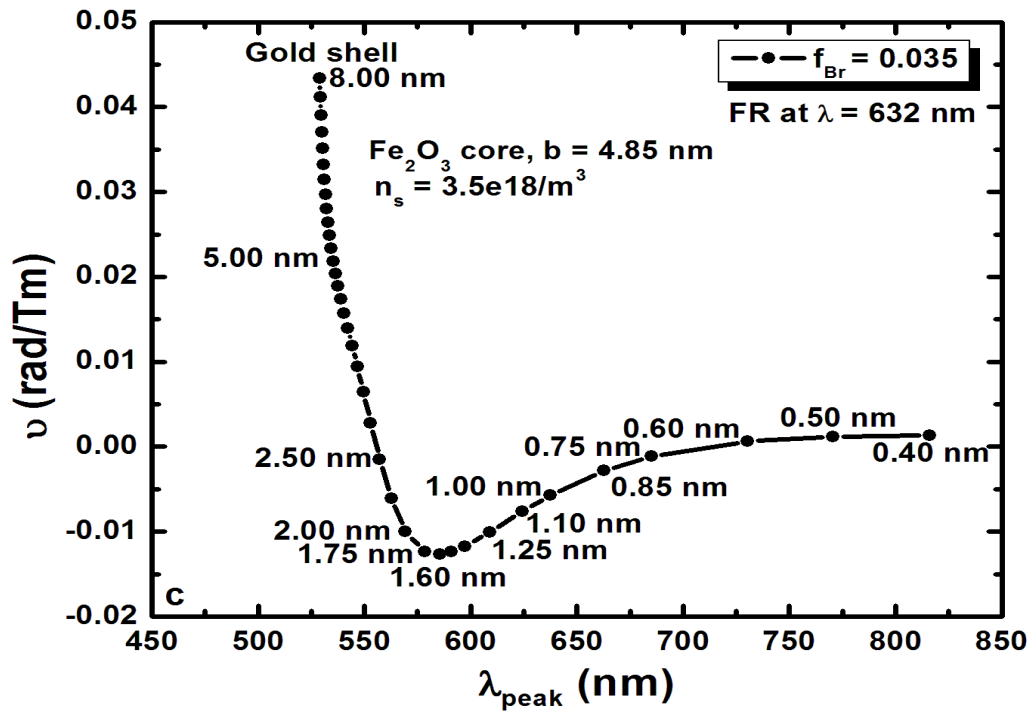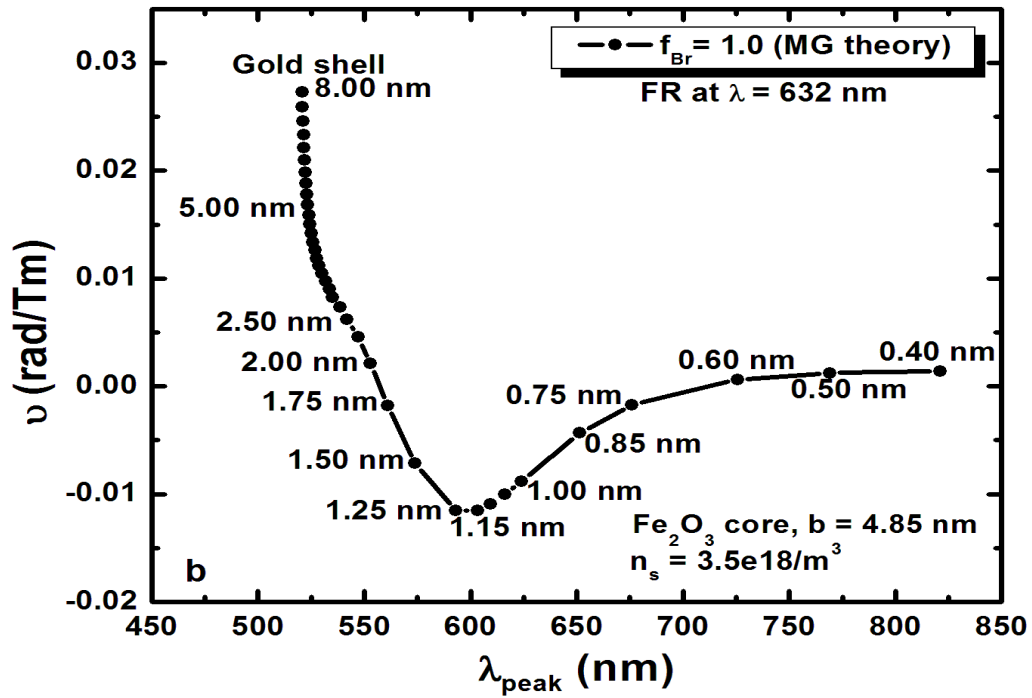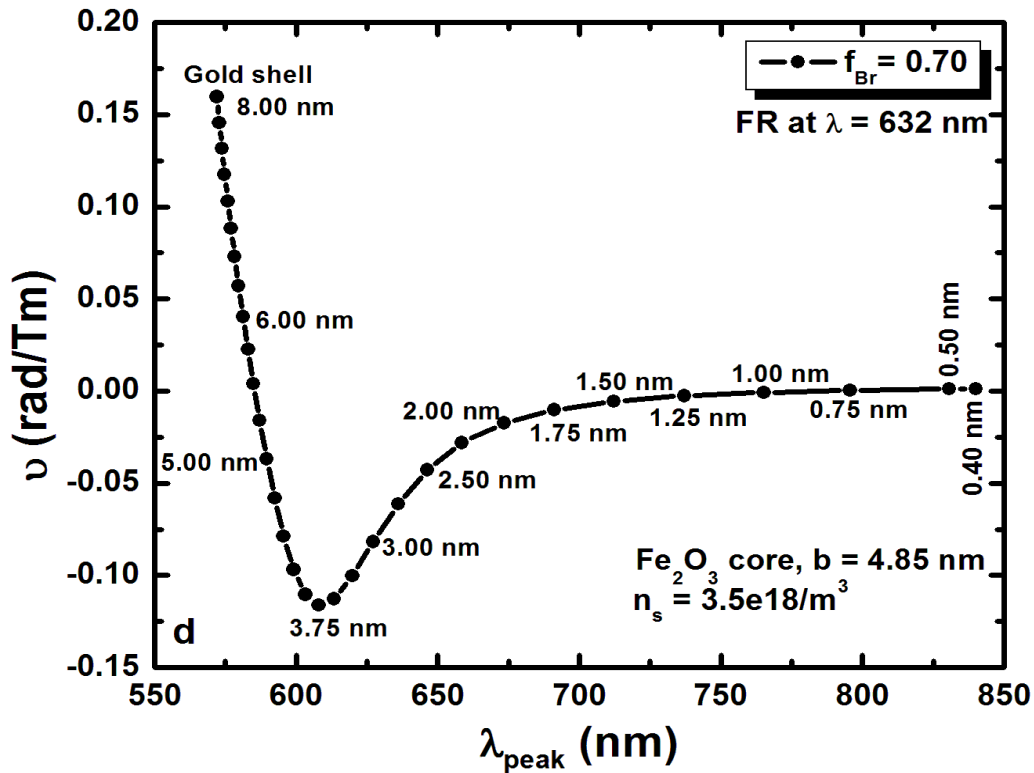
Figure 3.9 (a) Experimental Verdet constant of gold coated Fe$_2$O$_3$ nanoparticle solution as a function of surface plasmon resonance peak measured at 632 nm. (b)-(d) Calculated Verdet constant of gold coated Fe$_2$O$_3$ nanoparticle solution as a function of surface plasmon resonance peak measured at 632 nm.

Overall the results suggest that clustering is important of the interpretation of FR signal of magnetic NP in solution. Clustering could account in some extent for the enhanced FR signal as well as the deviation of the wavelength dependence of the FR signal from the FR signal of isolated particles. The simple Maxwell-Garnett theory assumes non interacting particles, which is not sufficient to describe the observed effects. Bruggeman theory takes into account of the near field interactions of the particles in an average fashion. Prior to this work, Moolekamp and

Stokes[13] already successfully used Bruggeman theory to improve the agreement of the magneto-optical response of chemically linked magnetite and gold nanoparticles. Although the Bruggeman theory produced better agreement with experiment, we think that future experiment and theory should focus on obtaining quantitative agreement.

Conclusions

In summary, the Faraday rotation of gold coated Fe_2O_3 NPs are measured at 632 nm as a function of gold shell thickness. Theory and experiments show qualitative agreement in describing the Faraday effect of the gold-coated NPs. The Faraday rotation reverses its sign when the gold shell is applied. The experimental Faraday signal exhibits saturation with gold shell thickness at 632 nm, but theory suggests that the Faraday rotation will eventually diminish and reverse sign again with increasing shell thickness. The theory shows that the variation in Faraday rotation with increased gold shell thickness is directly linked to the blue shift of the gold plasmon mode with increasing shell thickness. This interpretation is novel compared to previous observations of this effect. The distribution of NP sizes and shell thicknesses will spread out the variation in Faraday rotation beyond that indicated in the theory. The results also show that clustering of the magnetic NPs in solution may induce significant effects on the optical properties of these materials. In future experiments, it will desirable to control the aggregation (shape and size of aggregates) that can help develop better description for the aggregation in replacement of the Bruggeman theory used in this work. Using the NPs as isolators could be a significant improvement over commercial materials if this clustering can be minimized or maximized via manipulating the interparticle interactions, as well as improving the size distribution of the particles and the gold shell.

76

All the data presented in this chapter have been already published in J. Chem. Phys. 135, 224502, **2011**.

References

1.   R.D. Medford, A.L.T. Powell, W.H. Fletcher, J.D. Herbert, Nature, 192 (**1961**) 622-&.

2.   C.R. Pidgeon, R.N. Brown, Phys. Rev., 146 (**1966**) 575-&.

3.   W.A. Crossley, R.W. Cooper, J.L. Page, Vanstape.Rp, Phys. Rev., 181 (**1969**) 896-&.

4.   I.L. Lyubchanskii, N.N. Dadoenkova, M.I. Lyubchanskii, E.A. Shapovalov, T.H. Rasing, J. Phys. D-Appl. Phys., 36 (**2003**) R277-R287.

5.   R.B. Thompson, V.V. Ginzburg, M.W. Matsen, A.C. Balazs, Science, 292 (**2001**) 2469-2472.

6.   Buckingh.Ad, P.J. Stephens, Annu. Rev. Phys. Chem., 17 (**1966**) 399-&.

7.   P.A. Williams, A.H. Rose, G.W. Day, T.E. Milner, M.N. Deeter, Appl. Opt., 30 (**1991**) 1176-1178.

8.   F. Royer, D. Jamon, J.J. Rousseau, V. Cabuil, D. Zins, H. Roux, C. Bovier, Eur. Phys. J. Appl. Phys., 22 (**2003**) 83-87.

9.   T.Y. Kim, T. Hirano, Y. Kitamoto, Y. Yamazaki, IEEE Trans. Magn., 39 (**2003**) 2078-2080.

10.   Y.A. Bamakov, B.L. Scott, V. Golub, L. Kelly, V. Reddy, K.L. Stokes, J. Phys. Chem. Solids, 65 (**2004**) 1005-1010.

11.   K. Hayashi, R. Fujilkawa, W. Sakamoto, M. Inoue, T. Yogo, J. Phys. Chem. C, 112 (**2008**) 14255-14261.

12.   H.C.Y. Yu, M.A. van Eijkelenborg, S.G. Leon-Saval, A. Argyros, G.W. Barton, Appl. Opt., 47 (**2008**) 6497-6501.

13.   F.E. Moolekamp, K.L. Stokes, IEEE Trans. Magn., 45 (**2009**) 4888-4891.

14.   H. Uchida, Y. Masuda, R. Fujikawa, A.V. Baryshev, M. Inoue, J. Magn. Magn. Mater., 321 (**2009**) 843-845.

15.   D.A. Smith, K.L. Stokes, Opt. Express, 14 (**2006**) 5746-5754.

16.   Y.Q. Li, G. Zhang, A.V. Nurmikko, S.H. Sun, Nano Lett., 5 (**2005**) 1689-1692.

17.   B. Dong, X.W. Zhang, G.R. Han, Rare Metal Mat. Eng., 33 (**2004**) 31-34.

18.   P.K. Jain, Y.H. Xiao, R. Walsworth, A.E. Cohen, Nano Lett., 9 (**2009**) 1644-1650.

19.   P.K. Jain, M.A. El-Sayed, Nano Lett., 7 (**2007**) 2854-2858.

20.   P.K. Jain, M.A. El-Sayed, The Journal of Physical Chemistry C, 111 (**2007**) 17451-17454.

21.   S.J. Oldenburg, R.D. Averitt, S.L. Westcott, N.J. Halas, Chem. Phys. Lett., 288 (**1998**) 243-247.

22.   J.B. Jackson, N.J. Halas, J. Phys. Chem. B, 105 (**2001**) 2743-2746.

23.   R.D. Averitt, S.L. Westcott, N.J. Halas, J. Opt. Soc. Am. B: Opt. Phys., 16 (**1999**) 1824-1832.

24.   I. Edelman, J. Kliava, physica status solidi (b), 246 (**2009**) 2216-2231.

25.   See Supplementary Material at http://dx.doi.org/10.1063/1.3665138 for details of the theory of the Faraday rotation of nanoparticles.

26.   H. Inouye, K. Tanaka, I. Tanahashi, K. Hirao, Phys. Rev. B, 57 (**1998**) 11334-11340.

27.   L.B. Scaffardi, J.O. Tocho, Nanotechnology, 17 (**2006**) 1309-1315.

28.   D.A.G. Bruggeman, Ann. Phys., 417 (**1936**).

Chapter 4 - Pulsed magnetic field Faraday rotation

The Faraday rotation is known as a typical magneto-optical effect. Faraday effect is first discovered by Michael Faraday in 1945,[1] in which the plane of polarization of a light beam is rotated after transmitted through a dielectric medium when the magnetic field is applied in the direction of the propagation of light.[2]. The angle of rotation (φ) of plane of polarization of the light is given by;

$$\varphi = vBL \qquad\qquad\qquad 4.1$$

where B is the magnetic field, L is the path length of the dielectric medium, and v is the Verdet constant of the medium. Many reports have been reported on the Verdet constant of materials using alternating current magnetic field and direct current magnetic fields.[3-6] The physical meaning of the Verdet constant is magneto-complex birefringence, and it is given by the following equation, when the material has no absorbance at the observing wavelength;[7]

$$v = \frac{\omega}{2cB}(n_l - n_r) \qquad\qquad\qquad 4.2$$

where ω is the angular frequency, c is the velocity of light, n_l and n_r are the refractive indexes of the left and the right circularly polarized light.

Paramagnetic materials are commercially used in magneto-optical memory products and hence the Faraday rotation has been studied mainly for these materials.[8, 9] The measurement of the Faraday rotation of diamagnetic materials is very limited.[10] The Faraday rotation is thought to have unique information available in analytical chemistry, in that the magnetization can be monitored by light, since all substances have their own magnetic moments or magnetic susceptibilities, which could be used for the identification and speciation.[7] The electromagnet-based measurement requires an expensive and bulky electromagnet and a high current power supply to produce magnetic field of the order of a tesla or higher.[2] The alternative of the

alternating magnetic field is the pulsed magnetic field. Moreover, magnetic field is one of the important parameter that can be changed when performing an experiment. Many physical properties vary with some power of the magnetic field.[11] Sometime somewhere linearly or quadratically, and sometime occurs only after a certain threshold value. Higher field also provides higher resolution too. Therefore, it is important to try to increase the applied magnetic field maximum. Ordinary electromagnets cannot generate high magnetic field because of field saturation in ferromagnetic cores beyond which Joule heating occurs (due to high currents in the coils), limit the maximum field reached. Higher field can be generated with pulsed magnet because very high power is available from pulsed power supplies, and continuous cooling will no longer be a problem. Pulsed magnets use large current in air cored solenoids for a very short time interval which minimize Joule heating. However, the short time pulse is still longer on comparison to the time scales of electronic processes that occur in the materials. The time for the pulsed magnetic field is 10^{-2} s while the time for the electronic processes are usually orders of 10^{-14} to 10^{-9} s. Hence the material response can be treated as steady state to a great precision.[12] The main purposes of this experiment are the construction and calibration of pulsed magnetic field and then use the pulsed magnetic field to observe the magneto-optical Faraday rotation of Au, Fe_2O_3 and gold shell coated Fe_2O_3 NPs.

Construction of pulsed magnetic field

In 1924, the first pulsed magnetic field, close to 50 T, was developed by P. Kapitza from his lead acid storage battery through 1 mm bore and he was optimistic about obtaining 200-300 T if adequate financial means became available.[13] Pulsed magnets are used for two reasons: they can provide the highest fields and they can be made to fit a moderate budget. The generation of

pulsed magnetic field is important for several activities in the area of physical sciences. The basic components of a pulsed magnetic field are capacitor bank (C), power supply (V), spark gap (also called thyratron switch), inductor (L) and resistors (R). Basically, a pulsed magnetic field circuit is RLC (Resistor – Inductor – Capacitor) circuit. A simple schematic diagram for the pulsed magnetic field is shown in the Figure 4.1.
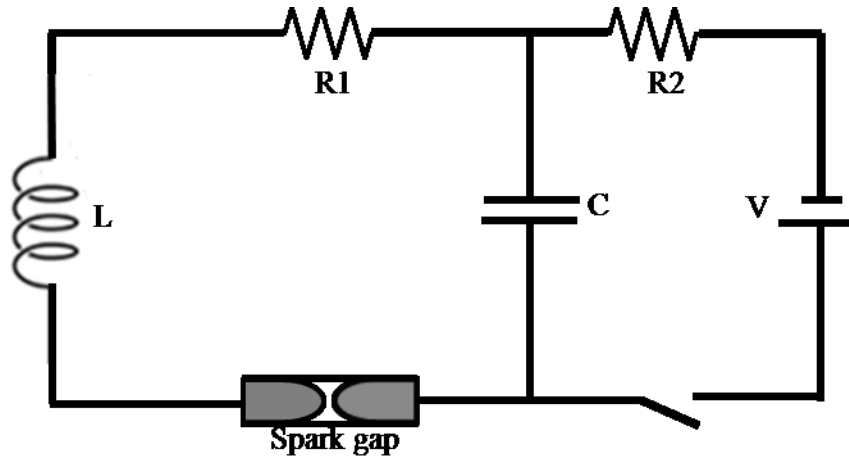
Figure 4.1 A schematic RLC diagram for pulsed magnetic field.

The capacitor bank is charged with a power supply. When the charged capacitor bank is discharged through the inductive coils for a short time, electric energy is transformed into magnetic energy.[14] The production of suitable shaped magnetic field requires a current to pass through a coil, but choosing the parameters of the coil is nontrivial because of trade-off between the magnetic field strength, the field homogeneity, and the inductance of the coil. Increasing the number of turns of the coil increases the field strength for a given current and increasing the diameter of the coil provides a larger region of the field uniformity but decreases the field strength. An increase in either the coil diameter or number of turns causes an increase in the inductance of the coil, and so for maximizing the rate of field switching, the number of turns and

coil diameter should be minimized.[15] A series of resistors controls the charging current. The value of $\pi\sqrt{LC}$ gives the duration of the pulse.[16]

The energy stored in the capacitor is deadly to humans if the capacitor is discharged through the human body. Therefore, it is very important to follow the safety steps to protect human life. A safety protocol is also prepared to operate the pulsed magnetic field which is attached in appendix.

Experimental setup

The experimental setup of the pulsed faraday rotation measurement is shown in the following Figure 4.2.
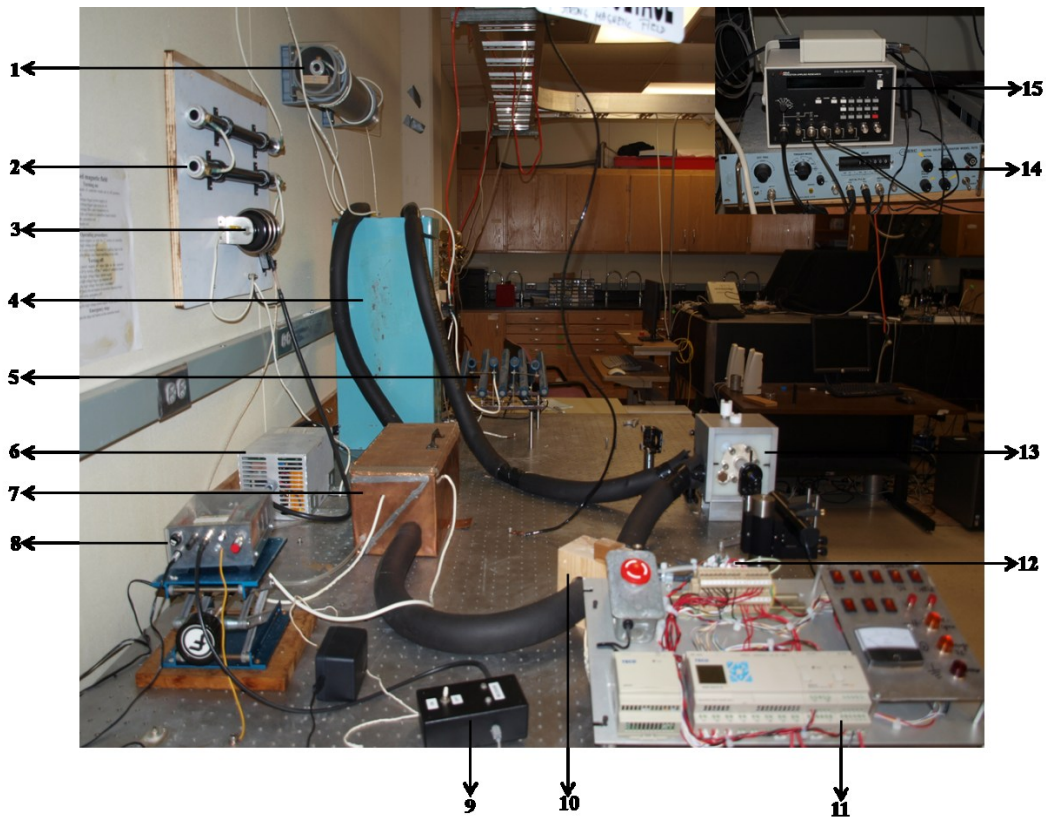
Figure 4.2 Experimental setup for pulsed magnetic field generator.

The setup consists of following parts:

1. Resistor (to discharge remaining charge)

2. Protective circuit (protect the power supply/charger from voltage reversal)

3. Diode (a part of protective circuit)

4. Capacitor bank

5. Current limiting resistor

6. Power supply/charger

7. Spark gap box

8. Trigger box (triggers the spark gap)

9. Fiber optic isolator (isolates low voltage component from high voltage component)

10. Current sensor (to calculate the magnetic field; $\int \frac{dI}{dt}$ gives current I(t) which is proportional to the magnetic field M(t)).

11. Programmable controller

12. Attenuator (reduces the amplitude of a single without distorting its waveform)

13. Coil (generates the pulsed magnetic field during discharge, and holds the sample)

14. Delay generator (provides precise delays for triggering. It has only microsecond precision with single channel, but experiment needs three channel)

15. Delay generator (nanosecond precision, not enough for the experiment)

The setup, located at Department of Chemistry, KSU, consists of a capacitor bank of 77.3 μF of Maxwell Laboratories which is charged by a power supply/charger of Lumina Power, Inc. The power supply uses 100-240 V AC-50/60 Hz input and output of 10kV@500 J/s in continuous operation. All the experimental operations are controlled by the computer programmable controller. The discharge energy can be calculated using the expression $\frac{1}{2}\,CV^2$.

Principally, the discharge of the capacitor bank to be critically damped which implies $R = 2\sqrt{L/C}$. The spark gap is the major resistance in the circuit, and most of the energy is dissipated through the spark gap during discharge and the remaining, maybe negligible, energy is used in the Joule heating of the coil.[16] A small spark gap gives the necessary resistance for the critical damping. Theoretically, the capacitor bank needs to be charged to cross the breakdown voltage of the spark gap. The breakdown voltage is the minimum voltage that causes a portion of insulator to become electrically conductive and complete the electric circuit. In our experiment the spark gap is fixed to approximately 2 mm and is triggered by using trigger box.

Experiment

Characterization of the magnetic field

Magnetic field of the setup is measured twice using water with two different discharge potential 3500 V, 5000 V and two different path lengths 3.0 cm and 2.6 cm, respectively. For the first measurement, the magnetic field is around 1.3 T and for the later measurement, the magnetic field is around 2.2 T. The variations of calculated magnetic field of the setup with time in these two measurements are shown in the Figure 4.3. The detail of the calculation for the magnetic field is attached in the appendix.
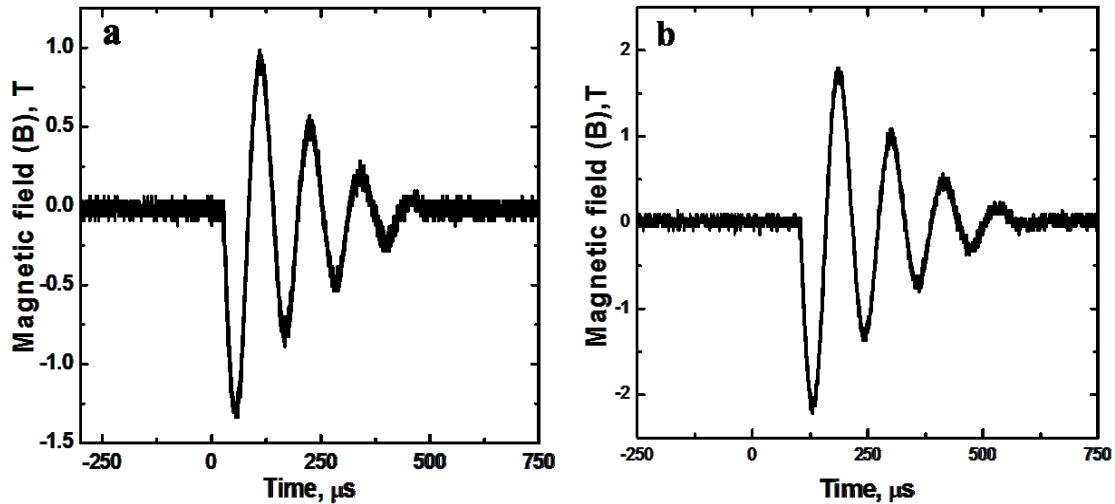
Figure 4.3 Variation of magnetic field with time using water (a) at discharge potential 3500 V with path length 3.0 cm and (b) at discharge potential 5000 V with path length 2.6 cm.

Laser power and discharged potential dependence of Faraday rotation

As our experiment showed, depending on discharge potential different magnetic field can be achieved. It is important to see the discharge potential dependence Faraday rotation. The discharge potential dependence of Faraday rotation is investigated using water in 3 cm long sample holder. A He-Ne laser (632 nm, 5 mW) is used as the source of light and a sheet polarizer is used to control the laser power. Investigation shows the linear dependence of Faraday rotation with the discharge potential. The experimentally measured Faraday rotations with their corresponding discharge potentials are shown in Figure 4.4(a).
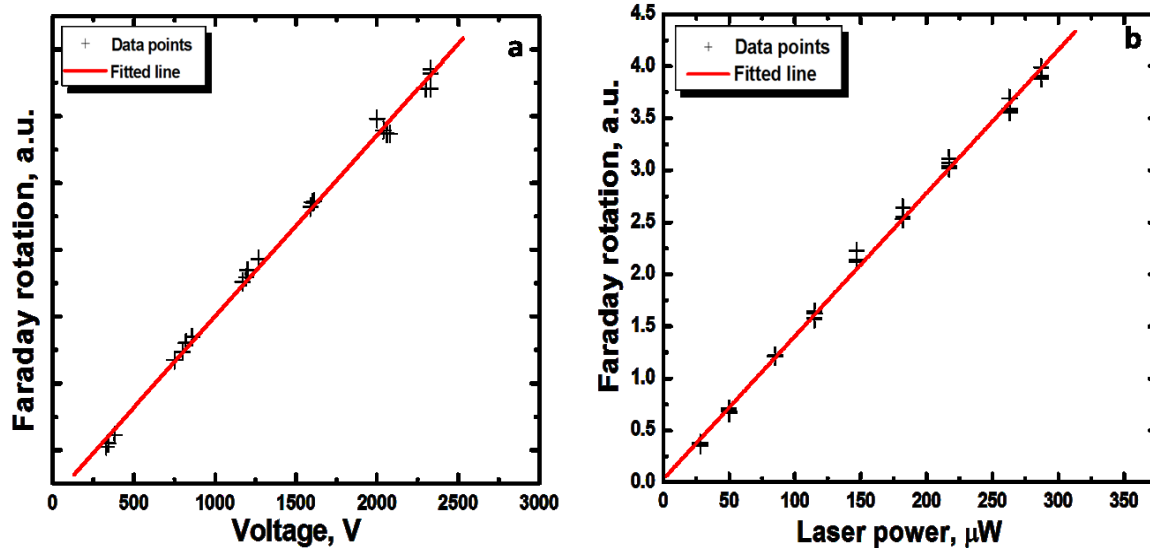
Figure 4.4 Relationship between (a) Faraday rotation and discharge potential, (b) Faraday rotation and laser power, cross points are the experimentally determined Faraday rotation and red line is the best fit line for the measured points.

In the similar way, the laser power dependence Faraday rotation is also investigated. Experimental investigation shows the Faraday rotation linearly depends on the laser power which is shown in Figure 4.4(b).

Faraday rotation of nanoparticles

For the experimental purpose, gold and iron oxide/gold nanoparticles, which are the same that used in pervious chapters, are used. These are large gold (17 nm) and Fe_2O_3 (9.7 nm) nanoparticles. The data are taken in 3 cm sample holder and at 3500 V discharge potential. The whole spectrum is recorded using Ocean Optics PX-2 Pulsed Xenon light source. The magneto-optical responses in terms of Verdet constant are shown in Figure 4.5. The measurement shows the maximum Faraday rotation around 520 nm for gold nanoparticles which corresponds to the

plasmon absorption peak wavelength for the gold nanoparticles. There is no such maximum Faraday rotation for Fe_2O_3 nanoparticles since there is no plasmon absorption peak maximum for Fe_2O_3.
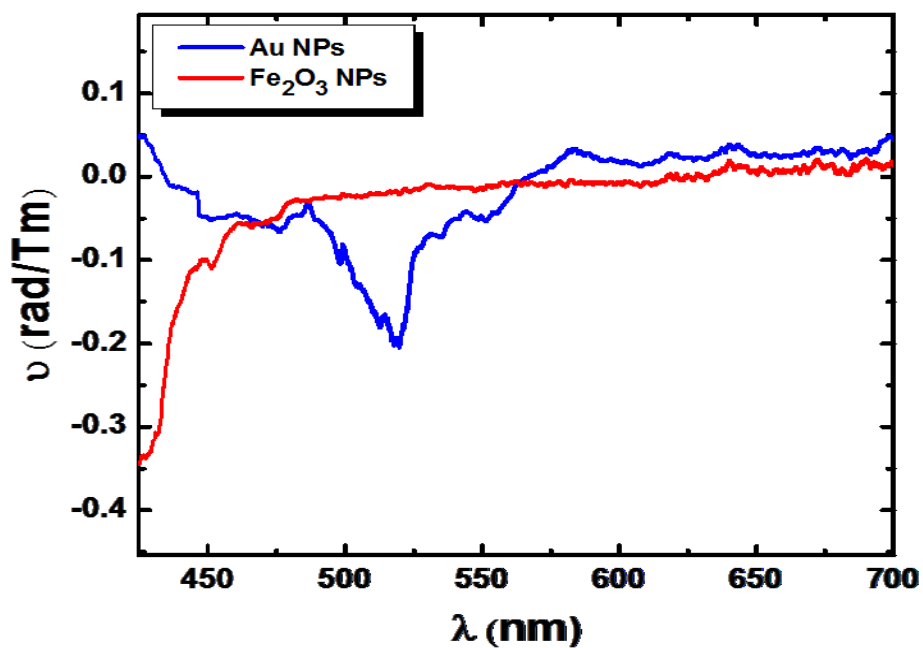
Figure 4.5 Faraday rotation of gold and Fe_2O_3 nanoparticles.

Similar type of Faraday rotation is obtained from the theoretical calculation using the Maxwell Garnett theory for both nanoparticles which is shown in Figure 4.6.
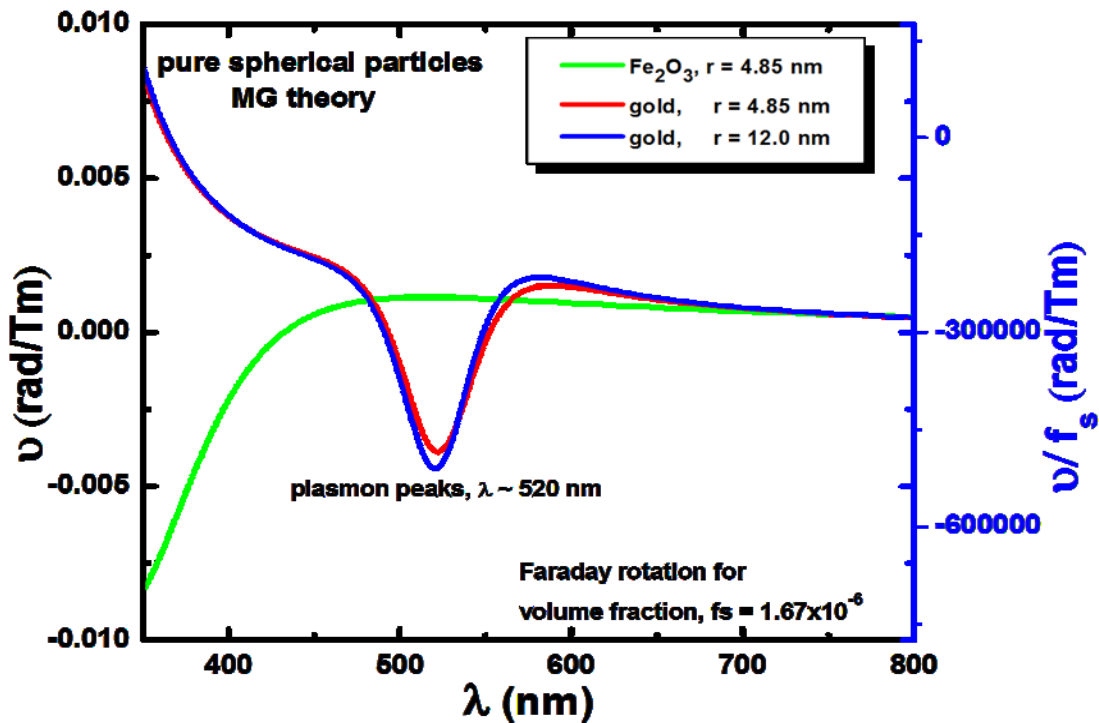
Figure 4.6 Faraday rotation in terms of Verdet constant calculated for nanoparticles indicated, in water solution, using the Maxwell Garnett theory at a volume fraction $f_s =$ 1.67 ×10^{-6} together with volume fraction normalized Faraday rotation.

The calculation shows the blue-shifting of the gold plasmon peak with increasing gold shell thickness is reflected in the Faraday rotation spectrum particles but there is no plasmon resonance for the Fe_2O_3 nanoparticles. The calculation accurately predicts the dip in the faraday rotation of the gold NPs at the plasmon resonance peak. This spectral feature is shifted for the gold coated nanoparticles to the red again as expected based on the calculation. On the other hand, experimentally obtained volume fraction normalized Faraday rotation data are shown in Figure 4.7. Volume fractions of NPs are calculated using concentration and TEM size of NPs. Data show unexpectedly far away from theoretically estimated values for both Fe_2O_3 and gold

NPs. It is very high for gold NPs and low for Fe_2O_3 NPs. This discrepancy between theory and experiment need to be resolved in the future. Commercially available materials with highest Verdet constant are Tb doped glass (69.81 rad/Tm), Terbium yttrium garnet (134.39 rad/Tm) and yttrium iron garnet (1605.70 rad/Tm) at 632 nm wavelength. The highest reported Verdet constant is 11344.64 rad/Tm for hybrid polythiophene-NP film at 830 nm.[17] Here, our measurement shows the Verdet constants for gold and Fe_2O_3 NPs are away from the theoretically expected values, and needs more investigation. The large Verdet constant of metal NPs relative to traditional materials could provide important applications of these particles as Faraday rotors.
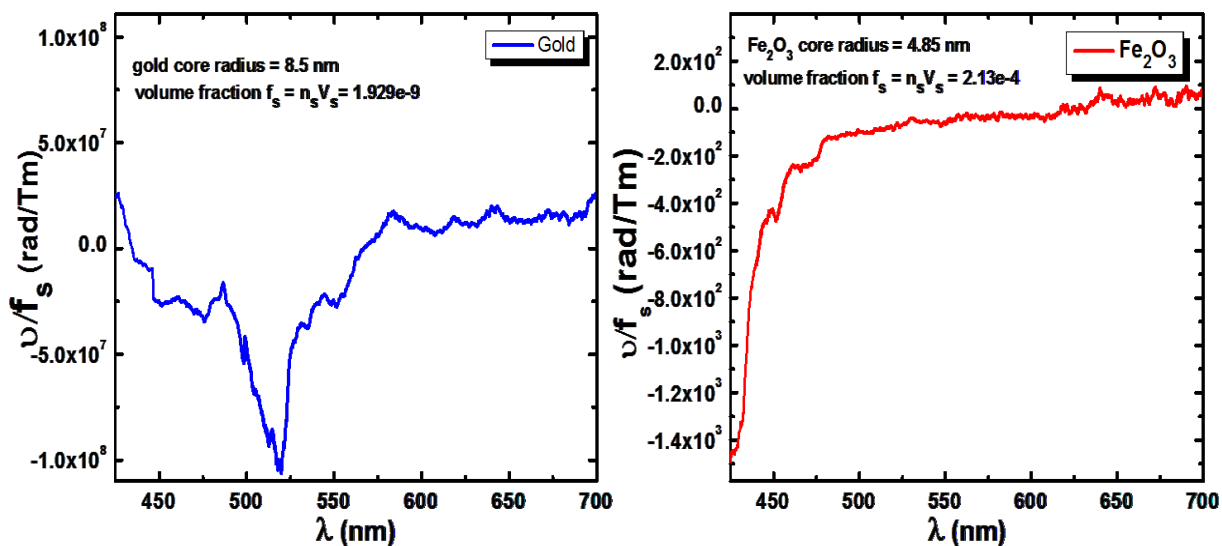
Figure 4.7 Experimentally obtained volume fraction normalized Faraday rotation for 17 nm gold (left) and 9.7 nm Fe_2O_3 (right) NP.

Faraday rotation of bare Fe_2O_3 and gold shell coated Fe_2O_3 nanoparticles are also measured under the same conditions. The measured Faraday rotation is shown in Figure 4.8.
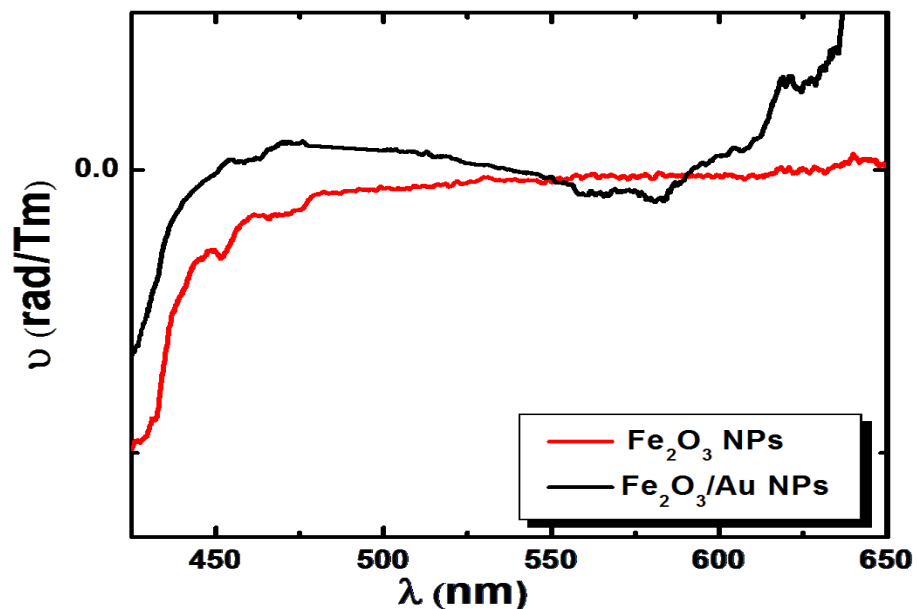
Figure 4.8 Faraday rotation of Fe_2O_3 and gold coated Fe_2O_3 nanoparticles.

A clear distinction can be seen in the Faraday rotation data. As bare Fe_2O_3 nanoparticles are coated with gold shell, the Faraday rotation spectrum started to increase in negative direction. If the thickness of the gold shell reached at a certain level, similar type of the Faraday rotation effect that is obtained from pure gold NPs can be expected. At that point, the NPs start to show the properties almost same to the pure gold NPs since the Fe_2O_3 is far from the surface of the NPs.

Conclusions

The pulsed magnetic field setup is constructed and calibrated. The magnetic field could be controlled by changing the discharge potential. Faraday rotation is linearly dependent on the discharge potential and laser power. Faraday rotation of nanoparticles in pulsed magnetic field is

also measured. The nature of experimentally measured Faraday rotation of NPs is similar to the nature of theoretically calculated Faraday rotation. However, the experimentally obtained Faraday data are perplexingly away from the theoretically estimated values. Further investigation is necessary to find out the reason behind such different values of Faraday rotation. The gold shell coated Fe_2O_3 nanoparticles start to show the similar type of Faraday rotation that observed for pure gold nanoparticles.

References

1. Hecht, E., *Optics*. Addison-Wesley: 2002.

2. Egami, S.; Watarai, H., *Rev. Sci. Instrum.* **2009,** *80* (9), 093705.

3. Wolfe, R.; Lieberman, R. A., *Appl. Phys. Lett.* **1991,** *58* (16), 1733-1735.

4. Turvey, K., *Rev. Sci. Instr.* **1993,** *64* (6), 1561-1568.

5. Bai, J. B.; Lu, G.; Lin, T., *Sensors and Actuators A* **2003,** *109*, 9-16.

6. Koerdt, C.; Rikken, G. L. J. A.; Petrov, E. P., *Appl. Phys. Lett.* **2003,** *82*, 1538-1540.

7. Isai, K.; Suwa, M.; Watarai, H., *Anal. Sci.* **2009,** *25* (1), 1-3.

8. Zhao, X. R.; Okazaki, N.; Konishi, Y.; Akahane, K.; Kuang, Z., *Appl. Surf. Sci.* **2004,** *223* (1-3), 73-77.

9. Sagnes, M.; Raquet, B.; Lassagne, B.; Broto, J. M.; Flahaut, E., *Chem. Phys. Lett.* **2003,** *372* (5-6), 733-738.

10. Botek, E.; Champagne, B.; Verbiest, T.; Gangopadhyay, P.; Persoons, A., *ChemPhysChem* **2006,** *7* (8), 1654-1656.

11. Frings, P.; Huang, Y. K.; Hennes, E., *Physica. B, Condensed matter* **2002,** *319* (1-4), 330-338.

12.   Murthy, O. V. S. N.; Venkataraman, V., *Rev. Sci. Instrum.* **2007,** *78* (11), 113905.

13.   Herlach, F., *Reports on progress in physics* **1999,** *62* (6), 859-920.

14.   Bartkevicius, S.; Novickij, J., *Elektronika Ir Elektrotechnika* **2009,** (4), 23-26.

15.   Salaoru, T. A.; Woodward, J. R., *Rev. Sci. Instrum.* **2007,** *78* (3).

16.   Mackay, K.; Bonfim, M.; Givord, D.; Fontaine, A., *J. Appl. Phys.* **2000,** *87* (4), 1996-2002.

17.   http://www.kuleuven.be/inpac/presentations/Wouters_WP6_INPAC.pdf.

Chapter 5 - (A) Complex formation between gold nanoparticles and MspA & MspA[cys]

Proteins are macromolecules with dimensions in the nanometer range that can be tailored to specific needs by site directed mutagenesis. Combining nanoparticles with proteins is desirable to extend the functionality and transferability of both proteins and nanoparticles. Nanoparticles have been successfully linked to antibodies,[1,2] aptamers,[3,4] and enzymes.[5,6] Extensive work has been done creating nanoparticle/ biomacromolecule complexes by many groups,[7-9] but challenges remain. Specifically, using protein/nanoparticle complexes has been severely hampered by the problem that most proteins lose their structural integrity in a non-native environment, limiting their potential use in many analytical and clinical procedures.[10]

The octameric porin A from *Mycobacterium smegmatis* (MspA) forms a homopore, which distinguishes itself by its extraordinary stability, suitable geometric dimensions, and an amphiphilic nature. This porin features a very hydrophobic docking unit that is able to penetrate virtually any cell membrane. When MspA is doped with a nanoparticle (NP) of suitable dimensions (< 5 nm in diameter), the resulting nanoparticle@MspA assembly will reconstitute within virtually all human (mammalian) cell membranes using the strongly hydrophobic "docking region" (see Figure 5.1). The geometric dimensions of this docking region are 3.7 nm in length and 4.9 nm in diameter.[11] In sharp contrast, the inner pore of MspA is hydrophilic.
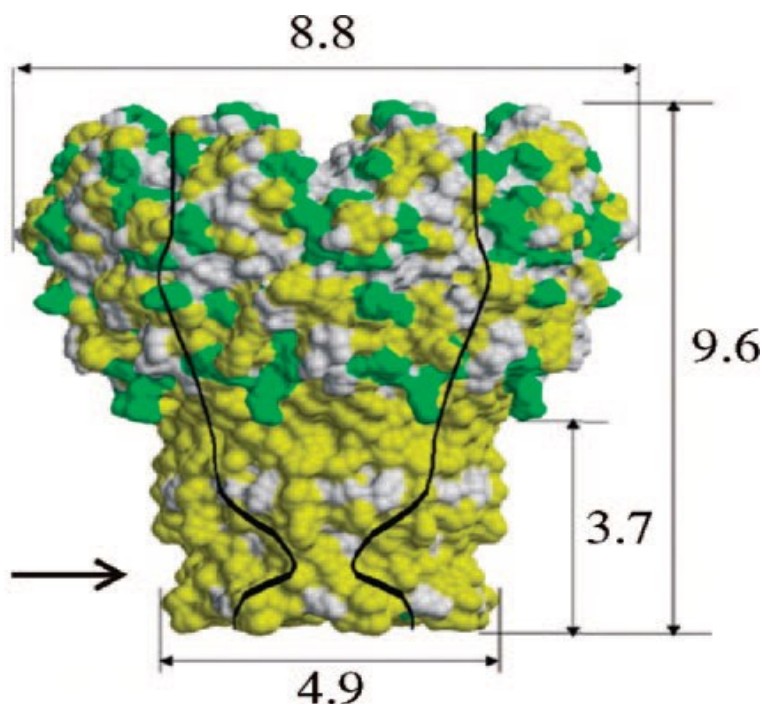
Figure 5.1 Crystal structure of MspA.[8] Surface representation (side view): green, hydrophilic amino acids; yellow, hydrophobic amino acids. Dimensions are given in nanometers. The position of the constriction zone ($d = 1$ nm) is marked with an arrow. The inner channel lining is indicated by black lines.

The diameter of the inner pore changes from 4.8 nm at the pore's entrance to 1.0 nm at its constriction zone (bottleneck). Due to the strong binding of hydrophilic functional groups to the surface of gold (and other metal) nanoparticles, the inner pore can act as host for nanoparticles of suitable size. In order to test the potential of this porin to dock nanoparticles, two different sizes of gold nanoparticles are synthesized. Thiols are known to bind most strongly to gold surfaces and to competitively displace other functional groups, such as amines and carboxylates. Therefore, the effect of a cysteine mutant of MspA (Q126C, henceforth abbreviated as MspA[cys]) is also investigated on the binding of gold nanoparticles.
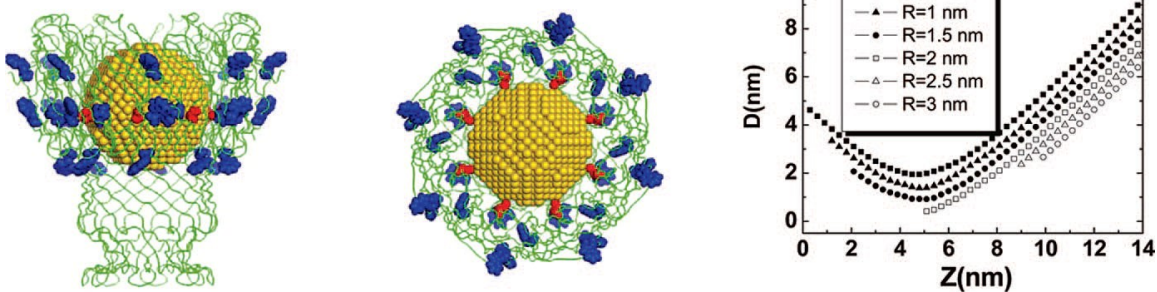
Figure 5.2 (a) The optimal arrangement for a nanoparticle of radius 2 nm. The closest S - Au distance is 0.42 nm. Gray represents the C^{α} backbone, gold the Au sphere, blue the Trp, and red the Cys 126. (b) The distance (D) of the nearest Au atom of the nanoparticle to the C^{β} of residue 126 as a function of distance from the base of the porin (Z) along the central axis of the porin. The origin ($Z = 0$) is defined by the C^{α} position of each D91 residue. The lines correspond to spherical Au nanoparticles of varying radius (R), and the horizontal line is the optimal C^{β}-Au distance (0.33 nm) required for S-Au bond formation (0.24 nm). Curves are truncated when an Au atom is located within 0.3 nm of a backbone or C^{β} atom of the porin (steric overlap). An optimal arrangement is observed for a nanoparticle of radius 2 nm (containing 1956 atoms) located at $Z = 5.1$ nm with a C^{β}-Au distance of $D = 0.42$ nm.

Our Au@MspA adducts are intended for plasmonic hyperthermia[12] experiments and serve as model compounds for magnetic hyperthermia experiments.[2] Compared to other methods for treating cancer, such as chemotherapy and radiation, hyperthermia has profound advantages: (A) When heated above 45°C, mammalian cells die because of protein misfolding, impairing DNA transcription, and many other metabolic functions.[13] Furthermore, the kinetic energy of the phospholipids in the cell membrane can exceed the hydration energy barrier, which holds them within the supramolecular assembly of the membrane. The membrane of mammalian cells at 43°C dissolves in the surrounding aqueous buffers, rendering the membrane freely permeable to small ions. This process leads to either necrosis (leakage of the cell components in the human

body) or apoptosis, depending on the amount of ion influx into the cytoplasm and the efficacy of the cellular repair mechanisms, which can be also impaired by hyperthermia.[14] (B) Heat is not toxic and will not destroy too many healthy cells, if the heating can be restricted to the tumor region(s) with precision. With nanoparticles, heating can be either induced by multiphotoabsorption at 800 nm,[15] where human tissue is almost transparent and does not scatter significantly,[16] or by the application of a local AC field when magnetic nanoparticles are used.

Experiment details

Chemicals and Porins

Hydrogen tetrachloroaurate(III) trihydrate (HAuCl$_4$·3H$_2$O, 99.99%), sodium borohydride (NaBH$_4$, 98%), mercaptosuccinic acid (98%), abbreviated as MSA, methanol, *n*-octylpolyoxyethylene, and sodium citrate (Na$_3$C$_6$H$_5$O$_7$·2H$_2$O). MspA and a mutant of MspA possessing a cysteine residue in position 126 (MspA^{cys}) were generous gifts from Professor Michael Niederweis, Department of Microbiology at the University of Alabama at Birmingham.

Synthesis of Gold Nanoparticles

Small gold nanoparticles were synthesized by the method described by Chen and Kimura *et al.*[17] Briefly, a mixture of 197 mg of HAuCl$_4$ is dissolved in 4 mL of doubly distilled water and 187.68 mg of MSA dissolved in 100 mL of methanol is prepared under inert atmosphere. A solution of NaBH$_4$ (189.15 mg of NaBH$_4$ in 25 mL of water) is slowly added at the rate of 2 mL/min. The solution is then stirred for 1 h. Finally, a dark-brown precipitate of gold nanoparticles is formed. The gold nanoparticles are centrifuged at 8500 rpm for 10 min to obtain a residue of nanoparticles. The nanoparticles are washed twice with 20% (v/v) water/methanol mixture once with pure methanol. The nanoparticles are dried in vacuum. The nanoparticles are easily soluble in water.

The large gold nanoparticles are prepared from the reduction of $HAuCl_4$ solution by sodium citrate solution as described by Turkevitch *et al.*[18] Briefly, 5 mg of $HAuCl_4$ and 50 mg of sodium citrate are dissolved in 95 and 5 mL of doubly distilled water, respectively. The $HAuCl_4$ solution is heated to about $70^{\circ}C$, the sodium citrate solution is added, and the mixture is vigorously stirred for 50 min. The color of the solution gradually changes from faint pink to wine red, which contains the required nanoparticles.

Transmission Electron Microscopy

The sizes of the different nanoparticles are determined with TEM. This is achieved using a Philips CM-200 TEM, operating at 100 kV. A small fraction of the nanoparticle solution is diluted to one-fifth of its original volume, and a drop of the diluted solution is spread over a copper grid (300 mesh size) supporting a thin film of amorphous carbon. To reduce the damage from the electron beam, the sample is cooled to liquid nitrogen temperature during data collection. TEM images and size distribution of both types of nanoparticles are shown in Figure 5.3. According to TEM analysis, the average size of the small nanoparticles is 3.7 ± 2.6 nm and large nanoparticles is 17 ± 3 nm.
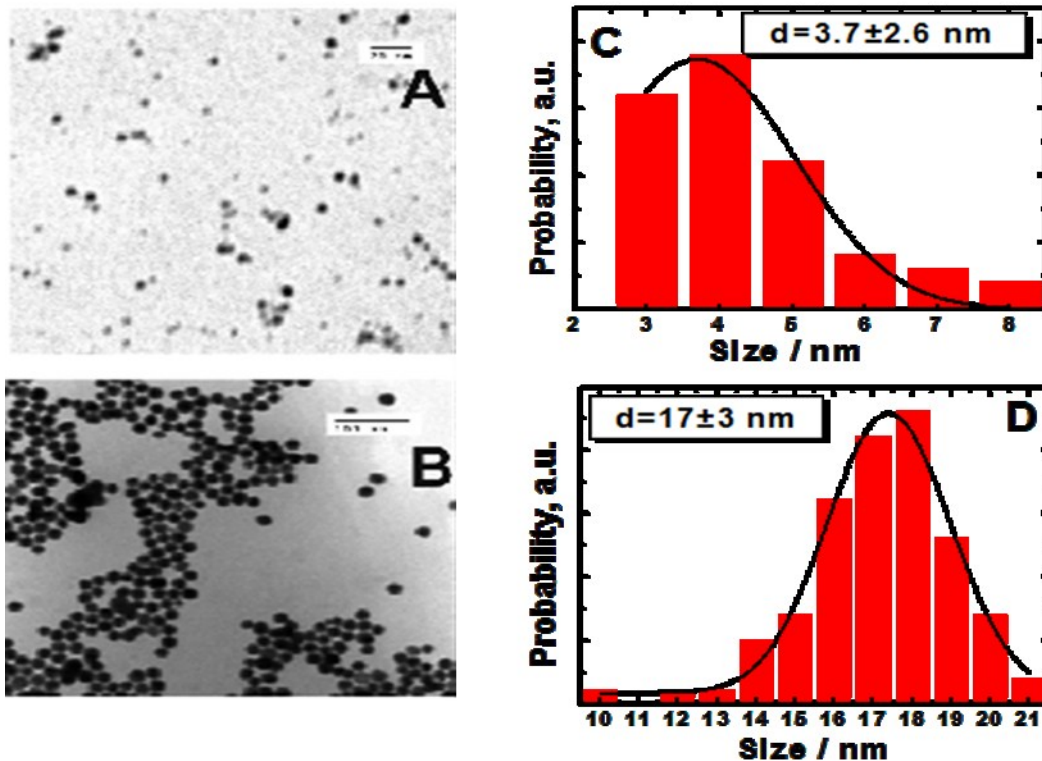
Figure 5.3 Representative TEM images of the gold nanoparticles used in the experiment. (A) TEM image of small nanoparticles. (B) TEM image of large nanoparticles. The size histograms indicating the average size and size distribution of the gold nanoparticles are shown in (C) and (D), respectively.

Neutron Activation Analysis of Gold Nanoparticles

The concentration of gold nanoparticles in the solution state is measured by means of neutron activation analysis (NAA). In this process, a sample and a standard sample are activated by neutrons under the same conditions. The specific activity of the samples is then measured. The activity of the samples after irradiation is directly proportional to the amount (concentration) of isotope present in the sample. The ratio of the specific activity to concentration of both samples is equal. From this relationship, and using the average nanoparticle sizes determined by the transmission electron microscopy (TEM) analysis, the concentration of gold nanoparticles in a

solution is calculated. The concentrations of small and large nanoparticles are 3.67×10^{-8} mol/L and 1.13×10^{-11} mol/L respectively.

Modeling of Nanoparticle and MspA Complexes

A series of calculations are performed using the porin octamer coordinates obtained from the crystal structure of MspA (PDB code: 1UUN). First, a gold face-centered cubic lattice is constructed using the experimental Au-Au contact distance of 0.288 nm.[19] Spherical Au nanoparticles of varying diameter are then isolated from the lattice. The center of mass of each nanoparticle is then moved along the central axis of the porin corresponding to various distances (Z) from the constriction site. A complex is rejected if any Au atom is located within 0.3 nm of any porin backbone (N, C^{α}, C, O) or C^{β} atom. The distance (D) of the nearest Au atom to the C^{β} atom of the Q126 residue is then determined as a function of Z. Assuming bond lengths for the C^{β}-S and S-Au bonds of 0.182 and 0.24 nm, respectively, together with a C^{β}-S-Au bond angle of 100°[20] suggests an optimal C^{β}-Au distance of 0.33 nm for the formation of S-Au covalent bonds.

MspA Porin/Gold Complex

Nanoparticle/protein complexes represent a unique class of materials that are able to increase the functionality of the individual components. We have assessed the ability of the very stable porin (MspA) from *M. smegmatis* to bind two very differently sized gold nanoparticles in the hydrophilic inner pore. The binding of the gold nanoparticles has been probed by observing the fluorescence and phosphorescence of tryptophan molecules positioned in the protein (Figure 5.2(a)). MspA contains eight identical amino acid chains. Each MspA chain is composed of 184 amino acid residues and contains four tryptophan fluorophores at positions 21, 40, 72, and 181. The positions of the 32 tryptophans of the MspA are shown in Figure 5.2(a). In order to

determine the geometrical requirements for the formation of a gold nanoparticle and MspA complex (Au@MspA) a series of calculations are performed using the porin octamer coordinates obtained from the crystal structure (PDB code: 1UUN). Figure 5.2 predicts that the optimal size for the complex formation involves a nanoparticle with a diameter of 4 nm. A larger diameter will not fit into the porin, while a smaller diameter will not be able to covalently attach to all eight C126 residues simultaneously. Smaller Au clusters could enter and bind asymmetrically-although their ability to totally block the porin would be reduced substantially. The figure also suggests that a 4 nm diameter Au nanoparticle should form a complex with its center approximately 5.1 nm away from the constriction zone and with Au atoms within 0.42 nm of the C^β of residue 126. While this is slightly larger than the optimal distance of 0.33 nm (see Methods), covalent attachment can easily be accommodated by small, but benign, changes in the porin structure. The covalent attachment to C126 is predicted to occur around the equator of the nanoparticle. Finally, we note that in the above complex the closest tryptophan to Au distances are approximately 2.5, 1.1, 1.4, and 2.0 nm for residues 21, 40, 72, and 181, respectively.

The average sizes of small and big gold nanoparticles are 3.7 ± 2.6 and 17 ± 3 nm respectively. The respective sizes of the gold nanoparticles used in our experiments are both smaller and larger than the channel opening of MspA, which is 4.8 nm. It is apparent from these data that the larger gold nanoparticles are unable to fit into channel opening or even the outer pore of MspA. However, the sample of smaller gold nanoparticles feature a significant fraction that is less than 4.8 nm in diameter. Fortunately, nanoparticles with diameters of 4.0 nm correspond to the most common particle size synthesized for the small Au clusters. Our experiments are based on the mechanistic paradigm that the smaller gold nanoparticles are in close proximity to the tryptophan side chains at positions 21, 40, 72, and 181. Hence, this will

result in different spectral features than for larger nanoparticles which have to remain outside of the central pore of MspA.

Stationary luminescence experiments of the Au@MspA complexes have been performed. The goal of these experiments is to confirm the presence of Au@MspA complexes when using smaller nanoparticles and to discern the effect of the various sized gold nanoparticles on the tryptophan emission. Furthermore, the effect of the cysteine mutant MspA[cys] on the binding of gold nanoparticles is studied by luminescence spectroscopy. MspA[cys] contains a ring of eight thiol groups within the pore that are only accessible to the smaller gold nanoparticles.

It is well-known that the photoluminescence of a fluorophore is greatly affected by the presence of a metal surface. Briefly, the presence of a metal surface affects the radiative and nonradiative rates of fluorescence and phosphorescence as well the rate of light absorption.[21] These effects are even more pronounced with metal nanoparticles when their surface plasmon resonance is close to the transition of the fluorophore. Qualitatively, the quenching of fluorescence is most significant if the fluorophore is within a few nanometers of the surface of the metal nanoparticle. For example, the effect of fluorescence quenching dominates up to a distance of approximately 5 nm from the nanoparticle surface. On the other hand, at distances between 5–20 nm, fluorescence enhancement is the dominant mechanism.

Both MspA and MspA[cys] possess several amino acids that contribute to the total luminescence of the protein. The strongest emitting fluorophore of MspA is tryptophan.[22] The spectrum features a strong absorption band at 280 nm (Figure 5.4).
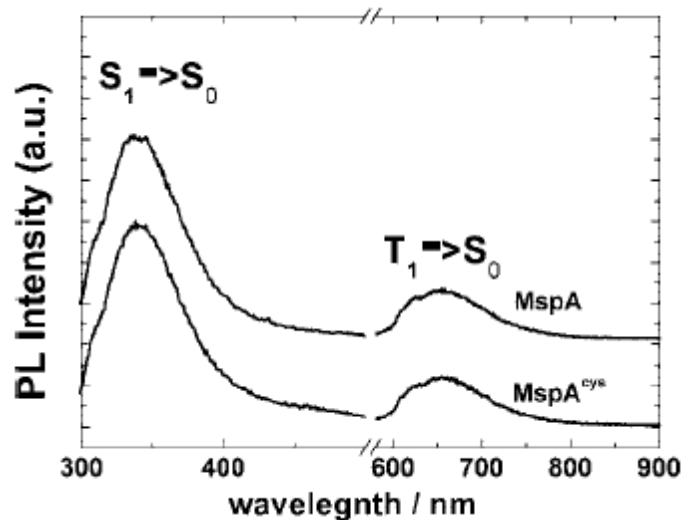
Figure 5.4 Fluorescence ($S_1 \rightarrow S_0$) and phosphorescence ($T_1 \rightarrow S_0$) spectra of the MspA and MspA^{cys}. The peak originates from the 32 tryptophans[8] present in the proteins. The samples are photoexcited at 280 nm.

The fluorescence emission of tryptophan is centered at around 350 nm. The quantum yield (Φ) of this primary fluorescence is known to vary between approximately $\Phi = 0.20$ and $\Phi = 0.80$, depending on protein conformation and environment.[23]

The fluorescence emissions occurring from the excitation ($\lambda = 280$ nm) of the tryptophans of MspA in the presence and absence of the small and large gold nanoparticles are summarized in Figure 5.5. In all cases the fluorescence emission band is centered around 350 nm. Both MspA and MspA^{cys} show similar trends; however, the observed fluorescence quenching by the small gold nanoparticles is more pronounced in MspA^{cys}, whereas the fluorescence enhancement by the larger gold nanoparticles is less distinct. Note that the concentrations of MspA and of the gold particles of the same size are exactly the same, permitting us to draw direct comparisons of their photophysical behavior. The absorption cross section of the large nanoparticle is greatly increased, which could cause large self-absorption effects, making the comparison of the protein

and Au@MspA complexes difficult. Therefore, the concentration of the large gold nanoparticles is chosen to be significantly smaller than that of the small gold nanoparticles. In parts (a) and (c) of Figure 5.5, the fluorescence of MspA (a) and MspA^{cys} (c) by the small gold nanoparticles drops to $55 \pm 20\%$ and $24 \pm 20\%$ of its initial value, respectively. In parts (b) and (d) of Figure 5.5 the fluorescence enhancements (I/I_0) of MspA (b) and MspA^{cys} (d) caused by the larger gold nanoparticles are $270 \pm 20\%$ and $130 \pm 20\%$, respectively.
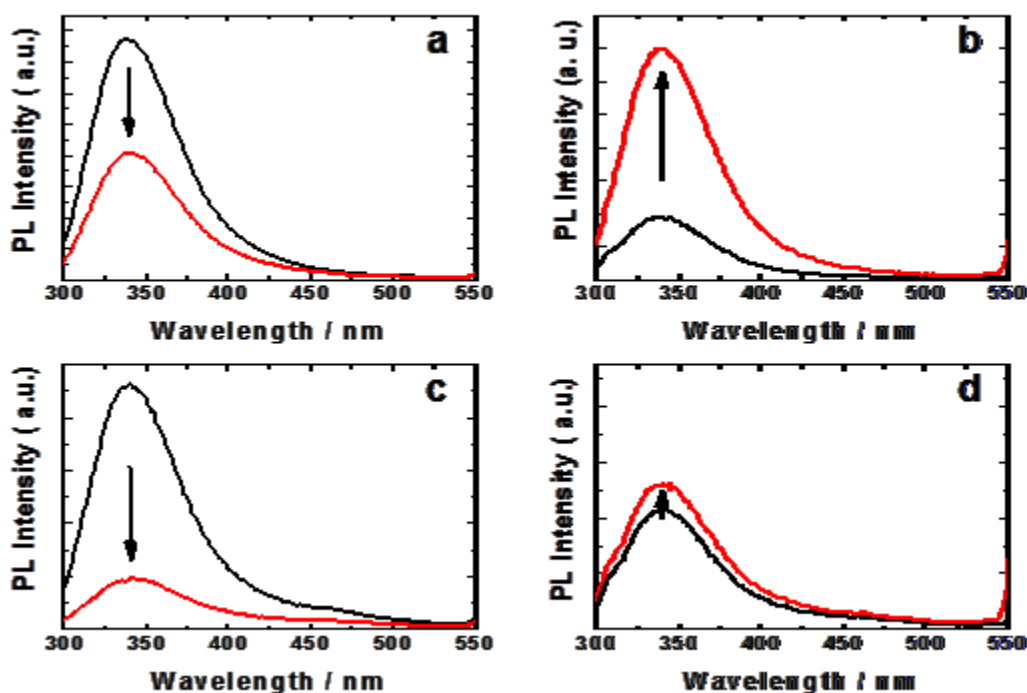
Figure 5.5 Fluorescence spectra of MspA before (black line) and after (red line) the addition of small (a) and large (b) gold nanoparticles to the protein solution. Fluorescence spectra of MspA^{cys} before (black line) and after (red line) the addition of small (c) and large (d) gold nanoparticles to the protein solution. The concentration of MspA and MspA^{cys} in the solution is 1.09×10^{-9} mol/L. The concentration of the small and large gold nanoparticles in solutions is 3.67×10^{-8} and 1.13×10^{-11} mol/L, respectively. The excitation wavelength is 280 nm.

Interestingly, only freshly prepared small gold samples exhibited quenching of the fluorescence of MspA. After aging for a month, the small gold nanoparticle samples induce increased tryptophan emissions, very similar to the large gold nanoparticle which is shown in the following Figure 5.6.
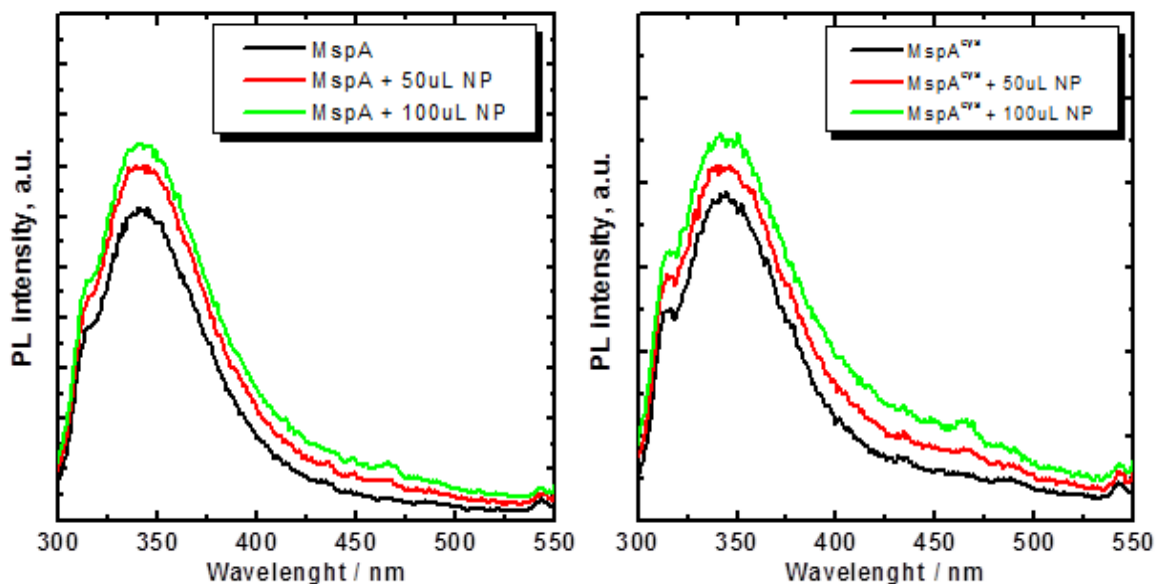
Figure 5.6 Tryptophan emissions of MspA (left) and MspA^{cys} (right) with small gold NPs after aging for a month.

We speculate, that the cause for this effect is most likely the aging (Ostwald ripening) of the gold nanoparticles, which increases the fraction of bigger particles and consequently reduces the proportion of the very small gold particles. Stability of the nanoparticles is tested through the measurement of the zeta-potential of nanoparticles colloids. The zeta-potentials of colloids are measured using four detectors from four different angles. The measured zeta-potentials for both small and large gold nanoparticles are shown in the following Figure 5.7.

104
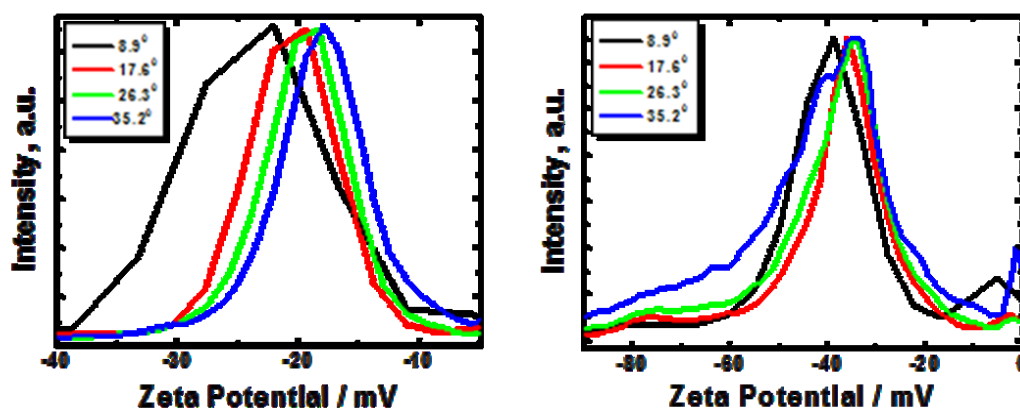
Figure 5.7 Zeta-potential of small (left) and large gold (right) nanoparticles.

The average zeta-potential of small gold nanoparticles is -20 mV which indicates that these nanoparticles are unstable. The instability of colloidal solution leads the nanoparticles to aggregate and forms larger nanoparticles. Therefore, the small gold nanoparticles start to show similar behavior that is shown by larger nanoparticles. The average zeta-potential of big nanoparticles colloid is -45 mV which is comparatively more stable than small gold nanoparticles.

A more detailed comparison of the fluorescence data is shown in Figure 5.8. The fluorescence spectra of the previous data (shown in Figure 5.5) are normalized to the peak maximum at 350 nm to observe changes in the fluorescence peak shape. Clearly discernible changes occur when assemblies between MspA^{cys} and the smaller nanoparticles are formed. The spectra of the wild-type MspA before and after the addition of nanoparticles differ much less than those for MspA^{cys}. Interestingly, the red side of the tryptophan fluorescence is less affected. The difference spectra between the small gold Au@MspA^{cys} and the MspA^{cys} indicate a fluorescence peak centered at about 370 nm. On the basis of previous observations, the 370 nm peak corresponds most likely to those tryptophan molecules that can be found in a polar

(aqueous) environment.[24] On the basis of this observation, the most likely location of these particular tryptophans is at position 181, which is located near the porin's "rim" and, therefore, exposed to a polar environment. In sharp contrast, no changes of the peak shapes are observed for the complexes of MspA with the larger gold nanoparticles. (Figure 5.8, panels (b) and (d)).
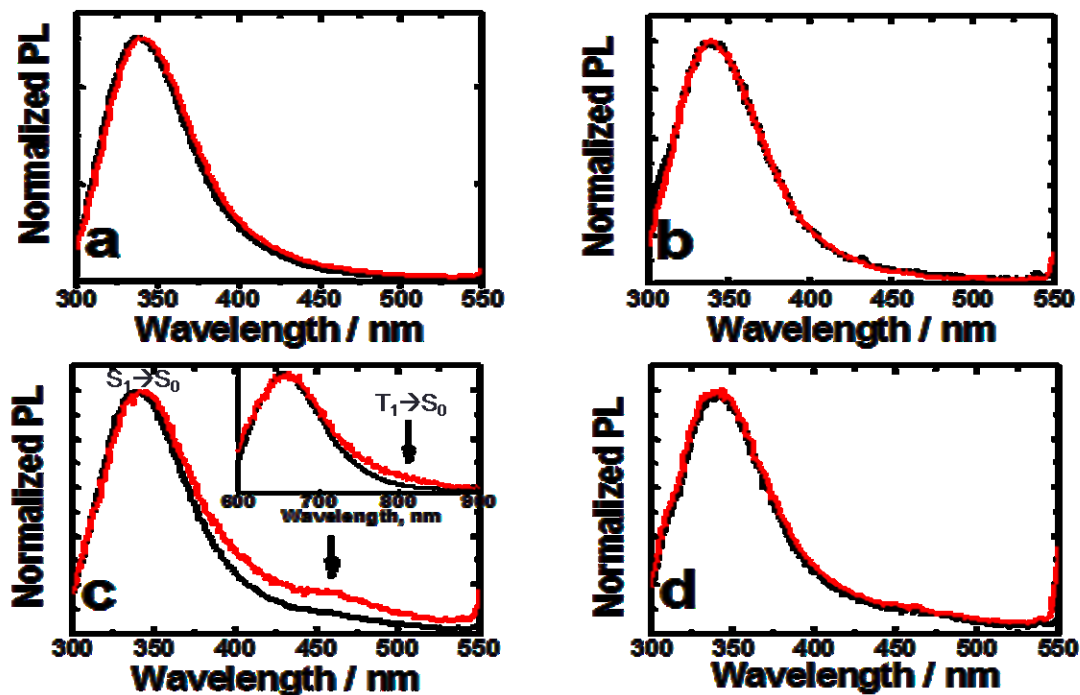
Figure 5.8 Same as Figure 5.5, but the fluorescence is normalized to the peak maximum. Panel (c) inset shows the $T_1 \rightarrow S_0$ transition of the MspA^{cys} before (black line) and after (red line) addition of small gold nanoparticles to the protein solution. The arrows indicate the position of the relative increase of fluorescence in the spectrum.

Finally, a second photoluminescence experiment is carried out to excite the nanoparticles at a wavelength where no appreciable absorption of the MspA protein takes place. The previously described combinations of the MspA proteins and the smaller and bigger gold nanoparticle samples are shown in Figure 5.9. However, excitation is performed this time at 500

nm. The data presented in parts (a) and (c) of Figure 5.9 show that the assemblies of the small gold nanoparticles with MspA feature emission of the protein's tryptophans corresponding to the $T_1 \rightarrow S_0$ transition around $\lambda = 775$ nm (phosphorescence).[24] The occurrence of phosphorescence is a strong indication that the nanoparticle and protein are indeed in close contact.[25] Interestingly, the complexes between the large gold nanoparticles and MspAs do not show the same effect. Note that the sharp features at approximately 550 and 600 nm are Raman lines of the solvents. The fluorescence of both gold nanoparticles in aqueous solution is found to be negligible.
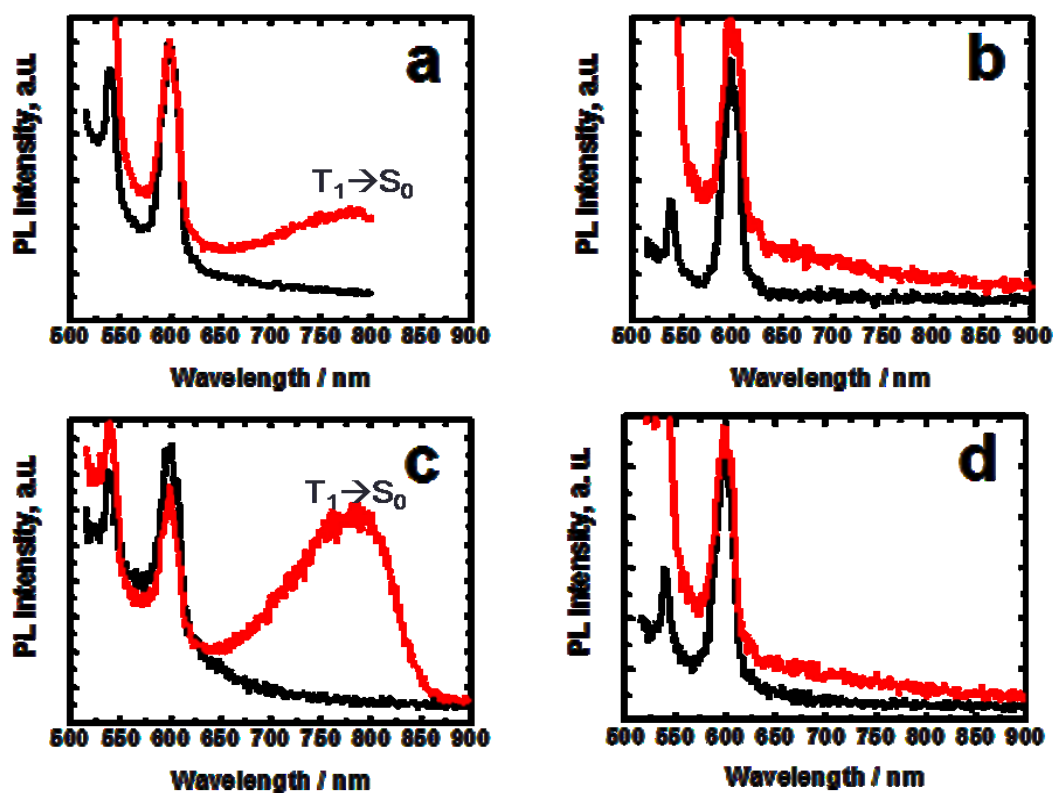
Figure 5.9 Photoluminescence spectra of MspA before (black line) and after (red line) the addition of small (a) and large (b) gold nanoparticles to the protein solution. Photoluminescence spectra of MspA^{cys} before (black line) and after (red line) the addition of small (c) and large (d) gold nanoparticles to the protein solution. The concentrations of

protein and nanoparticles are the same as before. The sharp features are Raman lines of the solvents. The photoluminescence of only gold nanoparticle solution (not shown) is negligible in the solution.

The observed differences with respect to the occurrence of phosphorescence are due to the location of the nanoparticles attached to MspA. Whereas the smaller gold nanoparticles permit their binding within the pore of MspA, the larger nanoparticles have to be bound at the exterior of MspA due to size exclusion. The observed phosphorescence quenching of the MspA's tryptophan units can be regarded as mechanistic proof of the proximity of the excited gold NP and at least some tryptophan units within the NP@MspA assembly. On the other hand, the observed fluorescence enhancement of the excited tryptophan units in the presence of the bigger gold nanoparticles clearly suggests that some kind of binding must take place as well. In principle, fluorescence quenching could be expected if there is only a single fluorophore in the protein even in the case of a big nanoparticle, but there are 32 tryptophans present at various distances from the large gold nanoparticles since no docking takes place. In addition, the presence of large gold nanoparticles may interrupt the energy transfer network of tryptophans. Clearly, in the case of docked small gold nanoparticles, distance distribution is more symmetric relative to the metal surface. An important question is where the nanoparticles are relative to the MspA and MspA^cys. When the protein is anchored on mica, the nanoparticles are bound to the MspA from the TOP for both small and large nanoparticles.[26]

High-Performance Liquid Chromatography (HPLC) Separation of the Au@MspA Complexes

The binding constants of both of the small and large gold nanoparticles bound to MspA are measured by HPLC (Shimadzu Prominence) employing a POROS HQ/20 anion exchange

column and a flux of 0.50 mL min^{-1}. Two buffers are used: AOP05 (25 mM HEPES, pH 7.5, 10 mM NaCl, 0.5% OPOE) and BOP05 (25 mM HEPES, pH 7.5, 2 M NaCl, 0.5% OPOE). A typical gradient is 100% AOP05 (0–5 min), followed by a linear gradient to 100% BOP05 (5–35 min). The eluent is kept at 100% BOP05 (35–50 min). Finally, the salt concentration is returned linearly to 10 mM (100% AOP05) (50–60 min). The stop rime is set at 65 min. Peak detection is achieved using UV-vis (diodearray).

In order to estimate the binding constants between MspA and the smaller and bigger gold nanoparticles, a HPLC procedure is used that had been originally developed for the purification of MspA. In Figure 5.10, two typical HPLC chromatograms belonging to MspA and the supramolecular adduct of small gold nanoparticles and MspA are shown. The two peaks of MspA at 16.4 and 20.8 min occur due to hydrophobic clustering of MspA; at higher surfactant concentration, only one peak is discernible (at 16.9 min). However, we would like to compare HPLC chromatograms that have been obtained under exactly the same experimental conditions.

It is known from the HPLC purification of other MspA adducts (e.g., dihydroindolizines as optical switches[27] within the inner pore or ruthenium(II)-quaterpyridinium complexes as channel blockers[28]) that the closing of the inner MspA pore leads to a significant shift of the observed retention time. They can be found between 1.5 and 3.0 min, depending on the channel blockers used. We interpret the finding reported here as independent proof for the binding of the small and the big NPs to MspA. In both cases, the channel is blocked by either binding within (small NPs) or on top of MspA (big NPs).

$$K_B = \frac{[Au@MspA]}{([Au]^0 - [Au@MspA])([MspA]^0 - [Au@MspA])} \qquad 5.1$$

, where K_B is the binding constant, [Au@MspA] is the concentration (mol/L) of the supramolecular assembly of small or big gold nanoparticles and MspA, $[MspA]^0$ is the

concentration of MspA (mol/L) in the absence of NPs, and $[Au]^0$ is the starting concentration of the nanoparticles (mol/ L). The results are summarized in Table 5.1.
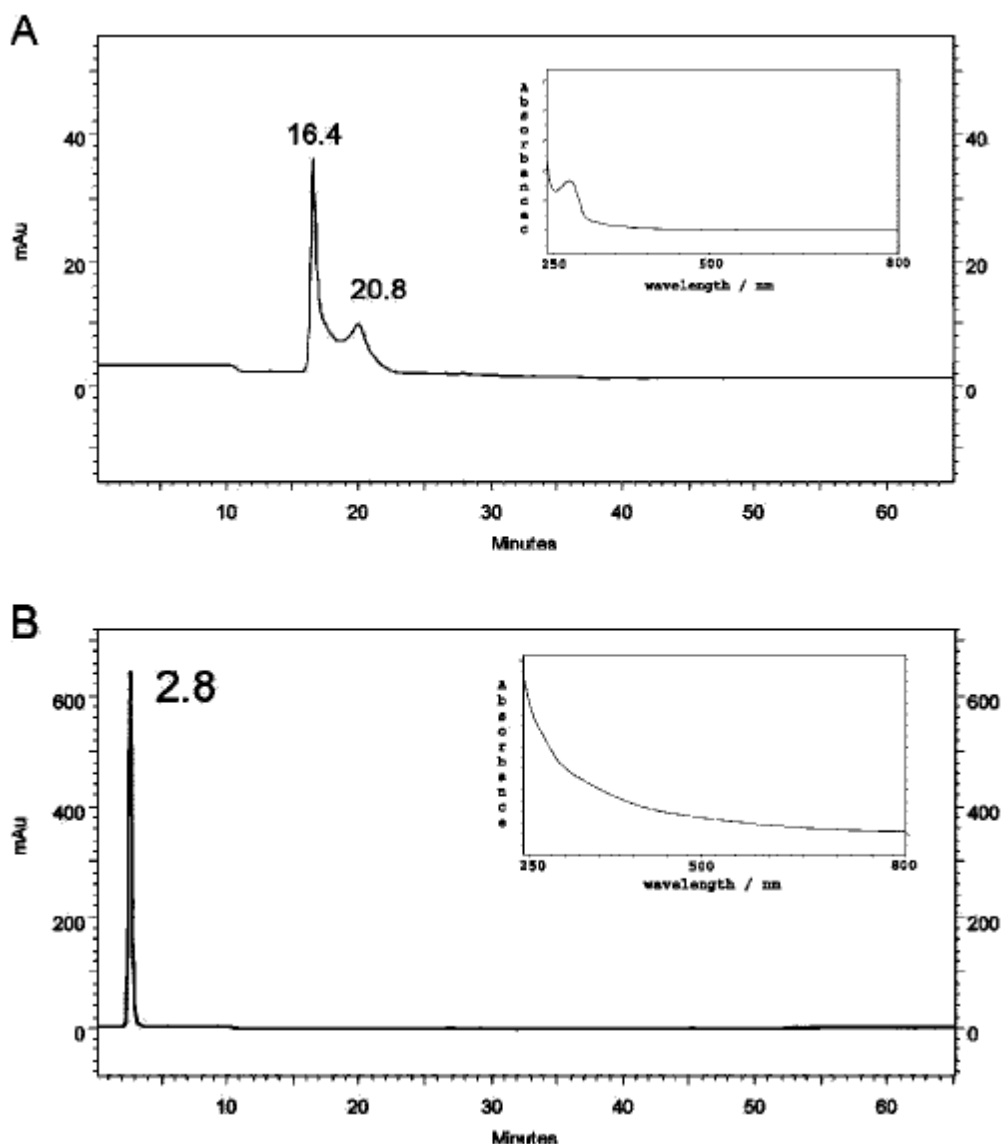
Figure 5.10 HPLC chromatograms of MspA (A) and small Au@MspA (B). Upon binding of the nanoparticles, the MspA peak shifts from 16.5/19.8 to 2.8 min (small Au@MspA) and 3.2 min (large Au and MspA). Note that the peak maxima of the small gold nanoparticles (1.8 min) and large gold nanoparticles (2.5 min) are distinctly different (not shown). The corresponding UV-vis spectra (shown as insets) confirmed the identity of the peaks. Principally, the same results are obtained when using MspA^{cys} and MspA.

Nanoparticle assembly	Binding constant (K_B) L/mol
Small Au@MspA	1.3×10^{9}
Large Au@MspA	2.22×10^{10}
Small Au@MspA^{cys}	$> 10^{12}$ (irreversible)[a]
Large Au@MspA^{cys}	1.7×10^{10}

[a] No free MspA could be detected.

Table 5.1 Binding Constants K_B (L/mol) Calculated from the HPLC Chromatograms Using Equation 5.1 and the Starting Concentrations of [MspA]^0 (1.09×10^{-9} mol/L) and Gold Nanoparticles [Au]^0: Small (3.67×10^{-8} mol/L) and Big (1.13×10^{-11} mol/L).

It is of importance for hyperthermia experiments using either gold nanoparticles or magnetic particles featuring an outer layer of gold that the binding constants of the small gold nanoparticles are very high. We have shown that these particles are able to bind within MspA and thus form 1:1 supramolecular complexes. If MspA^{cys} is used, the binding constant increases by at least 3 orders of magnitude indicating that these assemblies will be stable enough for their use within the (human) body. It is of interest as well that the binding constants between MspA and the big gold nanoparticles are distinctly higher than those of MspA and the smaller nanoparticles. We propose the possible reason for this behavior: (a) the big gold nanoparticles that are excluded from the interior of MspA can bind to the hydrophobic docking zone of MspA and (b) therefore clusters of MspA and the big gold nanoparticles are likely. However, equation 5.1 only describes 1:1 stoichiometry and we do not know the aggregation numbers of possible clusters. Therefore, the binding constants calculated for the big nanoparticles and MspA according to (5.1) are most likely high too.

Conclusions

The interactions of two gold nanoparticles of different sizes (average diameters of 3.7 ± 2.6 and 17 ± 3 nm) with the wild type of the mycobacterial porin MspA and a tailored cysteine mutant MspA Q126C by means of fluorescence/ phosphorescence spectroscopy are studied. Strong quenching of the MspA's tryptophan fluorescence is observed, indicating that the small gold nanoparticles are able to dock within the MspA pore and form supramolecular assemblies. The addition of eight cysteines within the MspA goblet by site specific mutation further increases the binding of the small gold nanoparticles within the MspA^{cys} pore. Exciting the surface plasmon resonance of the small gold nanoparticles shows energy transfer to the porin, which is absent in the case of large nanoparticles. Furthermore, the difference spectra data indicate there is an interaction between the protein and the gold nanoparticles. Contrary to the behavior of the small nanoparticles, the bigger nanoparticles cannot dock within the homopore of MspA because of size exclusion. This behavior is consistent with the observed fluorescence enhancement due to energy transfer from the surface plasmon of the bigger nanoparticles to the tryptophan residues of the MspAs.

When the nanoparticles are excited directly, the observed phosphorescence enhancement of the MspA tryptophan units is additional mechanistic proof of the formation of Au@MspA assemblies. Most interestingly, the observed fluorescence enhancement of the excited tryptophan units in the presence of the bigger, directly excited, gold nanoparticles clearly suggests that some kind of binding must take place. These results are corroborated by HPLC experiments. The binding constant of the small gold nanoparticles within MspA^{cys} exceeds 10^{12} (L/mol). This strongly suggests that Au@MspA assemblies, when designed correctly, are stable enough to be used as therapeutic agents.

Most of the data presented in this chapter have been already published in *Nano Lett.*, **2008**, 8 (4), 1229–1236.

References

1.   Pissuwan, D.; Cortie, C. H.; Valenzuela, S. M.; Cortie, M. B. *Gold Bull.* **2007**, *40*, 121–129.

2.   Qu, X.; Norbert, K.; Li, Z.; Wang, J.; Zhang, Z.; Huettmann, G. Confocal, Multiphoton, and Nonlinear Microscopic Imaging III. *Proc. SPIEsInt. Soc. Opt. Eng.* **2007**, *6630*, 66301C/1–66301C/8.

3.   Polsky, R.; Gill, R.; Kaganovsky, L.; Willner, I. *Anal. Chem.* **2006**, *78*, 2268–2271.

4.   Pavlov, V.; Xiao, Y.; Shlyahovsky, B.; Willner, I. *J. Am. Chem. Soc.* **2004**, *126*, 11768–11769.

5.   Willner, I.; Baron, R.; Willner, B. *Biosens. Bioelectron.* **2007**, *22*, 1841–1852.

6.   Wagner, E. *Expert Opin. Biol. Ther.* **2007**, *7*, 587–593.

7.   Katz, E.; Willner, I. *Angew. Chem., Int. Ed.* **2004**, *43* (45), 6042– 6108.

8.   Mukherjee, P.; Ahmad, A.; Mandal, D.; Senapati, S.; Sainkar, S. R.; Khan, M. I.; Parishcha, R.; Ajaykumar, P. V.; Alam, M.; Kumar, R.; Sastry, M. *Nano Lett.* **2001**, *1* (10), 515–519.

9.   Niemeyer, C. M. *Angew. Chem., Int. Ed.* **2001**, *40* (22), 4128–4158.

10.   Engelhardt, H.; Gerbl-Rieger, S.; Krezmar, D.; Schneider-Voss, S.; Engel, A.; Baumeister, W. *J. Struct. Biol.* **1990**, *105*, 92–102.

11.   Faller, M.; Niederweis, M.; Schulz, G. E. *Science* **2004**, *303*, 1189– 1192.

12.   Nie, S.; Xing, Y.; Kim, G. J.; Simons, J. W. *Annu. ReV. Biomed. Eng.* **2007**, *9*, 257–288.

13.   Cavaliere, R.; Ciocatto, E. C.; Giovanella, B. C.; Heidelburger, C.; Jonson, R. O.; Margottini, M.; Mondovi, B.; Moricca, B. C.; Rossi- Fanelli, A. *Cancer* **1967**, *20*, 1351–1384.

14.   Orgill, D. P.; Porter, S. A.; Taylor, H. O. *Ann. N.Y. Acad. Sci.* **2005**, *1066*, 106–118.

15.   http://info.tuwien.ac.at/iflt/safety/section1/1_1_1.htm.

16.   http://omlc.ogi.edu/spectra/aorta/index.html.

17.   Chen, S. H.; Kimura, K. *Langmuir* **1999**, *15* (4), 1075–1082.

18.   Turkevich, J.; Stevenson, P. C.; Hillier, J. *Discuss. Faraday Soc.* **1951**, (11), 55.

19.   De, G. T.; Rao, C. N. R. *J. Mater. Chem.* **2005**, *15* (8), 891–894.

20.   Rai, B.; Sathish, P.; Malhotra, C. P.; Pradip; Ayappa, K. G *Langmuir* **2004**, *20* (8), 3138–3144.

21.   Lakowicz, J. R. *Anal. Biochem.* **2001**, *298* (1), 1–24.

22.   Heinz, C.; Engelhardt, H.; Niederweis, M. *J. Biol. Chem.* **2003**, *278*, 10.

23.   Papp, S.; Vanderkooi, J. M. *Photochem. Photobiol.* **1989**, *49*, 775– 84.

24.   Stephan, J.; Stemmer, V.; Niederweis, M. Consecutive gene deletions in *Mycobacterium smegmatis* using the yeast FLP recombinase. *Gene* **2004**, *343*, 181–190.

25.   Chen, Y.; Barkley, M. D. *Biochemistry* **1998**, *37* (28), 9976–9982.

26.   Basel1, Matthew T.; Dani, Raj Kumar; Kang, Myungshim; Pavlenok, Mikhail; Chikan, Viktor; Smith, Paul E.; Niederweis, Michael; Bossmann, Stefan H. *Angew. Chem..* Submitted for publication.

27.   Shrestha, T.; Kalita, M.; Sukumaran, S.; Niederweis, M.; Bossmann, S. H. *42nd Midwest Regional Meeting of the American Chemical Society*, 2007.

28.   Gamage, P., Kalita, M.; Bossmann, S. H. To be published.

Chapter 5 - (B) Complex formation of MspA & MspAcys - magnetic Fe/Pt NPs

The increasing functionality of NPs that form complex with MspA/MspA[cys] could broaden the area of application of this complex. The complex of MspA/MspA[cys] with magnetic NPs might be another potentially important area (magnetic hyperthermia). Here preliminary data of the complex formation of MspA/MspA[cys] with magnetic Fe/Pt NPs are presented. The experimental procedures are similar to the ones described in chapter 5 (A) to produce the complex of MspA/MspA[cys] with magnetic Fe/Pt NPs with different sizes. Fe/Pt NPs are chosen for this experiment, because it is metallic and magnetic material at the same time. These NPs are attracting a lot of interest for the potential application in the field of biomedical sciences because bimetallic Fe/Pt NPs show extremely stable behavior in presence of oxygen during *in vivo* experiments.[1]

Experiment details

Chemicals

Platinum acetylacetonate, $Pt(acac)_2$, iron acetylacetonate, $Fe(acac)_2$, 1,2-hexadecanediol, octyl ether, and 10% tetramethylammonium hydroxide (TMAOH), oleic acid, oleyl amine are purchased from Sigma-Aldrich and used without purification.

NPs synthesis

Two different sizes Fe/Pt NPs are used in this experiment. Fe/Pt I NPs are smaller than Fe/Pt II NPs. Fe/Pt I is synthesized by chemical reduction method as described by Elkins *et al.*[2] Briefly, 1.5 mmol of 1,2-hexadecanediol is used to reflux 0.5 mmol of iron acetylacetonate and 0.5 mmol of platinum acetylacetonate in 30 mL of dioctyl ether in presence of 0.05 mmol of oley

lamine and 0.05 mmol of oleic acid at the boiling temperature of octyl ether for 30 minutes. Then, the solution is cooled down to room temperature. The residual NPs are subjected to successive washing/centrifuging cycles to remove excessive surfactant using ethyl alcohol. The remaining dark brown precipitate is redispersed in hexane. Thus prepared NPs are transferred into aqueous medium through phase transfer using 10% TMAOH as described by Salgueirino-Maceira *et al.*[3] Briefly, hexane dispersed NPs are redispersed in 2 mL of 10% TMAOH and 100 mL of deionized water. Sonication and shaking of the mixture transform the NPs from hexane to water. The NPs in water are centrifuged several times to eliminate the excess of surfactants, and the precipitates are redispersed in TMAOH. Thus obtained monodispersed Fe/Pt nanoparticles have average size around 3.5 nm. The representative TEM images and size distributions of both NPs are shown in Figure 5.11.
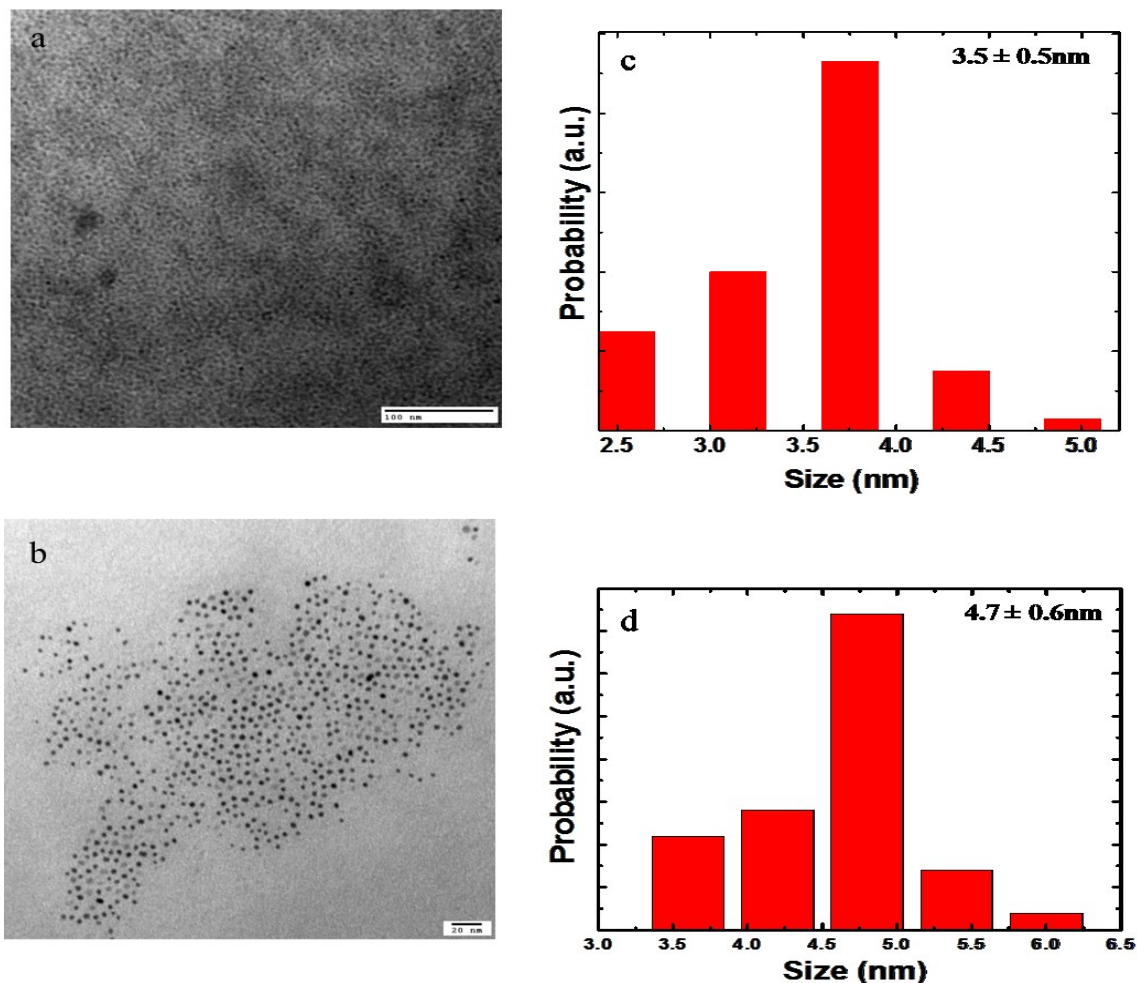
Figure 5.11 Representative TEM images of (a) Fe/Pt I & (b) Fe/Pt II NPs and (c) and (d) are their respective size distributions.

PL measurements

Tryptophan molecules are the source of fluorescence in MspA and MspA^{cys}. Every MspA molecule contains eight identical amino acid chains and each chain is composed of 184 amino acid residues with four tryptophan fluorophores at positions 21, 40, 72 and 181. There are altogether 32 tryptophan molecules in each MspA molecule.[4] Fluorescence emission spectra, quantum yields, and decay times of amino acid tryptophan has long been known to be highly sensitive of its local environment and presence of nearby quenchers.[5, 6] In this experiment,

tryptophan alone is also used with NPs to see the photoluminescence change due to the addition of magnetic NPs.

Fluorescence data are taken after the addition of every 5 µL of NPs solution to assess the change in PL due to the interactions between the fluorophore and NPs' surface. The relative change in intensity of the fluorescence is shown in Figure 5.12.
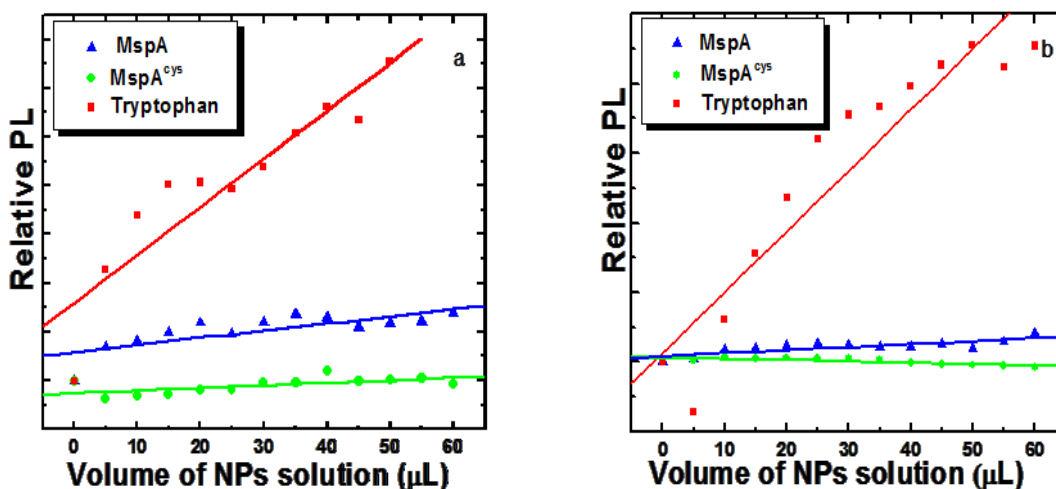
Figure 5.12 Increasing fluorescence intensity of the mixture of (a) Fe/Pt I (small) (b) Fe/Pt II (large) with MspA, MspA^{cys}, and tryptophan.

The increasing intensities of fluorescence of the mixture of NPs and MspA, MspA^{cys} are not similar with the mixture of similar size of gold NPs and MspA, MspA^{cys}. However, the size of Fe/Pt NPs is smaller than the opening pore of MspA and MspA^{cys}. This indicates that the complex formation process of MspA/MspA^{cys} with gold and magnetic Fe/Pt NPs is different. Regardless the size (larger or smaller than the opening of porin) of the magnetic NPs Fe/Pt, the interaction is always the same. Interaction of magnetic Fe/Pt NPs with MspA/MspA^{cys} is similar with that of large gold NPs. It might be because of the magnetic moment of the magnetic NPs

that forces the NPs come near to each other and make aggregates and behaves like large NPs. Our speculation is that the interaction of magnetic Fe/Pt NPs between MspA/MspA^{cys} takes place only from outside of porion. Magnetic moment of magnetic NPs brings them closer and forms large aggregates which make them unable to enter into the porin channel.

Conclusions

The interaction of magnetic Fe/Pt NPs with MspA and MspA^{cys} is studied using fluorescence spectroscopy. The experiment shows both Fe/Pt NPs could not quench the fluorescence from tryptophan of MspA and MspA^{cys}. While gold NPs are able to quench the fluorescence and form supramolecular assemblies. This result clearly indicates that the interactions of Fe/Pt and gold NPs with Mspa/MspA^{cys} are different though the sizes are comparable. The future studies need to be focused on the aggregation of NPs because magnetic moments drag the particles come closer to each other to form bigger cluster. The larger NP size prevents complex formation with MspA. In the previous chapter on the Faraday rotation of magnetic Fe_2O_3 NPs, the results indicate formation of large aggregates from single NPs in solution. It is speculated that similar thing could happen in the case of the Fe/Pt NPs. However, no aggregation data are taked for this experiment. Therefore, future experiments need to be focused on the quantifying the magnetic interactions. Controlling these interactions could produce useful inorganic/biological complexes.

References

1.   Kim, D. K.; Kan, D.; Veres, T.; Normadin, F.; Liao, J. K.; Kim, H. H.; Lee, S. H.; Zahn, M.; Muhammed, M., *J. Appl. Phys.* **2005,** *97*, 10Q918.

2.   Elkins, K. E.; Vedantam, T. S.; Liu, J. P.; Zeng, H.; Sun, S. H., *Nano Lett.* **2003,** *3* (12), 1647-1649.

3.   Salgueirino-Maceira, V.; Liz-Marzan, L. M.; Farle, M., *Langmuir* **2004,** *20* (16), 6946-6950.

4.   Dani, R.; Kang, M.; Kalita, M.; Smith, P.; Bossmann, S.; Chikan, V., *Nano Lett.* **2008,** *8* (4), 1229-1236.

5.   Vivian, J. T.; Callis, P. R., *Biophys. J.* **2001,** *80*, 2093-2109.

6.   Gryczynski; Malak, H.; Lakowicz, J. R., *Biospectroscopy* **1996,** *2* (1), 9-15.

Chapter 6 - Magnetic nanoparticles heating for magnetic hyperthermia

In general, the energy of the rapidly changing electromagnetic field can be converted into heat energy. Both, the electric field (E) and the magnetic field strength (H) are able to generate heat. The most common conversion takes place through resistive heating, capacitive heating and induction heating.[1] Resistive and capacitive heating are possible through the electric component (E) of the alternating electromagnetic field. In resistive heating, heat energy is produced when an electric current flows through a resistive material. The heat energy produced depends on the current flow and the resistance of the material and is calculated as square of current times resistance (I^2R). This is the principle of the electric heater. As the frequency of alternating electromagnetic field increases, the amount of internal atomic distortion also increases. This increasing internal atomic distortion produces a large amount of heat in the medium[1] which is known as capacitive or dielectric heating. Capacitive heating is the working principle of household microwaves. Capacitive heating takes place at higher frequencies (10 MHz). Capacitive heating is able to heat water and even insulators as well. Therefore, higher frequencies cannot be used in human being involved clinical applications since human being contain more than 75% of water. However, there is one more mechanism which can convert alternating magnetic field into heat. The mechanism is known as inductive heating which occurs at low frequencies. At low frequencies, the effect of electric component is insignificant and heating is mainly due to the magnetic component (H).[2] In inductive heating, heat is produced in a magnetic material when the material is exposed to an AC field. Current is induced in the material heated by electromagnetic induction.[1] Inductive heating can be used in the clinical applications such as magnetic hyperthermia (MHT). Tolerable limits of inductive heating of tissues limit the

safe range of magnetic field amplitude and frequency that can be employed for MHT. It has been shown that any combination of field strength (H) and frequency (f) will be biologically non-invasive when $H*f \leq 4.85 \times 10^8$ Hz-A/m.[3]

MHT is a technique where magnetic fluid is exposed to an alternating magnetic field, the magnetic particles can act as an effective source of heat[4] which could be used to destroy the cancer cells. Cell death occurs either due to the protein denaturation or the dissolution of parts of the cell membrane.[5] The fundamental basis of the magnetic hyperthermia is that cells show signs of apoptosis and necrosis when heated around 46˚C.[6] At this temperature, the function of many structural and enzymatic proteins within cells is modified, which in turn alters cell growth and differentiation and can induce apoptosis. Magnetic hyperthermia leads to more desirable apoptosis cell dying method rather than necrosis. Unfortunately, the temperature at which apoptosis of cancer cells takes place is too close to that of normal cells. Therefore, temperature control would be necessary.[7] The first experimental investigation of the magnetic hyperthermia was suggested by Gilchrist *et al.* in 1957 by heating various tissue sample using 20-100 nm of γ-Fe_2O_3 nanoparticles with 1.2 MHz magnetic fields.[8] Nowadays, magnetic hyperthermia is becoming a promising tool in treating various types of cancer. This is because tumor cells are more susceptible to heat than normal tissue cells.[9] Thermal resistance of cancer cells is lower than the normal cells because the flow of blood is insufficient in tumors and the inadequate blood flow makes tumors more acidic due to the lactic acid buildup (higher rates of metabolism) in the tumor tissues form lack of oxygen (hypoxic) while the normal cells are well oxygenated (euoxic). Acidic nature increases the temperature sensitivity of the cells and temperature will rise easily when the blood flow is insufficient and cancer cells can be eliminated selectively by raising the local temperature of the tumor sites.[10]

Heat generation using magnetic NPs

The heating effect of magnetic fluid is a result of absorbing energy from an alternating magnetic field and converting it into heat by the eddy current losses and relaxation losses.[11] Essentially the origin of heat, when magnetic particles are exposed in alternating magnetic field, depends on the size of the particles and hence their magnetic properties.[12] When the magnetic particle size is larger than 1 micron, generation of the eddy currents in the particles is responsible for heat generation. For multi-domain magnetic particles, the heating is mainly due to hysteresis loss. Larger particles have number of sub-domains with well-defined magnetization direction. When such particles are exposed into the alternating magnetic field, the domain with the magnetization direction along the magnetic field axis grows and the other ones shrink. This phenomenon is called domain wall displacement.[13] When the magnetization curves with increasing and decreasing magnetic field amplitudes do not coincide then the material is said to exhibit a hysteresis behavior and generates heat under the influence of the alternating magnetic field. The amount of heat that is generated during hysteresis loss can be calculated by determining the area of the hysteresis loop.

When the size of nanoparticles decrease to single-domain particle regime (super paramagnetic NPs), generation of heat due to hysteresis loss is not possible since there are no domain walls and the domain wall displacement is not possible. Even though, these nanoparticles can produce heat under the influence of the alternating magnetic field. The generation of heat by single-domain magnetic particles is due to the relaxation loss. There are two distinct relaxation loss mechanisms by which the magnetization of magnetic nanoparaticles can relax back to their equilibrium position after the applied magnetic field is removed. The first relaxation mechanism is the Néel relaxation where rotation of magnetic moment within the particles takes place to

reverse magnetization direction. This process needs to overcome an energy barrier, which is for uniaxial anisotropy, is given by $E = KV$, where K is the anisotropy constant of the material and V is the volume of the particles. An external alternating magnetic field supplies energy and assist magnetic moments to overcome the energy barrier. This energy is dissipated when the particle moment relaxes to its equilibrium orientation. The relationship between the characteristic time of thermal fluctuation of the magnetic moment of a single-domain particle with uniaxial anisotropy is obtained by Néel relaxation time, τ_N, as[14]

$$\tau_N = \tau_0 \, e^{\left(\frac{\Delta E}{k_B T}\right)} \hspace{5cm} 6.1$$

where k_B is the Boltzmann constant, the pre-exponential factor, τ_0, is an expression of the anisotropy energy and depends on several parameters, including temperature, gyromagnetic ratio, saturation magnetization, anisotropy constants, the height of barrier, etc. However, for the sake of simplicity, the value of τ_0 is often considered to be a constant [15] in the range of 10^{-9} to 10^{-13}s, and T is the temperature. In summary, Néel relaxation time represents the time required to achieve zero magnetization after the external magnetic field is removed.

The second relaxation mechanism is the Brownian relaxation. If particles move freely within the suspension, the entire particle can rotate to align along the external magnetic field. This mechanism generates heat due to the viscous friction between the rotating particle and the surrounding medium. The Brownian relaxation time, is given by[16]

$$\tau_B = \frac{3\eta V_H}{k_B T} \hspace{5cm} 6.2$$

where η is the dynamic viscosity of the carrier liquid, V_H is the hydrodynamic volume of the particle. Hydrodynamic volume (particle + ligand layer) characterizes how a particle moves through the fluid in which it is suspended and may be different than the magnetic volume due to agglomeration, coating or interactions between the fluid and the nanoparticle surface.

The two relaxation mechanism is shown in the following Figure 6.1.

Figure 6.1 Schematic depiction of Néel and Brownian relaxation.

In summary, out of these two mechanisms, the faster relaxation mechanism is the dominant in the heat dissipation process. The Néel relaxation depends exponentially on magnetic anisotropy and particle volume. The Brownian relaxation depends linearly with the particle volume and viscosity of carrier liquid. Due to different size dependence of Néel and Brownian relaxation, there is a boundary for these two relaxations where crossover of relaxation takes place. The crossover between Néel and Brownian relaxation takes place when $\tau_N = \tau_B$. The dominant relaxation times of maghemite/water system are shown in Figure 6.2. In general, Néel relaxation prevails at higher frequency combined with smaller particle size and vice versa for Brownian relaxation.[17]
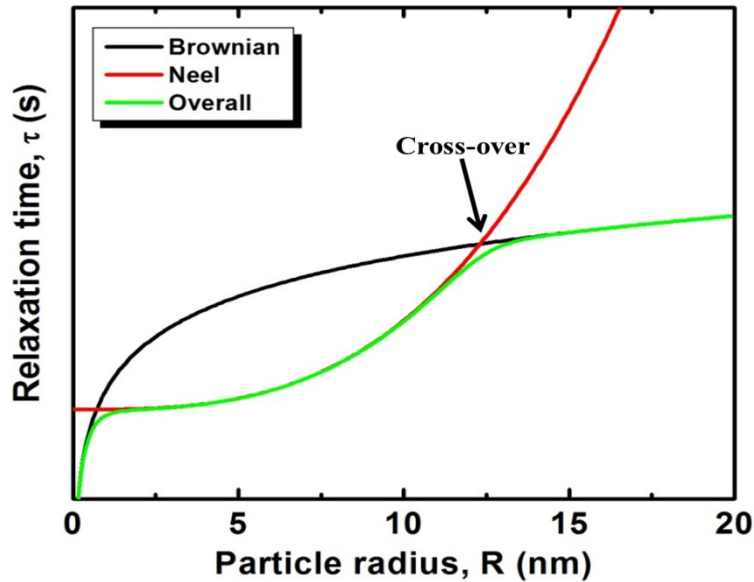
Figure 6.2 Relaxation times of maghemite/water system.

The boundary frequency (f_c) and the corresponding particle diameter (D_c), of some of the selected ferrofluids are given in the following table 6.1.[17]

Ferrofluid	D_c nm	f_c kHz
Maghemite/water	25	8
Maghemite/ester oil	24	0.1
Ba-hexaferrite/water	11	50
Co-ferrite/water	7	10000
Co-ferrite/glycerin	9	0.1
Co, hexag./water	6	2500

Table 6.1 Estimated separating Néel and Brownian relaxation regime.[17]

In most of the case, both relaxation mechanisms work together and the effective relaxation time is given by

$$\frac{1}{\tau} = \frac{1}{\tau_N} + \frac{1}{\tau_B}$$ 6.3

126

Mechanism of heat generation

Rosensweig[18] developed the analytical relationships of power dissipation from the ferrofluid in alternating magnetic field. Briefly, magnetization of ferrofluid cannot follow the applied time varying magnetic field. The phase lag between the applied magnetic field and the magnetization of the ferrofluid results in conversion of magnetic work into internal energy. It is convenient to express the magnetization in terms of the complex ferrofluid susceptibility as $\chi = \chi' - i\chi''$, where χ' is the in-phase component and χ'' is the out-of-phase component of susceptibility. The change in internal energy is given by

$$\Delta U = 2\mu_0 H_0^2 \chi'' \int_0^{2\pi/\omega} \sin^2 \omega t \, dT \qquad 6.4$$

Here, only the out-of-phase component, χ'', survives, hence it is also known as loss component of susceptibility. Integrating and multiplying the result by cyclic frequency ($f = \omega/2\pi$) gives the mean volumetric power dissipation (loss power density, Wm^{-3}):

$$P = f\Delta U = \mu_0 \pi \chi'' f H_0^2 \qquad 6.5$$

The susceptibility components are given by

$$\chi' = \frac{1}{1 + (\omega\tau)^2} \chi_0 \qquad 6.6$$

$$\chi'' = \frac{\omega\tau}{1 + (\omega\tau)^2} \chi_0 \qquad 6.7$$

Then the equations (6.5) and (6.7) give the power dissipation for a monodispersed ferrofluid which is expressed as

$$P = \pi \mu_0 \chi_0 H_0^2 f \frac{2\pi f\tau}{1 + (2\pi f\tau)^2} \qquad 6.8$$

For polydispersed ferrofluid, the volumetric heat dissipation rate is given by

$$P = \int_0^\infty P \mathrm{g}(R) dR \qquad 6.10$$

where g(R) is the log normal size distribution, which is given by

$$g(R) = \frac{1}{\sqrt{2\pi}\sigma R} exp\left[\frac{-(\ln R/R_0)^2}{2\sigma^2}\right]$$

6.11

where $\ln R_0$ is the median radius and σ is the standard deviation of $\ln R$.

The loss power density P (Wm^{-3}) is related with the specific loss power SLP (Wg^{-1}) by the mean

mass density of the particles.[19] The maximum loss power could be reached with small particles

and high frequencies. Here, a typical example for γ-Fe$_2$O$_3$ nanoparticle is shown in the following

Figure 6.3.
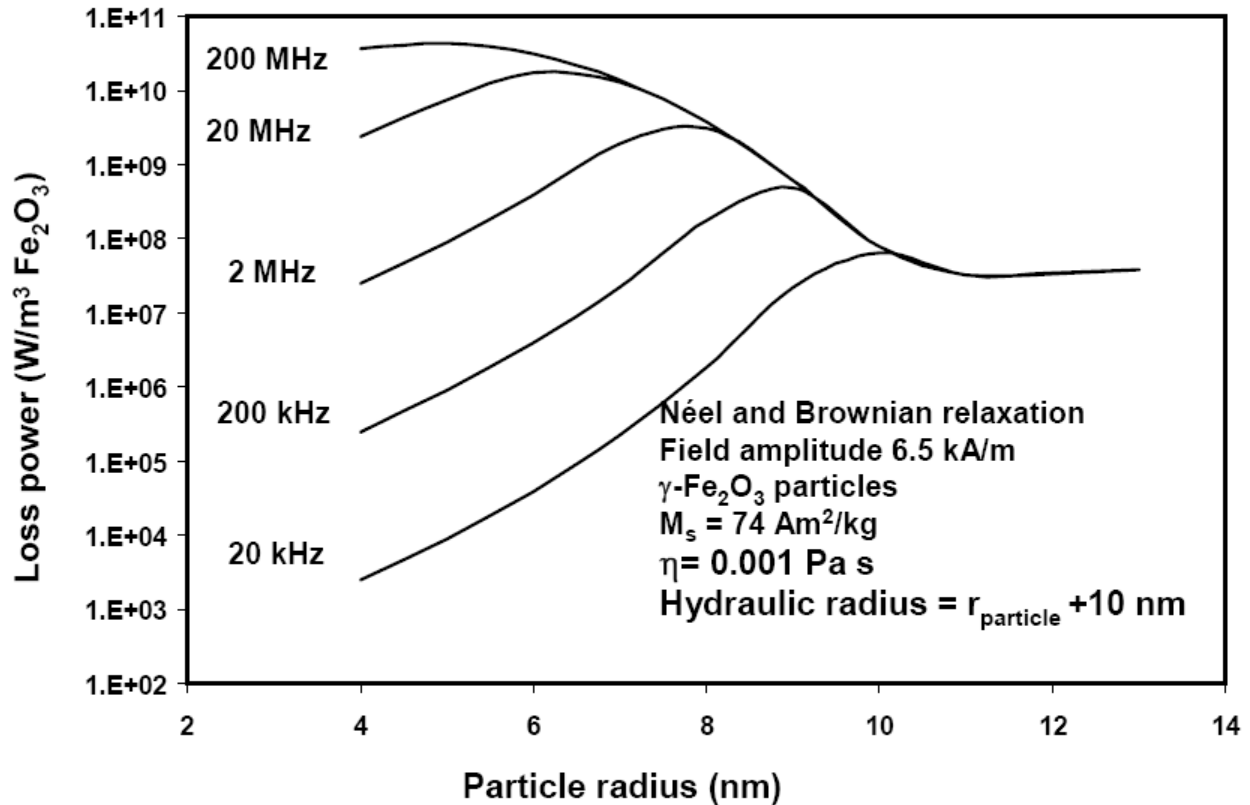
Figure 6.3 Loss power of γ-Fe$_2$O$_3$ with its size and frequency of applied alternating magnetic field.[20]

Independent of the heating mechanism, the heating efficiency of the particles is

quantified in terms of the power of heating of a magnetic material per gram (specific loss power,

SLP), which is also called the specific absorption rate (SAR).[21] SAR is defined by the following expression

$$SAR = C\frac{dT}{dt}$$ 6.12

where C is the specific heat capacity of the system ($Jg^{-1}K^{-1}$), dT is the change in temperature and dt is the change in time.

Experimental measurement of SAR

In the measurement of SAR of magnetic NPs, four different magnetic NPs are used. Sizes of all of them fall in the superparmagnetic region. Superparamgnetic NPs comparatively generate more heat in alternating magnetic field than the equal mass of other magnetic NPs. Among four types of NPs, two are Fe/Pt (Fe/Pt I and Fe/Pt II), and remaining are CoAu, and FeAu. Fe/Pt I is synthesized by chemical reduction method as described by Elkins *et al.*[22] Briefly, 1.5 mmol of 1,2-hexadecanediol is used to reflux 0.5 mmol of iron acetylacetonate and 0.5 mmol of platinum acetylacetonate in 30 mL of dioctyl ether in presence of 0.05 mmol of oleylamine and 0.05 mmol of oleic acid at the boiling temperature of octyl ether for 30 minutes. Then the solution is cooled down to room temperature. The residual NPs are subjected to successive washing/centrifuging cycles to remove excessive surfactant using ethyl alcohol. The remaining dark brown precipitate is redispersed in hexane. Thus prepared NPs are transferred into aqueous medium through phase transfer using 10% TMAOH as described by Salgueirino-Maceira *et al.*[23] Briefly, hexane dispersed NPs are redispersed in 2 mL of 10% TMAOH and 100 mL of deionized water. Sonication and shaking of the mixture transform the NPs from hexane to water. The NPs in water are centrifuged several times to eliminate the excess of surfactants, and the precipitates are

redispersed in TMAOH. Thus obtained monodispersed Fe/Pt nanoparticles have average size around 3.5 nm.

An induction heater (shown in Figure 6.4), manufactured by Superior Induction Company, CA, is used to determine the SAR value of NPs. The heater contains a copper coil which has one inch diameter with four turns and is continuously cooled with cold water. The heater operates with 5 kA/m field amplitude at 366 kHz frequency.

Figure 6.4 Induction heater (left) and fiber optic temperature probe (right) for magnetic hyperthermia experiment.

2 mL of every NPs colloid is placed in a glass vial and put inside the coil of induction heater using Teflon holder. A Teflon holder act as insulator and it prevents the residual heating of the sample from the coil. The temperature change of the colloidal solution is measured using a fiber optic probe (shown in Figure 6.4), manufactured by Neoptix, Canada and recorded in a computer. The rise of temperature of sample solutions as a function of time is shown in Figure 6.5.
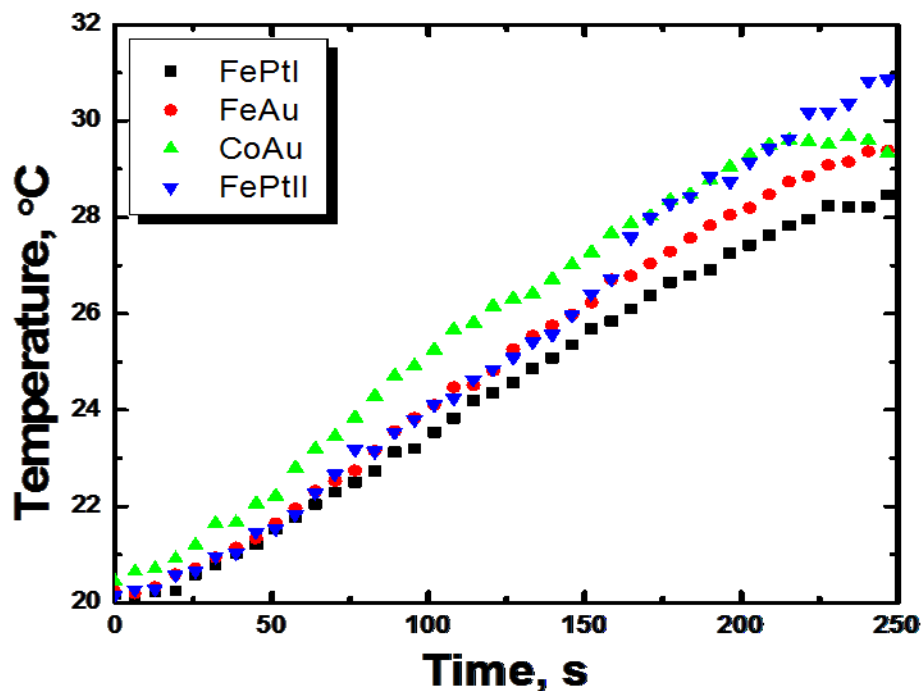
Figure 6.5 Change in temperatures of magnetic NP colloids with time.

Clear difference can be seen the heating effect of different magnetic NPs. In order to reduce the errors due to the conduction of heat to the environment, the initial slope of the time dependent temperature curve ($\Delta T/\Delta t$) is taken for the calculation of SAR. The calculated values of SAR for different NPs at 5 kA/m and 366 kHz of applied alternating magnetic field are tabulated in table 6.2.

NPs	Size nm	Concentration g/mL	$\Delta T/\Delta t$	SAR W/g
FePt I	3.5	0.0093	0.018	16.18
FePt II	4.5	0.0045	0.013	24.15
FeAu	3.5	0.0036	0.015	35.5
CoAu	3.5	0.0050	0.0126	21.2

Table 6.2 Experimentally determined SAR for different magnetic NPs.

SAR depends on various factors for example; size, size distribution, shape, bulk and surface chemical compositions, frequency and amplitude of the magnetic field, viscosity of the carried medium.[12] In our experiment, NPs sizes are very similar. The frequency and amplitude of the applied magnetic field and the viscosity of carrier liquid are same for all experiments. Note that SAR (W/g) is independent of the concentration of the sample. It means the difference in SAR is because of the shape and size distribution along with the bulk and surface chemical compositions.

Viscosity dependence of SAR

For the viscosity dependence of SAR values of magnetic nanoparticles, commercially available Fe_3O_4 (EMG 707) nanoparticles colloid is used which is well characterized with 10 nm average diameter. To manipulate the viscosity of the carrier liquid, different volume of water and ethylene glycol are mixed such that the viscosity dependence of SAR with the contribution of Brownian relaxation on heat generation of the system can be calculated. Four solutions with different viscosities are prepared and tested the rise in temperature with respect to time under the same conditions. The temperature change with respect to time for all colloids with different viscosities is represented in the following Figure 6.6.
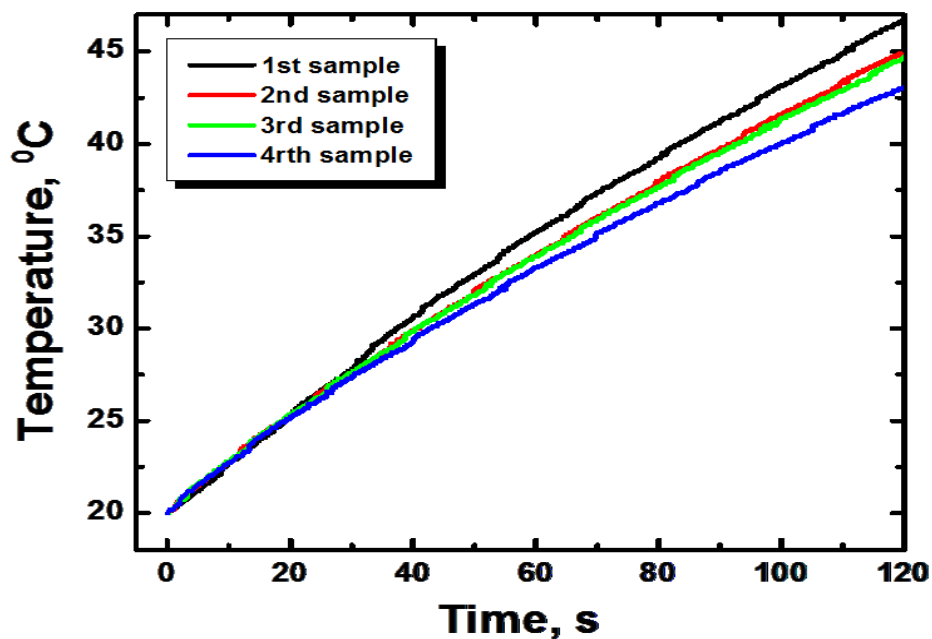
Figure 6.6 Change in temperature with respect to time for magnetic colloids of EMG 707 in corresponding viscous medium.

Depending on above heating curve, SAR of all colloids are calculated. The calculated SAR with their corresponding viscosity and compositions of all the sample solutions are given in table 6.3.

Sample	Water mL	Ethylene glycol mL	EMG 707 μL	Sample viscosity cP at 20°C	SAR W/g
1st	2	0	40	1.002	328.95
2nd	1.5	0.5	40	2.481	276.73
3rd	1	1.0	40	4.688	243.57
4rth	0.5	1.5	40	8.43	205.74

Table 6.3 Composition of the samples and calculated SAR for EMG 707 Fe₃O₄ NPs with corresponding viscosity.

The variation of the SAR with viscosity is plotted in the following Figure 6.7.
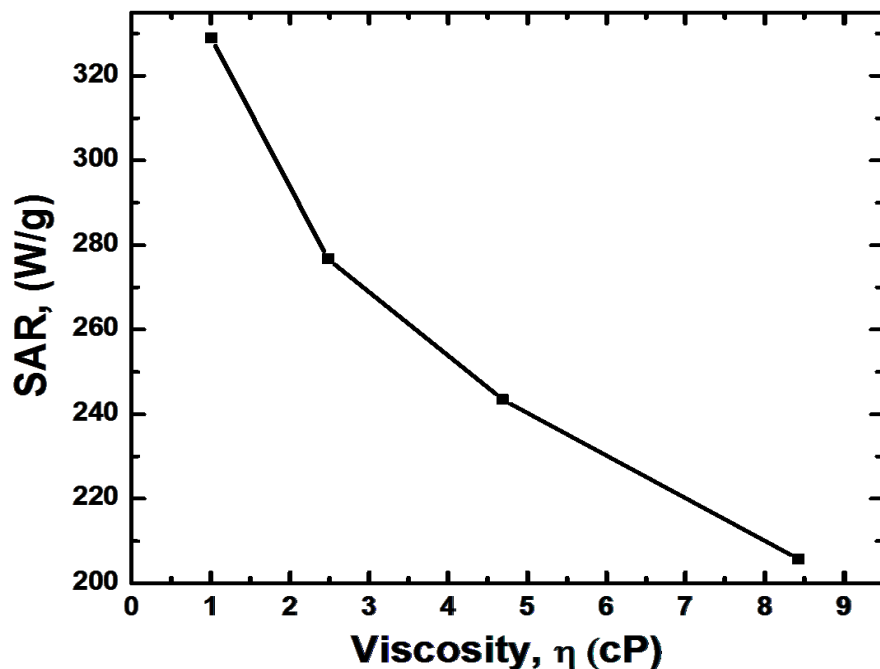
Figure 6.7 Variation of SAR of Fe$_3$O$_4$ EMG 707 NPs with viscosity.

As viscosity increases the SAR decreases which is, of course, reasonable. It is because as viscosity increases, the contribution of Brownian relaxation to the SAR decreases since higher viscosity hinders the physical rotation of the magnetic particles in the carrier liquid. This effect reflects into low SAR for the same NPs in highly viscous liquid. In this sample, the Brownian contribution for SAR is approximately 30% in water.

Conclusions

Heating efficiency of different NPs is investigated. The experimentally determined SAR of around 4 nm particles indicates that more NPs need to be used to kill the cancer cell because the reasonable assumption to destroy one cm^3 of tumor tissue using magnetic hyperthermia is 5-10

mg.[24] Lee *et al.*[25] have recently shown 100 to 450 W/g for uniformly dispersed Fe_3O_4 NPs of 9, 12 and 15 nm diameter which is increased to 1,000 to 4,000 W/g after coating them using $CoFe_2O_4$ at 37.3 kA/m and 500 kHz.

Viscosity also significantly affects the heating capacity of NPs. SAR decreases approximately by 30% in water when Brownian relaxation is hindered with the application of more viscous liquids. However, delivery of NPs to the targeted area of the body, toxicity, controlling the temperature at specific range and dose of NPs are other critically important factors that need to be studied before using the NPs for biomedical applications. Next research in this field should be focused on these topics.

References

1.   Patrick, D. R.; Fardo, S. W., *Electrical Distribution Systems*. The Fairmont Press: 2009.

2.   Nikiforov, V. N., *Russian Physics Journal* **2007,** *50* (9), 913-924.

3.   Ondeck, C. L.; Habib, A. H.; Ohodnicki, P.; Miller, K.; Sawyer, C. A., *J. Appl. Phys.* **2009,** *105* (7), 07B324.

4.   Jordan, A.; Wust, P.; Scholz, R.; Tesche, B.; Fahling, H., *International journal of hyperthermia* **1996,** *12* (6), 705-722.

5.   Bossmann, S. H., Nanoparticles for hyperthermia treatment of cancer. In *Fabrication and Bio-Application of Functionalized Nanomaterials*, Wang, X., Ed. 2009.

6.   Tran, N.; Webster, T., *J. Mater. Chem.* **2010,** *20* (40), 8760-8767.

7.   Mornet, S.; Vasseur, S.; Grasset, F.; Duguet, E., *J. Mater. Chem.* **2004,** *14* (14), 2161-2175.

8.   Gilchrist, R. K.; Medal, R.; Shorey, W. D.; Hanselman, R. C.; Parrott, J. C., *Annals of surgery* **1957,** *146* (4), 596-606.

9.   Nedelcu, G., *Digest Journal of Nanomaterials and Biostructures* **2008,** *3* (3), 103-107.

10.   Maenosono, S.; Saita, S., *IEEE Trans. Magn.* **2006,** *42* (6), 1638-1642.

11.   Bekovic, M.; Hamler, A., *IEEE Trans. Magn.* **2010,** *46* (2), 552-555.

12.   Duguet, E.; Vasseur, S.; Mornet, S.; Devoisselle, J.-M., *Nanomedicine* **2006,** *1* (2), 157-168.

13.   Mornet, S.; Vasseur, S.; Grasset, F.; Veverka, P.; Goglio, G., *Prog. Solid State Chem.* **2006,** *34* (2-4), 237-247.

14.   Laurent, S.; Dutz, S.; Haefeli, U.; Mahmoudi, M., *Adv. Colloid Interface Sci.* **2011,** *166* (1-2), 8-23.

15.   LesliePelecky, D. L.; Rieke, R. D., *Chem. Mater.* **1996,** *8* (8), 1770-1783.

16.   Leslie-Pelecky, D. L.; Labhasetwar, v.; Kraus, R. H., Nanobiomagnetics. In *Advanced Magnetic Nanostructures*, Sellmyer, D. J.; Skomski, R., Eds. Springer: New York, 2006.

17.   Hergt, R.; Dutz, S.; Zeisberger, M., *Nanotechnology* **2009,** *21* (1), 015706.

18.   Rosensweig, R. E., *J. Magn. Magn. Mater.* **2002,** *252* (1-3), 370-374.

19.   Hergt, R.; Dutz, S.; Mueller, R.; Zeisberger, M., *Journal of physics. Condensed matter* **2006,** *18* (38), S2919-S2934.

20.   Hofmann-Amtenbrink, M.; Rechberg, B. V., Superparamagnetic Nanoparticles for Biomedical Applications. In *Nanostructured for Biomedical Applications*, Tan, M. C., Ed. Transword Research Network: Kerala, India, 2009.

21.   Fortin, J.-P.; Wilhelm, C.; Servais, J.; Menager, C.; Bacri, J.-C., *J. Am. Chem. Soc.* **2007,** *129* (9), 2628-2635.

22.   Elkins, K. E.; Vedantam, T. S.; Liu, J. P.; Zeng, H.; Sun, S. H., *Nano Lett.* **2003,** *3* (12), 1647-1649.

23.   Salgueirino-Maceira, V.; Liz-Marzan, L. M.; Farle, M., *Langmuir* **2004,** *20* (16), 6946-6950.

24.   Pankhurst, Q. A.; Connolly, J.; Jones, S. K.; Dobson, J., *Journal of physics. D, Applied physics* **2003,** *36* (13), R167-R181.

25.   Lee, J. H.; Jang, J.; Choi, J.; Moon, S. H.; Noh, S.; Kim, J.; Kim, J.; Kim, I.; Park, K. I.; Cheon, J., *Nat. Nanotechnol.* **2011,** *6*, 418-422.

Chapter 7 - Magnetoliposomes for magnetic field triggered controlled drug release

The first liposome was discovered about 45 years ago by Bangham and coworkers.[1] Liposomes are formed when phospholipids are hydrated or exposed to an aqueous environment. Liposomes are micro-particulate lipoidal vesicles that consist of a ~ 5 nm thick lipid bilayer shell surrounding an aqueous core exhibiting several important biological properties which may be useful in various applications. Liposomes can be made entirely from naturally occurring substances and are therefore nontoxic, biodegradable and non-immunogenic. Liposomes structure, chemical composition and colloidal size are easily controllable during their preparation. The properties of liposomes offer very useful model systems for many fundamental studies including topology, membrane biophysics, photophysics and photochemistry, colloidal interactions, cell function, signal transduction and in many industrial applications include drug delivery, diagnosis etc.[2]

Liposomes can be classified on the basis of number of lamellae and size. Unilamellar vesicles (ULV) comprise one lipid bilayer with diameter 50-250 nm. They contain a large aqueous core and are preferentially used to encapsulate water soluble drugs.[3] Multilamellar vesicles (MLV) comprise several concentric lipid bilayers with diameter 1-5 μm. ULV are homogeneous in size, and thermodynamically unstable with relatively longer circulation half-life. MLV are simple to prepare, mechanically stable with relatively shorter circulation half-time. The fast removal (short circulation half-life) of the liposomes by the macrophages and monocytes of the reticuloendothelial system (RES) can be prevented by attaching a polyethylene glycol (PEG) to the outside of the liposomes. PEG provides a dynamic cloud of hydrophilic and neutral chains at the particle surface which repel plasma protein and makes the particle invisible

to RES.[4] PEG coated liposomes are invisible to RES, hence PEG coated liposomes are also known as stealth liposomes.

Development of nanotechnology has provided a number of drug delivery and diagnosis systems. Among the different systems available, liposomes have attracted greater attention mainly due to their biocompatibility because liposomes composed of natural lipids which are biodegradable, biologically inert, weakly immunogenic, produce no antigenic or pyrogenic reactions, and possess limited intrinsic toxicity.[5, 6] Therefore, drugs encapsulated in liposomes are expected to be transported without rapid degradation with minimum side-effects. Furthermore, the vesicular structure of liposomes can include a wide range of substances, either hydrophilic within the internal aqueous compartment or hydrophobic inside the lipid bilayer shell[7] as shown in Figure 7.1 and the surface properties of liposomes can be modified comparatively easier than other drug carrier such as NPs.[8] Applications of liposomes depend and are based on physic-chemical and colloidal characteristics such as composition, size, loading efficiency of the lipids and the stability of the carrier , as well as their biological interactions with the cells.[9]
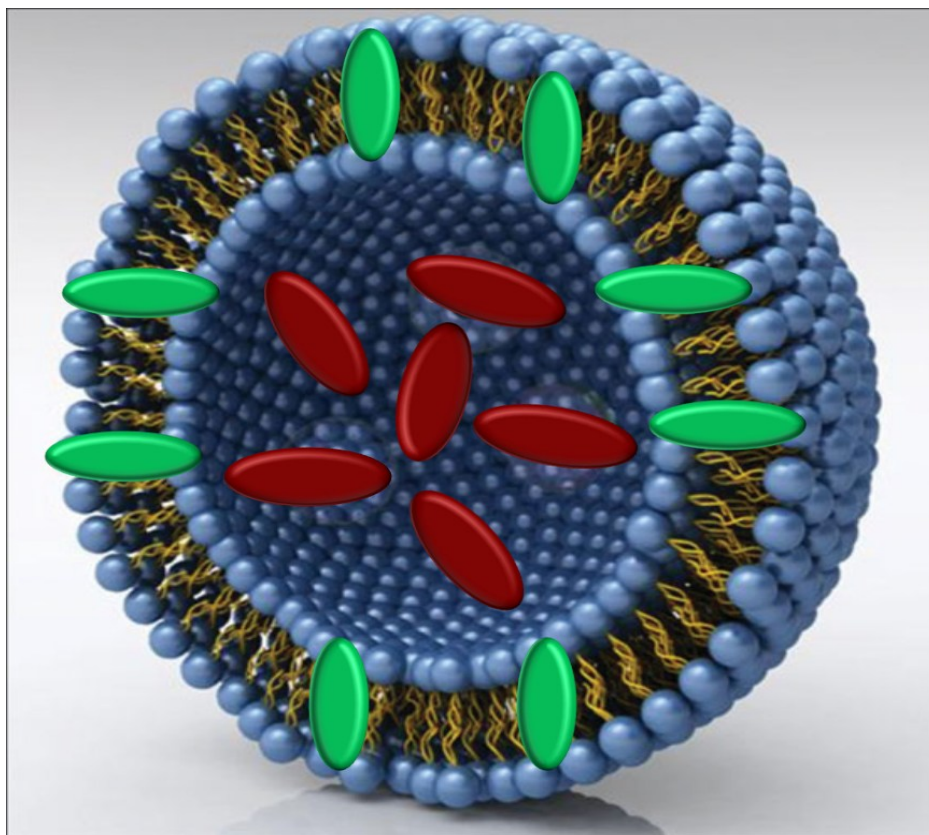
Figure 7.1 Hydrophobic compounds (green) insert between the phospholipids forming the bilayers of the liposome while water-soluble compounds (dark red) are entrapped in the aqueous space between the bilayers (modified from[10]).

On the other hand, superparmagnetic NPs are being used in various biomedical applications.[11] The flow of superparamagnetic NPs in blood vessel can be easily manipulated via external magnetic field due to the high degree of magnetic susceptibility in the presence of external magnetic field below Curie temperature.[12] Magnetic NPs can be efficiently encapsulated with liposomes and used for targeting drugs to a specific location using an external magnetic field gradient. The size of the magnetic NPs is also important, because size of NPs determines the relative contribution of the relaxation process whether Brownian or Néel. The total relaxation time is given by the equation

$$\frac{1}{\tau} = \frac{1}{\tau_N} + \frac{1}{\tau_B}$$

7.1

where τ_N is the Néel relaxation time and τ_B is the Brownian relaxation time. An estimated calculation of the total relaxation time for superparamagnetic NPs is shown in Figure 7.2. Note that the plateau where the relaxation is dominated by Brownian relaxation and is viscosity dependent.
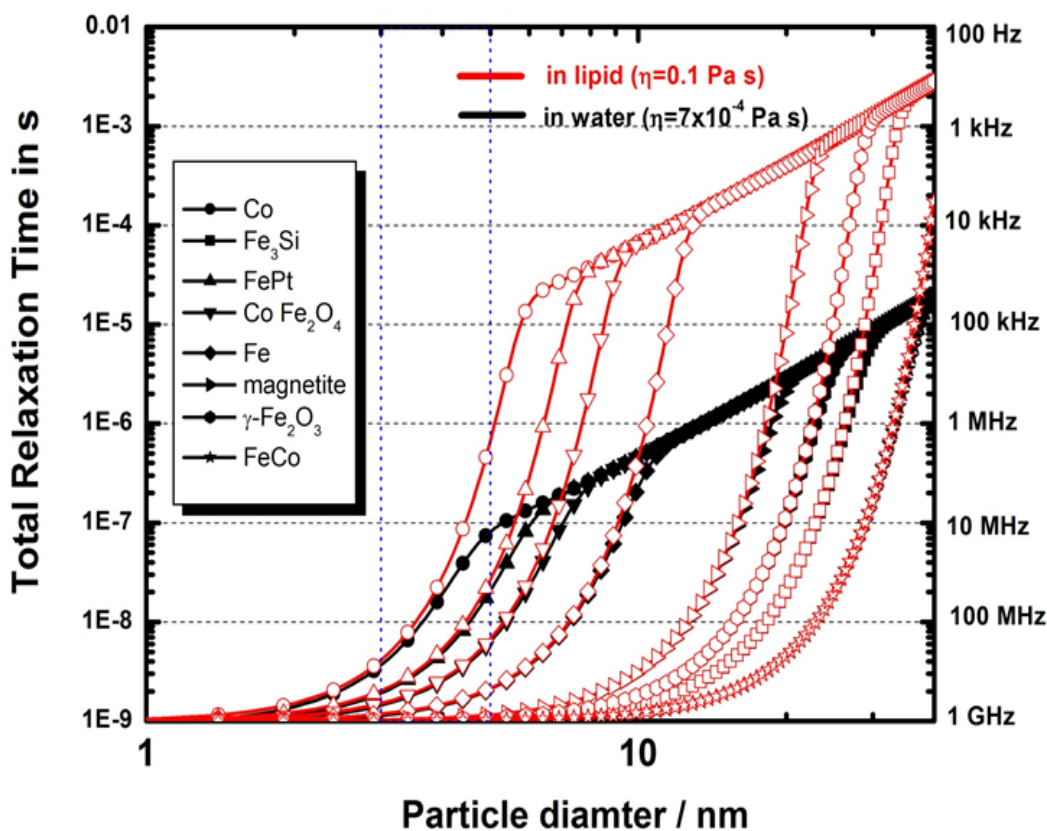
Figure 7.2 Calculation of total relaxation time of spherical magnetic NPs in water and in lipid bilayer.

The magnetic NPs encapsulated liposomes are called magnetoliposomes (MLs). The presence of magnetic NPs in aqueous pool or in the lipid bilayer of liposome enhances the drug leakage by applying the magnetic field[13] since pulsed magnetic field forces the NPs to mechanically oscillate around their equilibrium position. Superparamagnetic NP with dominated

Brownian relaxation is desirable where the rotation of the whole particle takes place and this rotation could facilitate more efficient release than release triggered by Néel relaxation. A number of investigations has been reported on exploiting superparamagnetic NPs in targeted and controlled release of drugs.[14, 15] Most of the drug delivery studies are done in presence of alternating magnetic field.[16-18] Nappini *et al.* have shown 20 to 80 percentage release efficiency for bare cobalt ferrite NPs using low frequency (0.2 kHz, 2.5 kHz, and 5.2 kHz) alternating magnetic field with different exposure times (10, 20, 50 minutes).[19] The same group in another study under similar conditions showed better loading efficiency with citrated coated cobalt ferrite NPs.[16] Babincová *et al.* have shown around 60% release of an anticancer drug (doxorubicin) with γ-Fe_2O_3 NPs using an alternating magnetic field with frequency of 3.5 MHz and 1.5 mT of magnetic field.[18] Thermally sensitive drug cannot be used in alternating magnetic field. The use of alternating magnetic field may generate the undesirable side-effect in biological systems through so-called magnetic hyperthermia effect. This effect could be minimized by using pulsed magnetic field where short pulses of magnetic field are used and minimize the undesirable side-effects. No drug release has been reported using pulsed magnetic field.

In this study, our aim is to assess the drug release from MLs under the influence of the pulsed magnetic field, to investigate the drug release from MLs as a function of number of pulses and discharge potential of pulsed magnetic field. The ultimate goal of the research is to develop an instantaneous delivery system for thermal sensitive drugs with 100% efficiency with longer circulation-half-time using PEG coating onto the surface of liposome. It is also possible to develop Magnetic Resonance Imaging (MRI) contrast agent using MLs[20] since currently used Gd^{3+} containing contrast agent is associated with high toxicity.

Experimental details

Materials

Chemicals used in synthesis of NPs ($FeCl_3.6H_2O$, 2-pyrrolidone, methanol, diethyl ether and acetone) are purchased from Sigma-Aldrich. Two types of phospholipids, 1,2-dipalmitoyl-*sn*-glycero-3-phosphocholine (DPPC), 1,2-distearoyl-*sn*-glycero-3-phosphocholine (DSPC) are used in the synthesis of liposomes. Both phospholipids are purchased from Avanti Polar Lipids. Sodium Hydroxide (NaOH), Sephadex G-50, Chloroform, Cholesterol, and 5(6)-Carboxyfluorescein (CF) dye, Triton X-100 used in liposome synthesis are purchased from Sigma-Aldrich. Phosphate buffered saline (PBS) buffer is prepared in the lab following the standard protocol.

Nanoparticle synthesis

Fe_3O_4 NPs are synthesized according to the procedure described by Zhen Li *et al.*[21] Briefly, oxygen of mixture of 10 mmol $FeCl_3.6H_2O$ and 100 mL of 2-pyrrolidone is removed by purging nitrogen gas into the mixture. The mixture is then reflux at the boiling point of 2-pyrrolidone. Then the solution is cooled to room temperature and 1:3 volume ratio of methanol/diethyl ether is added to precipitate the NPs. The black precipitate is washed with acetone several times and dried the sample for characterization. The size of the NPs depends on the reflux time. Thus obtained NPs are water soluble. For our experiment, 5 hours of reflux time is used and the estimated average size of the NPs is 15 nm.

Liposome synthesis and drug/NPs loading

There are several possible liposome synthesis methods. Some of them are:[22] (i) ultrasound treatment, which produces small sized liposomes ($\approx$ 200 nm), (ii) extrusion of hydrated lipid film method, which also produces small liposomes (less than 5 µm, depending on the pore size of

filter), (iii) electroformation method which uses an AC field between two conductive electrodes and the size of liposomes depends on the amplitude and frequency of the applied field.

Extrusion of hydrated lipid films is a common method for liposome synthesis. Different types of extrusion devices with different extrusion parameters including filter pore sizes, number of passages and use of freeze and thaw cycles could be varied.[23] Maintaining phase transition temperature (t_c) is critical during the synthesis of liposome because lipids have a characteristic t_c which determines the characteristic phase transition of lipids. The lipids are a rigid (solid), well-ordered arrangement below the t_c and in a liquid-crystalline phase above the t_c. The fluidity of liposome bilayer can be altered by using phospholipids with different t_c which in turn can vary from -20 to 90˚C depending upon the length and nature (saturated or unsaturated) of the fatty acid chains.[24] Presence of high t_c (>37˚C) lipids makes the liposome bilayer membrane less fluid at the physiological temperature and less leaky. The liposomes composed of low t_c (<37˚C) lipids are susceptible to leakage of drugs encapsulated in aqueous phase at physiological temperature. Having low t_c is advantageous for liposomes as drug carrier system due to the fact that bioactive drugs which are encapsulated in liposomes with high phase transition temperature are generally released slower than those encapsulated in liposomes with lower phase transition temperature.[23]

The general liposome synthesis method involves the preparation of the lipid for hydration, hydration with agitation, and sizing to a homogeneous distribution of vesicles.[25] For our experiment, liposomes are produced by the thin-film hydration method coupled with sequential extrusion method which is adopted from the Ph.D. thesis of Matthew T. Basel.[26] Briefly, 88:1:10 molar ratio of 1,2-dipalmitoyl-*sn*-glycero-3-phosphocholine (DPPC), 1,2-distearoyl-*sn*-glycero-3-phosphocholine (DSPC) and cholesterol, respectively, are mixed for total lipid 10 mg in a round-bottom flask. To assure a homogeneous mixture of lipids, the lipids must

be dissolved in an organic solvent. The organic solvent is either chloroform or chloroform: methanol mixture. The 88:1:10 molar ratio mixtures are thoroughly mixed and the solvent is removed by heating in water bath to yield a lipid film. Further, to remove organic solvent completely, the thin film containing round-bottom flask is placed in a vacuum for one hour.

The next step is the hydration of lipid film. Hydration of the thin-film lipid is carried out simply by adding and agitating an aqueous medium into the thin-film containing round-bottom flask. In this step, the residue is hydrolyzed using 125 µL of 1XPBS, 838 µL of water, 37 µL of 3M NaOH and 25 mg of 5(6)-Carboxyfluorescein (CF), and definite amount of NPs solution (water soluble) to incorporate NPs into the liposome. If NPs are insoluble in water, the NPs should mix with lipid before making thin film of lipid. As a control liposome, no NPs solution is used, but all other steps during preparation remain the same. Here, CF molecules act as a model drug molecules and release of this molecule is measured to calculate the percentage release of the drug. The temperature of the hydrating medium should be above the transition temperature (t_c) of the lipid with the highest t_c before adding to the dry lipid.[25] The mixture is hydrate for an hour with vigorous shaking, mixing, or stirring. The product of hydration is multilamellar lipids.

After the hydration step, the next step is freeze and thaw process. The freeze and thaw process prevents the membranes from fouling and improves the homogeneity of the size distribution of the final suspension. In this process, the temperature of the hydrated mixture is decreased to -80˚C and then increased to 50˚C ten times for five minutes each time. End the solution at 50˚C. Then, the next step is extrusion. The solution, kept at 50˚C, is forced through right pore size polycarbonate filters (Whiteman) eleven times ending on the side which did not originally have the solution. The extrusion is done above the t_c. Below t_c, membrane has

tendency to foul with rigid membranes which cannot pass through the pores. The product of the extrusion is unilamellar lipids. The non-trapped NPs and dye are removed by gel exclusion chromatography in a Sephadex G-50 column with 1XPBS buffer. The first portion of the elute from the column is collected and characterized using dynamic light scattering (DLS) method. The average size of the liposomes obtained using 100 nm polycarbonate filter paper during extrusion is 250 nm.

Drug release assay

The model drug of the investigation, 5(6)-Carboxyfluorescein (CF), is responsible for the fluorescence emission from thus prepared liposomes. CF is a hydrophilic fluorescent molecule and it should be entrapped in the core of liposome. CF generates emission fluorescence at around 517 nm. The intensity of CF fluorescence gives the amount of free CF in the system. The change in fluorescence intensity is measured upon exposure to pulsed magnetic field. The fluorescence self-quenching decreases as the CF molecules come out from the liposomes.[19] The steady state fluorescence is measured at excitation wavelength 460 nm with 1 nm slits. To calculate the drug release from both control liposomes and MLs, 200 µL of thus prepared liposomes or MLs is diluted using 3 mL of 1XPBS Buffer. The emission fluorescence spectra of liposomes or MLs before exposing into pulsed magnetic field, after exposing into 10 pulses of pulsed magnetic field and after the addition of 100 µL of Triton X-100 are recorded. The addition of Triton X-100 completely releases the CF through vesicles disruption. The typical fluorescence emission spectra are shown in Figure 7.3. Same measurements are performed for other NPs.
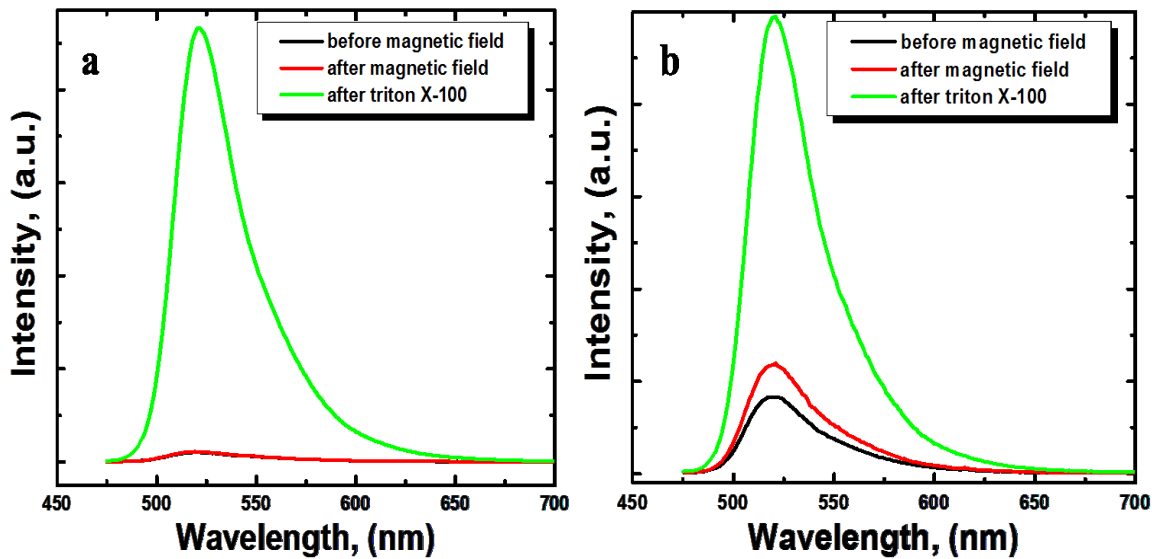
Figure 7.3 Static fluorescence emission measurements of (a) control liposome, no NP (b) magnetic NPs (Fe$_3$O$_4$) loaded liposome, before/after exposing pulsed magnetic field and after the release of all dye as model drug using Triton X-100.

The clear difference can be seen in the fluorescence emission spectra between the control liposome and magnetic NPs loaded liposome. To quantify the result, percentage release of the drug is calculated. The percentage release of the drug is calculated from the fluorescence intensity of emission spectra. For better accuracy, the surface areas under the emission spectra are calculated using Matlab program. The Matlab codes are attached in appendix. The calculated surface areas under the emission spectra are used to calculate the percentage release as

$$\% \, release = \frac{SA_{AMF} - SA_{BMF}}{SA_{AT} - SA_{BMF}} \times 100 \qquad\qquad 7.2$$

, where SA_{AMF} is the surface area after exposing into magnetic field, SA_{BMF} is the surface area before exposing into magnetic field, SA_{AT} is the surface area after the addition of Triton X-100.

147

The calculated % releases for control liposomes and Fe_3O_4 NPs loaded liposomes are tabulated in the table 7.1.

Samples	SA_{BMF}	SA_{AMF}	SA_{AT}	% release
Liposome	1.2232×10^6	1.2774×10^6	4.5549×10^7	0.12%
Liposome/Fe_3O_4	2.1313×10^6	2.9696×10^6	1.2098×10^7	8.40%

Table 7.1 Drug release data for control and magnetic NPs loaded liposomes.

The same experiment is repeated with the hydrophobic, hydrophilic and amphiphilic peptide coated Fe_3O_4 NPs, since depending on the surface property of NPs, the position of the NPs in the liposomes is fixed. The % releases of drug are calculated which are given in the following table 7.2. The percentage releases with hydrophilic and amphiphilic peptide coated Fe_3O_4 NPs are almost same. The percentage release with hydrophobic peptide coated Fe_3O_4 NPs is comparatively small. This indicates that the hydrophobic peptide coated Fe_3O_4 NPs are not incorporated in the liposomes because of the surface property of NPs.

Samples	SA_{BMF}	SA_{AMF}	SA_{AT}	% release
Hydrophobic	4.6117×10^6	4.7701×10^6	6.9581×10^7	0.24%
Hydrophilic	5.5005×10^6	7.2880×10^6	5.0060×10^7	3.57%
Amphiphilic	2.7737×10^6	4.5261×10^6	5.0989×10^7	3.63%

Table 7.2 Drug release data for hydrophobic, hydrophilic and amphiphilic peptide coated Fe_3O_4 NPs.

In order to observe the effect of osmotic pressure in the drug release, different concentration (0.33X, 3X, and 10X) of PBS solutions are used. The % releases of drug are calculated which are given in the table 7.3.

PBS	Samples	SA_{BMF}	SA_{AMF}	SA_{AT}	% release
0.33X	Liposome	3.5503×10^6	3.5720×10^6	6.8944×10^6	0.65%
	Liposome/Fe_3O_4	2.1282×10^6	2.3426×10^6	4.7956×10^6	4.5%
3X	Liposome	2.1847×10^5	2.1699×10^5	3.0875×10^6	-0.05%
	Liposome/Fe_3O_4	2.4329×10^5	2.8957×10^5	2.5625×10^6	2.0%
10X	Liposome	3.5388×10^6	3.7585×10^6	1.1852×10^8	0.2%
	Liposome/Fe_3O_4	7.5666×10^6	9.6707×10^6	7.1622×10^7	3.3%

Table 7.3 Drug release data for liposomes and Fe_3O_4 NPs loaded liposomes in different concentrations of PBS solutions.

The percentage drug release from liposome and Fe_3O_4 NPs loaded liposomes in different PBS buffer solution also show some release but are not significantly different from 1XPBS solution.

Conclusions

All the data presented here are the preliminary data. Experimental results show the percentage drug release is from 2% - 8% for the magnetic NPs loaded liposomes while there is almost no release with the control liposomes after exposing into the pulsed magnetic field. This proves that MLs can be used in instantaneous release of drug under the influence of the pulsed magnetic field. There is no data available for the pulsed magnetic field drug release to compare with, however, this percentage release, of course, is not satisfactory. Further effort should be made to optimize the percentage release by changing the different factors. For example; magnetic NPs with higher saturation magnetization, stronger magnetic field, larger size of NPs, different synthesis method of liposomes, bigger multilamellar liposomes, surface charge and surface group of NPs etc. The drug release from MLs as a function of number of pulses and discharge

potential are also studied (data are not included here) but the results are not consistent. The data that are presented here are preliminary. These data are obtained by following standard protocol using a pulsed magnetic field instead of alternating magnetic field. Our suspicion is that some chemical changes may occur once Triton X-100 is added to the MLs and it may lead to entirely different fluorescence emission. Therefore, a new protocol may be necessary to establish to control the experiment with careful and thorough investigation in future. The research is in progress.

References

1.   Bangham, A. D.; Standish, M. M.; Watkins, J. C., *J. Mol. Biol.* **1965,** *13*, 238-252.

2.   Lasic, D. D., Applications of Liposomes. In *Handbook of Biological Physics*, Lipowsky, R.; Sackmann, E., Eds. Elsevier Science: 1995; Vol. 1.

3.   Immordino, M. L.; Dosio, F.; Cattel, L., *International Journal of Nanomedicine* **2006,** *2006* (3), 297-315.

4.   Mohanraj, V. J.; Chen, Y., *Trop. J. Pharm. Res* **2006,** *5* (1), 561-573.

5.   Campbell, P., *Cytobios.* **1983,** *37* (145), 21-66.

6.   Rooijen, N. v.; Nieuwmegen, R. v., *Immunological Investigations* **1980,** *9* (3), 243-256.

7.   Benyettou, F.; Chebbi, I.; Motte, L.; Seksek, O., *J. Mater. Chem.* **2011,** *21*, 4813-4820.

8.   Grislain, L.; Couvreur, P.; Lenaerts, V.; Ronald, M.; Deprez-Decampeneere, D.; Speiser, P., *Int. J. Pharm.* **1983,** *15* (3), 335-345.

9.   Zia, Q.; Farzuddin, M.; Ansari, M. A.; Alam, M.; Ali, A.; Ahmad, I.; Owais, M., Novel Drug Delivery Systems for Antifungal Compounds. In *Combating Fungal Infections: Problems and Remedy*, Ahmad, I.; Owais, M.; Shahid, M.; Aqil, F., Eds. Springer: 2010.

10.   http://techtransfer.universityofcalifornia.edu/NCD/19354.html.

11.   Hofmann-Amtenbrink, M.; Rechberg, B. V., Superparamagnetic Nanoparticles for Biomedical Applications. In *Nanostructured for Biomedical Applications*, Tan, M. C., Ed. Transword Research Network: Kerala, India, 2009.

12.   Wu, W.; He, Q.; Jiang, C., *Nanoscale Res Lett* **2008,** *3*, 397-415.

13.   Lesieur, S.; Grabielle-Madelmont, C.; Menager, C.; Cabuil, V.; Dadhi, D.; Pierrot, P.; Edwards, K., *J. Am. Chem. Soc* **2003,** *125* (5266-5267).

14.   Hu, S. H.; Liu, T. Y.; Huang, H. Y.; Liu, D. M.; Chen, S. Y., *Langmuir* **2008,** *24*, 239-244.

15.   Kohler, N.; Sun, C.; Wang, J.; Zhang, M., *Langmuir* **2005,** *21*, 8858-8864.

16.   Nappini, S.; Bonini, M.; Bombelli, F. B.; Pineider, F.; Sangregorio, C.; Baglioni, P.; Norden, B., *Soft Matter* **2010,** *7*, 1025-1037.

17.   Chen, Y.; Bose, A.; Bothun, G. D., *ACS Nano* **2010,** *4* (6), 3215-3221.

18.   Babincova, M.; Cicmanec, P.; Altanerova, V.; Altaner, C.; Babinec, P., *Bioelectrochemistry* **2002,** *55*, 17-19.

19.   Nappini, S.; Massimo, B.; Francesca, R.; Baglioni, P., *Soft Matter* **2011,** *7*, 4801-4811.

20.   Soenen, S. J.; Velde, G. V.; Ketkar-Atre, A.; Himmelreich, U.; Cuyper, M. D., *WIREs Nanomedicine and Nanobiotechnology* **2011,** *3*, 197-211.

21.   Li, Z.; Sun, Q.; Gao, M., *Angewandte Chemie (International ed. in English)* **2005,** *117*, 125-128.

22.   Elersic, K.; Pavlic, J. I.; Iglic, A.; Vesel, A.; Mozetic, M., *Chem. Phys. Lipids* **2012,** *165*, 120-124.

23.   Maherani, B.; Arab-tehrany, E.; Kheirolomoom, A.; Reshetov, V.; Stebe, M. J.; Linder, M., *Analyst* **2012,** *137*, 773-786.

24.   Sharma, A.; Sharma, U. S., *Int. J. Pharm.* **1997,** *154*, 123-140.

25.   http://avantilipids.com/index.php?option=com_content&view=article&id=1384&Itemid=372.

26.   Basel, M. T. Targeting Cancer Therapy: Using Protease Cleavage Sequences to Develop more Selective and Effective Cancer Treatments. Kansas State University, 2010.

Appendix A - Supplemental Material for Faraday rotation in Alternating Magnetic Field

Theory of Modeling Faraday rotation

The Faraday rotation[1] in a medium is due to the difference of propagation of right and left circularly polarized light through it, when a magnetic field is applied along the propagation direction (z). The theory is closely related to that for optical rotation.[2] The dielectric permittivities ε_R and ε_L for the two polarizations will be slightly different, causing one polarization to be phase shifted relative to the other, after the light propagates some distance z. Once these permittivities are known for the composite medium made of core/shell particles in water, the Faraday rotation can be found.

ε_R and ε_L are the eigenvalues of the permittivity tensor in Cartesian coordinates, written as,[3]

$$\varepsilon = \begin{pmatrix} \varepsilon_{xx} & \varepsilon_{xy} \\ -\varepsilon_{xy} & \varepsilon_{xx} \end{pmatrix} \Rightarrow diagonalization \Rightarrow \tilde{\varepsilon} = \begin{pmatrix} \varepsilon_{xx} - i\varepsilon_{xy} & 0 \\ 0 & \varepsilon_{xx} + i\varepsilon_{xy} \end{pmatrix} \qquad 1$$

The diagonal elements are ε_R and ε_L, which gives

$$\varepsilon_{xx} = \frac{1}{2}(\varepsilon_R + \varepsilon_L), \qquad \varepsilon_{xy} = \frac{i}{2}(\varepsilon_R - \varepsilon_L) \qquad\qquad 2$$

Each polarization propagates independently with a wave vector, $k_{R,L} = \frac{\omega}{c}\sqrt{\varepsilon_{R,L}}$. Then the Faraday rotation of linearly polarized light after propagating a distance z is found to be

$$\varphi = \frac{1}{2}Re\{k_R - k_L\}z = \frac{\omega}{2c}Re\left\{-i\frac{\varepsilon_{xy}}{\sqrt{\varepsilon_{xx}}}\right\} \qquad\qquad 3$$

The ellipticity angle produced by the difference in extinction of the two polarizations is given instead by using the imaginary part. The Verdet constant ν is φ normalized per applied magnetic induction B and unit distance,

$$\nu = \frac{\varphi}{zB} = (\pi/\lambda B)Re\left\{-i\varepsilon_{xy}/\sqrt{\varepsilon_{xx}}\right\} \qquad\qquad 4$$

As ε_{xy} is proportional to B except at very high fields, ν does not depend on B. We use this approach here to get φ, based on finding the effective dielectric functions for right/left polarizations of the composite water-nanoparticle medium using a Drude model.

Dielectric Properties

The Drude model for the electron response can be used to estimate the absorption and Faraday rotation effects, due to both the Fe_2O_3 core and the gold shell. Both of these are closely related. A resonance in the absorption will correspond to a similar resonance effect in the Faraday rotation. We take the approach of finding an accurate description of the dielectric functions $\varepsilon(\omega)$, based on experimental measurements of absorption in solutions of nanoparticles. Once $\varepsilon(\omega)$ is known separately for both the core and the shell materials, the resulting Faraday rotation of core/shell nanoparticles in solution can be calculated as described below:

The frequency-dependent relative dielectric permittivity of a medium, due to bound electrons at a single resonance ω_0 combined with free electrons of plasma frequency ω_p, is taken as[4,5]

$$\varepsilon = 1 - \frac{g_0^2}{\omega^2 - \omega_0^2 + i\gamma_0\omega - \nu\omega\omega_B} - \frac{\omega_p^2}{\omega^2 + i\gamma_p\omega - \nu\omega\omega_B} \qquad\qquad 5$$

For the bound electrons, ω_0 is the binding frequency, g_0 is the oscillator strength, and γ_0 is the damping frequency. The last term in (5) represents the free electrons, with plasma frequency ω_p and damping frequency γ_p. The applied magnetic field (along z) responsible for the Faraday rotation enters into both terms, in the cyclotron frequency, $\omega_B = eB_z/m^*$. The helicity is $\nu = +1/-1$ for left/right circular polarization. That term, due to the Lorentz force, leads to Faraday rotation, applying expression (5) separately for both polarizations.

For the gold shell, we assume that the free electron plasma is the main contribution to ε, although a contribution from bound electrons[6] must also be included to move the plasmon frequency of gold nanoparticles into the visible. For the free electrons, we use the bulk value plasma frequency, $\omega_p = 1.37 \times 10^{16}$ rad/s ($\lambda = 138.5$ nm), and a scattering time $\tau = 9.1$ fs, effective mass $m^* = m_e$, and damping frequency that includes scattering from the shell surfaces,[7] according to

$$\gamma_p = \frac{1}{\tau} + \frac{v_F}{d} \qquad\qquad 6$$

The Fermi velocity is $v_F = 1.40 \times 10^6$ m/s and d is the thickness of the gold shell. For the bound electrons, we do not use a limiting dielectric constant like $\varepsilon_\infty \approx 10$, as in Ref. 7 to get the plasmon resonance for spherical gold particles near 530 nm. Instead, the average effect of the bound electrons is represented approximately by a single resonance term proportional to g_0^2 as in Eq. (5). This makes the inclusion of Faraday effects rather simple, compared to a more correct treatment of the interband transitions. The parameters have been fitted from the absorption spectrum of a solution of 17 nm diameter (average) gold nanoparticles in water (similar to that explained for γ-Fe$_2$O$_3$ parameter fitting in the following paragraph). For description of the absorption, especially near the plasmon resonance, the fitting parameters are found to be $g_0 = 4.43 \times 10^{15}$ rad/s, $\omega_0 = 3.86 \times 10^{15}$ rad/s ($\lambda_0 = 488$ nm), and $\gamma_0 = 6.22 \times 10^{15}$ rad/s (scattering time $\tau_0 = 1/\gamma_0 = 1.61$ fs). This fit is shown in Figure A.1.
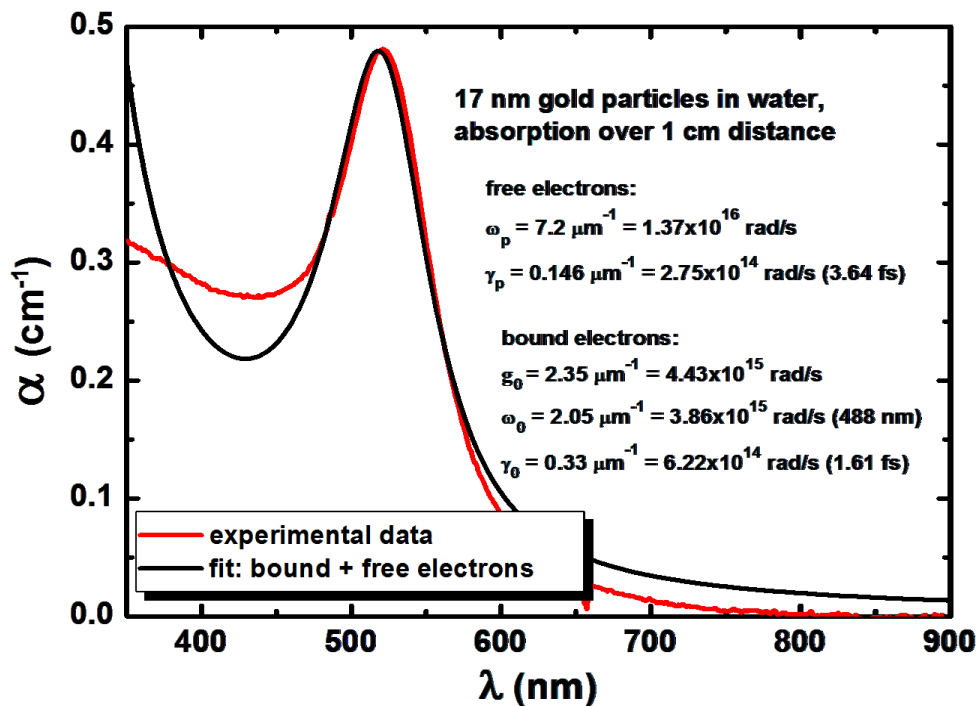
Figure A.1 Fit of experimentally measured absorption of gold nanoparticle solution to model dielectric function including both free and bound electrons.

The fit is close to the experimental data around the plasmon resonance, and somewhat overestimates the absorption at longer wavelengths, but the model should not be taken seriously in the ultraviolet. This, however, is not a problem, because it is the change in the frequency of the plasmon resonance with changing gold shell thickness that is responsible for many of the interesting plasmonic effects. As long as this model gives a reasonable description of that resonance, it should be able to suggest how the absorption and Faraday rotation vary with gold shell modifications.

Describing the maghemite core [γ-Fe$_2$O$_3$] is complex, because it has several different absorption resonances. There is at least one strong resonant absorption in the ultraviolet that is

responsible for Faraday rotation.[8] Its tail produces the leading contribution to the absorption $\alpha(\omega)$ in the visible. The absorption spectrum of γ-Fe_2O_3 particles over 350 nm < lambda < 700 nm, not including the weaker absorption band from 460 nm -- 560 nm, was fit by using the above expression (5), see Figure A.2. For a volume fraction f of spherical particles of dielectric constant ε in water (the host medium, with ε_a =1.777), the absorption is $\alpha = \frac{\omega}{c} Im\{\sqrt{\varepsilon_{eff}}\}$, where ε_{eff} results from the Maxwell Garnett effective medium theory[9] (MG equation),

$$\frac{\varepsilon_{eff} - \varepsilon_a}{\varepsilon_{eff} + 2\varepsilon_a} = f \frac{\varepsilon - \varepsilon_a}{\varepsilon + 2\varepsilon_a} \qquad\qquad 7$$

Assuming only bound electrons ($\omega_p = 0$) we found that $g_0 = 5.20 \times 10^{15}$ rad/s, $\omega_0 = 5.06 \times 10^{15}$ rad/s ($\lambda_0 = 372$ nm), and $\gamma_0 = 2.89 \times 10^{15}$ rad/s ($\tau_0 = 1/\gamma_0 = 0.347$ fs) describes the underlying absorption curve of Fe_2O_3 (Figure A.2).[7]
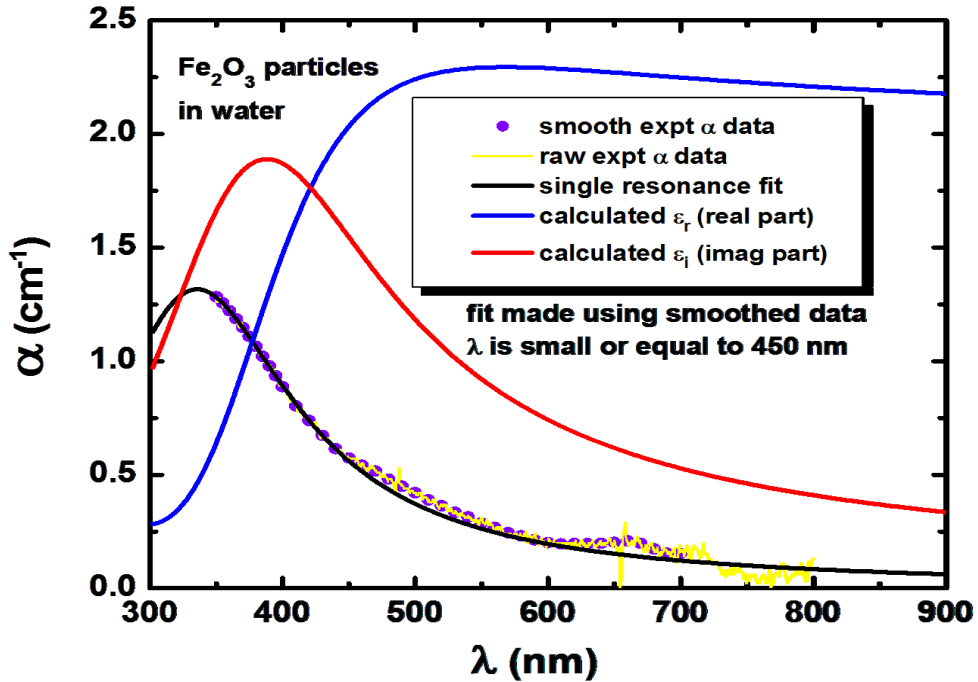
Figure A.2 Fit of absorption spectrum of maghemite nanoparticles in water solution for determing its dielectric function. The real and imaginary parts of the resulting $\varepsilon(\lambda)$ are also shown.

The other parameters needed to describe the maghemite core are its domain saturation magnetization M = 414 kA/m, and its anisotropy constant K = 4700 J/m³.[8] The cores have average radius b=4.85 nm, volume $V = \frac{3}{4}\pi b^3$ = 478 nm³, and magnetic moment $m = MV$, and are super-paramagnetic, as can be seen by the ratio of magnetic anisotropy energy KV = 14 meV to the thermal energy $k_B T$ = 26 meV (at 300 K). Their average magnetic moment in an externally applied magnetic induction B follows the classical Langevin function,

$$\langle m_z \rangle = m\langle cos\theta \rangle = m\left[cothx - \frac{1}{x}\right] \approx \frac{1}{3}mx, \qquad x \equiv \frac{mB}{k_B T} \qquad\qquad 8$$

For the permanent magnetization in these single domain particles, the internal magnetic field is $H_{in} = -\frac{1}{3}M$ and the internal magnetic induction is $B_{in} = \mu_0(H_{in} + M) = \frac{2}{3}\mu_0 M$. The component along z is $B_{in,z} = B_{in}\langle cos\theta \rangle = \frac{2}{3}\mu_0 M\frac{x}{3} = \left(\frac{2}{9}\mu_0 VM^2/k_B T\right)B$. This internal magnetic induction is amplified by the factor $\frac{2}{9}\mu_0 VM^2/k_B T$ = 5.5, which helps to enhance the Faraday rotation compared to that in a non-magnetized medium.

For pure particles of either gold or maghemite in a water solution, the MG theory (7) can be applied to calculate the Faraday rotation. Figure A.3 indicates how the plasmon peak in $\alpha(\omega)$ for gold is accompanied by a similar peak in the Verdet function, $v(\omega)$. Further, the plasmon width increases for smaller particles, due to the enhanced surface scattering term.
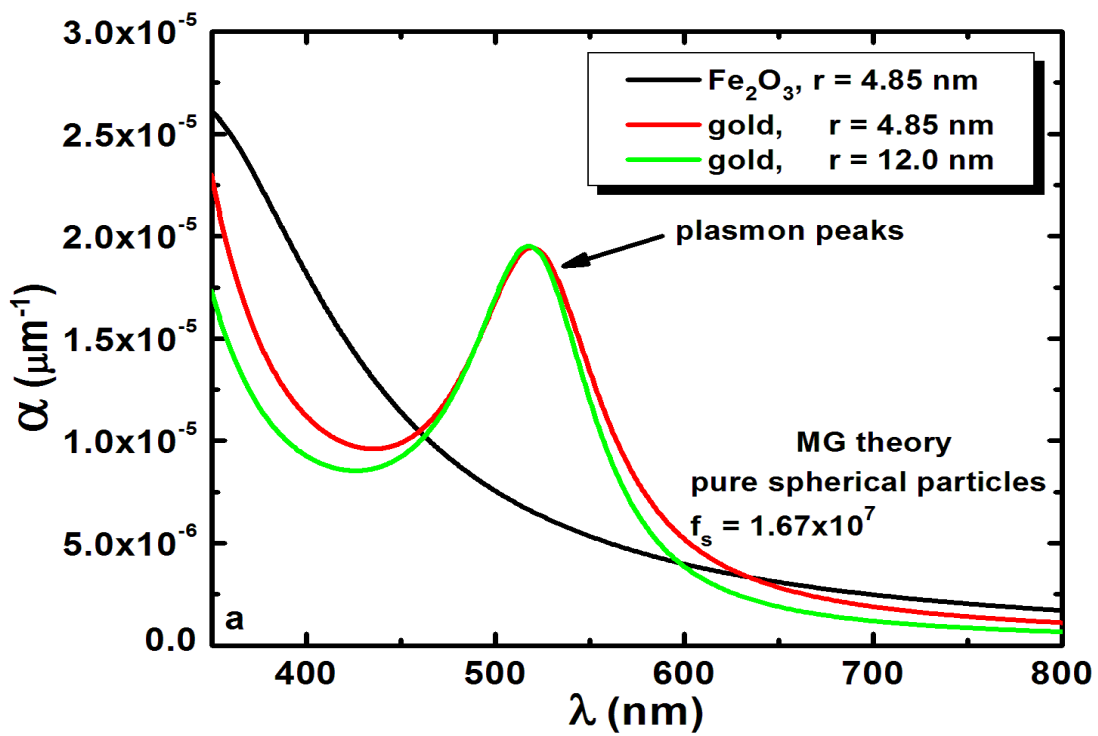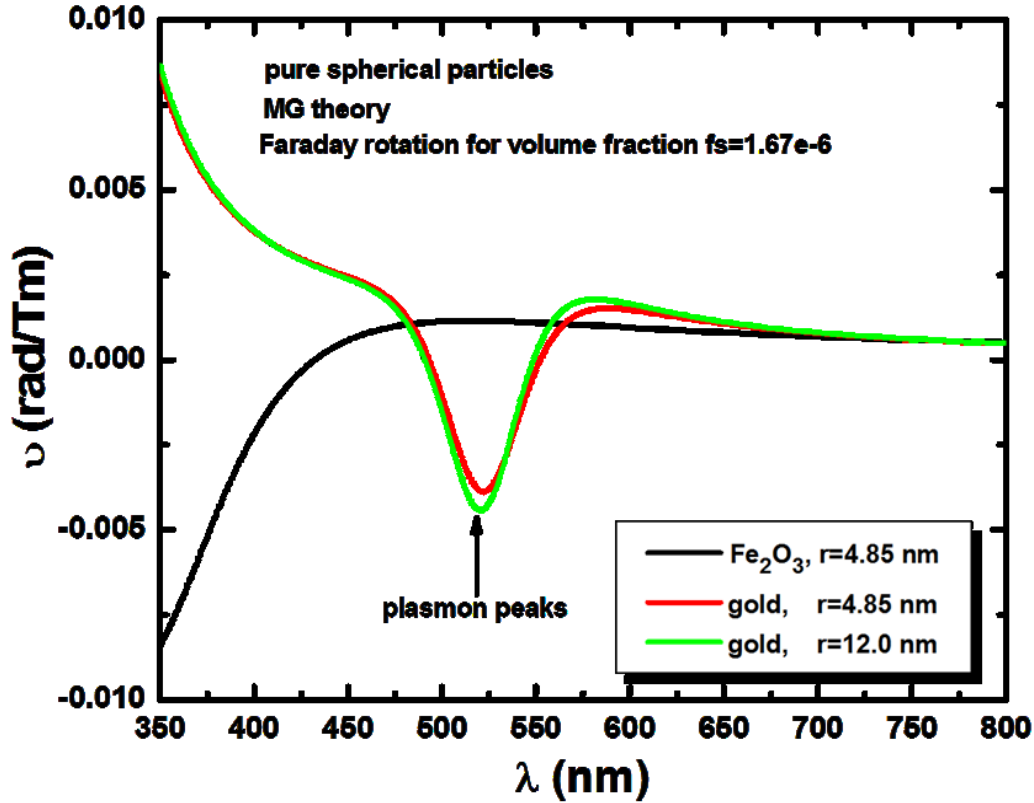
Figure A.3(a).

Figure A.3(b).

Figure A.3 Absorption (a) and Faraday rotation or Verdet constant (b) calculated for nanoparticles indicated, in water solution, using the Maxwell Garnett theory at a volume fraction $f_s = 1.67 \times 10^{-6}$. The plasmon resonance appears clearly in both quantities, and is wider for smaller particles.

Core/shell particle's permittivity ε_s

The individual particles are assumed to be spherical, with a maghemite core (ε_c) of radius b, surrounded by a shell of gold (ε_b) to outer radius a, much less than the wavelength of light being considered. The particle is immersed in a medium (water) with dielectric constant ε_a. From their separate frequency-dependent permittivities, we require first the effective permittivity of

160

one spherical particle, ε_s. This can be found equivalently either by (1) finding the effective polarization and average internal electric field using electrostatics, or (2) applying Maxwell Garnett theory[9, 10] to a single particle, taking the Fe_2O_3 core as an inclusion of internal volume fraction $f_c = \left(\frac{b}{a}\right)^3$ within the gold shell "host" medium. The composite particle's dielectric function ε_s is found to be

$$\varepsilon_s = \varepsilon_b \frac{1+2\beta_c}{1-\beta_c}, \quad \beta_c = f_c \frac{\varepsilon_c - \varepsilon_b}{\varepsilon_c + 2\varepsilon_b}, f_c = \left(\frac{b}{a}\right)^3 \qquad \text{(9, Solution of MG equation)}$$

This effective permittivity is also expressed as $\varepsilon_s = \varepsilon_b + \alpha_s/F_s$, where the susceptibility and internal field per applied field of a spherical particle surrounded by a host medium ε_a are found via electrostatics as

$$\alpha_s = \frac{\langle P_{in} \rangle}{E_0} = 3\varepsilon_a \frac{\varepsilon_s - \varepsilon_a}{\varepsilon_s + 2\varepsilon_a}, \qquad F_s = \frac{\langle E_{in} \rangle}{E_0} = \frac{3\varepsilon_a}{\varepsilon_s + 2\varepsilon_a} \qquad\qquad 10$$

Effective Composite Medium

These particles are dispersed into water with a volume fraction $f_s = n_s V_s$, where $n_s \approx 3.5 \times 10^{18}/m^3$ is their number density and $V_s = 4\pi a^3/3$ is their volume that depends on the outer radius of the gold shell. We consider two different ways to determine the effective permittivity of the solution: (1) Maxwell Garnett effective medium theory, assuming that the spheres are well separated and scatter light independently; (2) Bruggeman theory,[9, 10] supposing that the spheres combine into clusters composed from hundreds to thousands of the core/shell particles in a closed packed arrangement with a volume fraction $f_{Br} \approx 0.74$.

In the MG theory the effective permittivity of the composite can be expressed as

$$\varepsilon_{\text{eff}} = \varepsilon_a + \frac{f_s \alpha_s}{[1 - f_s(1 - F_s)]} \quad \text{or as} \quad \varepsilon_{\text{eff}} = \varepsilon_a \frac{1 + 2\beta_s}{1 - \beta_s} , \quad \beta_s = f_s \frac{\varepsilon_s - \varepsilon_a}{\varepsilon_s + 2\varepsilon_a} \qquad \qquad 11$$

This expression is evaluated separately for left/right polarizations, from which the Faraday rotation can be found using (2) and (3). Some results for absorption and Faraday rotation due to core/shell particles are shown in Figure A.4. The important aspect of the results is that the plasmon resonance starts at long wavelengths for very thin gold shells, and moves towards about 520 nm with increasing shell thickness. Note that the volume fraction f_s increases with thickness of the gold shell, as the number density of particles was nearly constant in experiments.
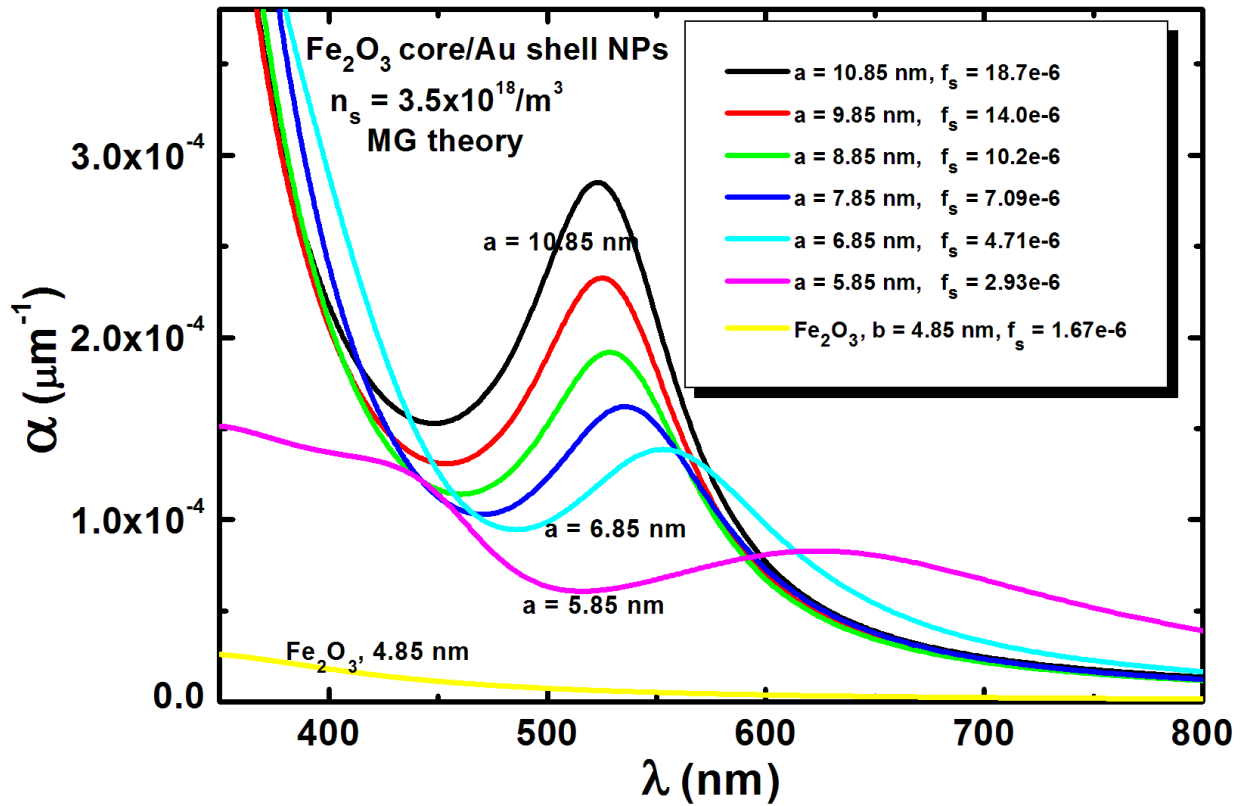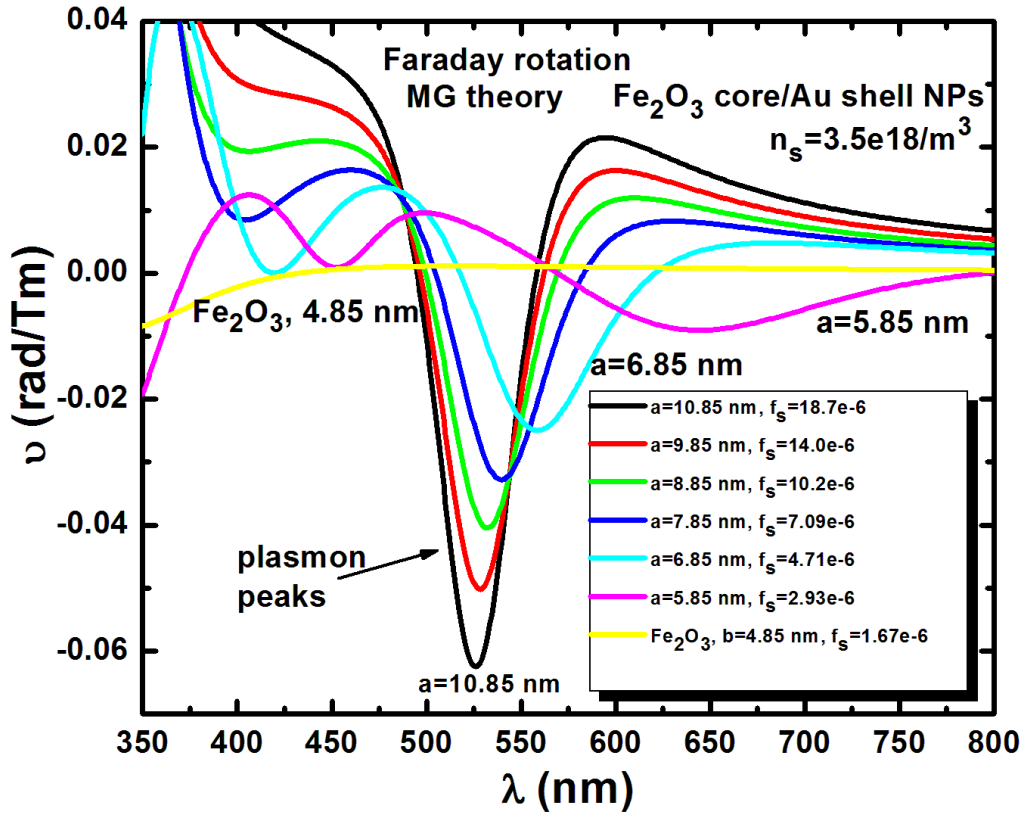
Figure A.4(a).

Figure A.4(b).

Figure A.4 Absorption (a) and Faraday rotation (b) for core/shell nanoparticles in water, showing the variations with increasing gold shell thickness. Notably, the plasmon peak moves towards shorter wavelength with increasing shell thickness.

To include the clustering effects via the Bruggeman theory, we first find the effective permittivity of a cluster, ε_{cl}, composed from volume fraction f_{Br} of core/shell spheres surrounded by volume fraction $1 - f_{Br}$ of water host (ε_a). The cluster effective permittivity ε_{cl} solves the Bruggeman equation,

$$f_{Br} \frac{\varepsilon_s - \varepsilon_{cl}}{\varepsilon_s + 2\varepsilon_{cl}} + (1 - f_{Br}) \frac{\varepsilon_a - \varepsilon_{cl}}{\varepsilon_a + 2\varepsilon_{cl}} = 0 \qquad\qquad 12$$

163

where the first term represents the contribution of the spheres surrounded by averaged cluster, and the second term represents the water surrounded by averaged cluster. The solution for the effective permittivity of a cluster is found to be

$$\varepsilon_{cl} = \frac{1}{4}\left\{(2 - 3f_{Br})\varepsilon_a + (3f_{Br} - 1)\varepsilon_s + \sqrt{[(2 - 3f_{Br})\varepsilon_a + (3f_{Br} - 1)\varepsilon_s]^2 + 8\varepsilon_a\varepsilon_s}\right\} \qquad 13$$

It is interesting to note that the limit $f_{Br} = 1$ of this Bruggeman cluster effect just recovers the simpler MG result (i.e., Eq. (12) gives $\varepsilon_{cl} = \varepsilon_s$). Both theories predict the blue shift of the plasmon resonance in the absorption spectrum with increasing gold shell thickness (Figures A.4 and A.5).
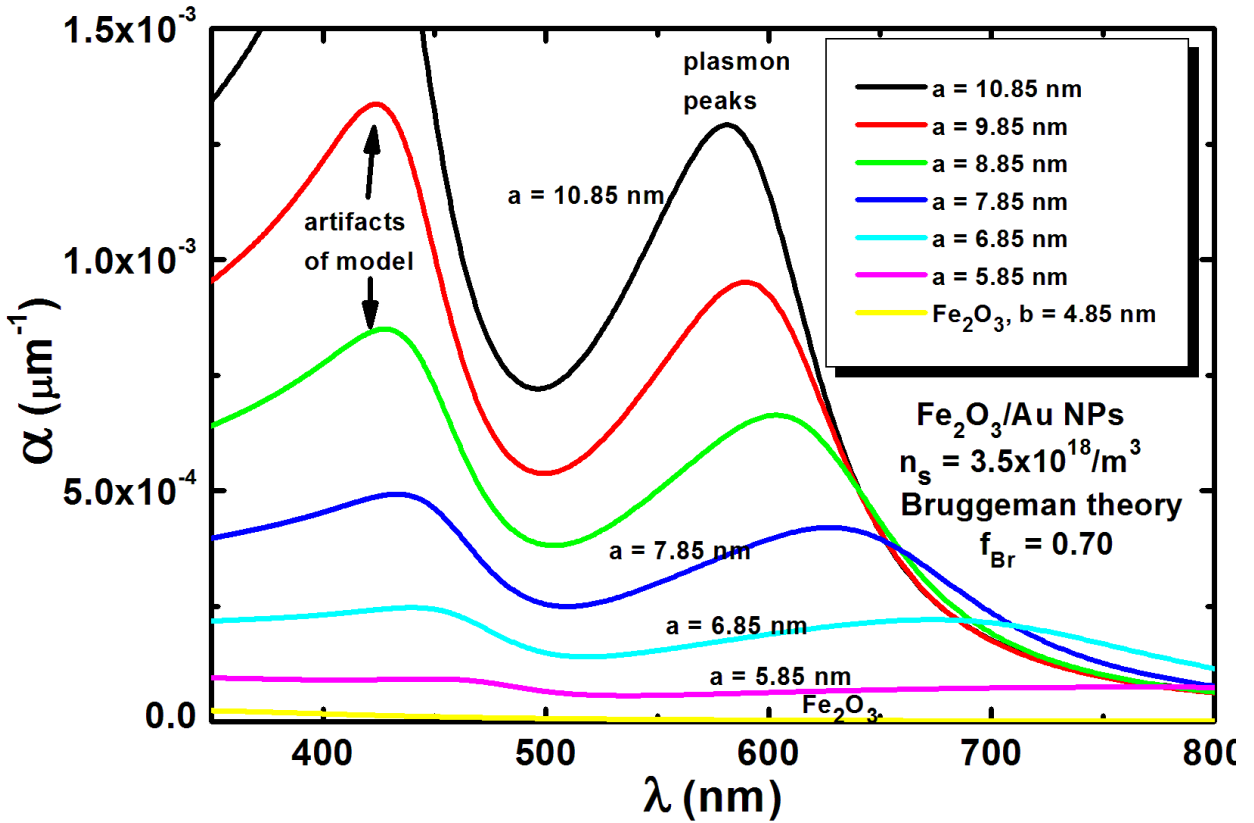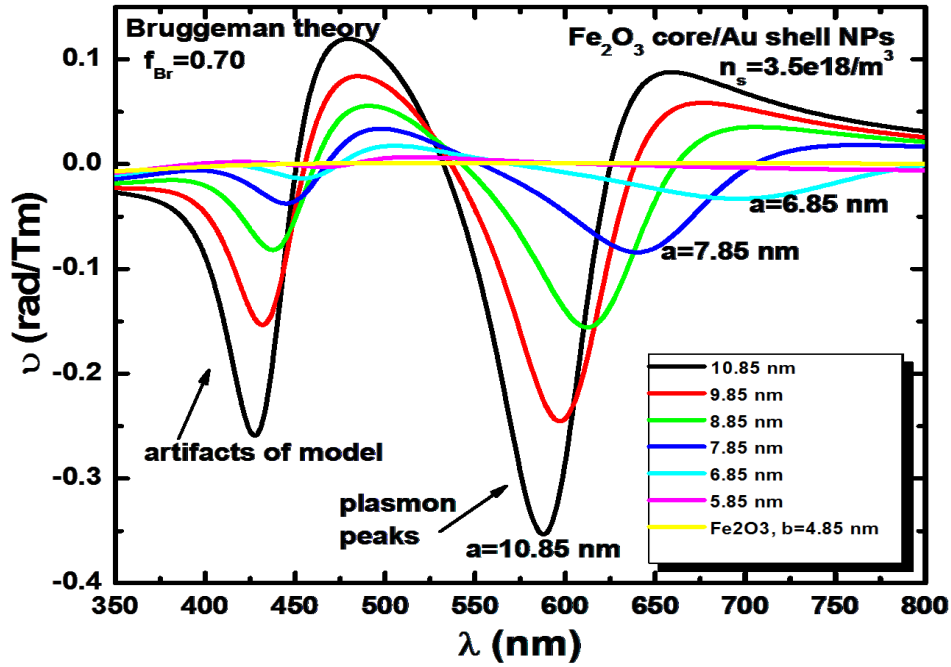
Figure A.5(a).

Figure A.5(b).

Figure A.5 Absorption (a) and Faraday rotation (b) for core/shell particle solutions in water, including strong clustering effects via the Bruggeman theory. The peaks below 450 nm are artifacts due to the single resonance assumed for bound gold electrons. The plasmon peak does is slightly higher than that found without clustering effects.

Once ε_{cl} is found, we again apply MG theory to get ε_{eff} due to these clusters dispersed at a low volume fraction f_{cl} in the water (for both left/right polarizations). [Note: At low volume fraction, the MG and Bruggeman theories give the same effective permittivity.] The number density of clusters in the water is $n_{cl} = n_s/N_s$, where $N_s = f_{Br}V_{\text{cluster}}/V_s$ is the number of core/shell spheres in a cluster. Then the volume fraction of clusters in the water is $f_{cl} = n_{cl}V_{\text{cluster}} = f_s/f_{Br}$. This does not depend on the size of the cluster, just on its packing density. The final application of the MG theory gives the effective permittivity of the composite medium,

$$\varepsilon_{\text{eff}} = \varepsilon_a \frac{1+2\beta_{cl}}{1-\beta_{cl}}, \qquad \beta_{cl} = f_{cl} \frac{\varepsilon_{cl}-\varepsilon_a}{\varepsilon_{cl}+2\varepsilon_a} \qquad\qquad\qquad 14$$

This is used in Eqs. (2) and (3) to get the Faraday rotation, including the clustering effects. Although the clusters have typical sizes from 80 nm to 160 nm across, only their internal packing fraction was needed in the theory, not their size.

Figure A.5 shows the results of using a cluster packing fraction $f_{Br} = 0.7$, close to the hard sphere value. Although clustering effects are probably important, such a large value of packing fraction does not fit the peak in the absorption very well, as seen in Figure A.6; both the absorption and Faraday rotation plasmon peaks fall at a wavelength that is too long. In fact the absorption peak's position with shell thickness is better fitted using $f_{Br} \approx 0.035$ as seen in Figure A.6.
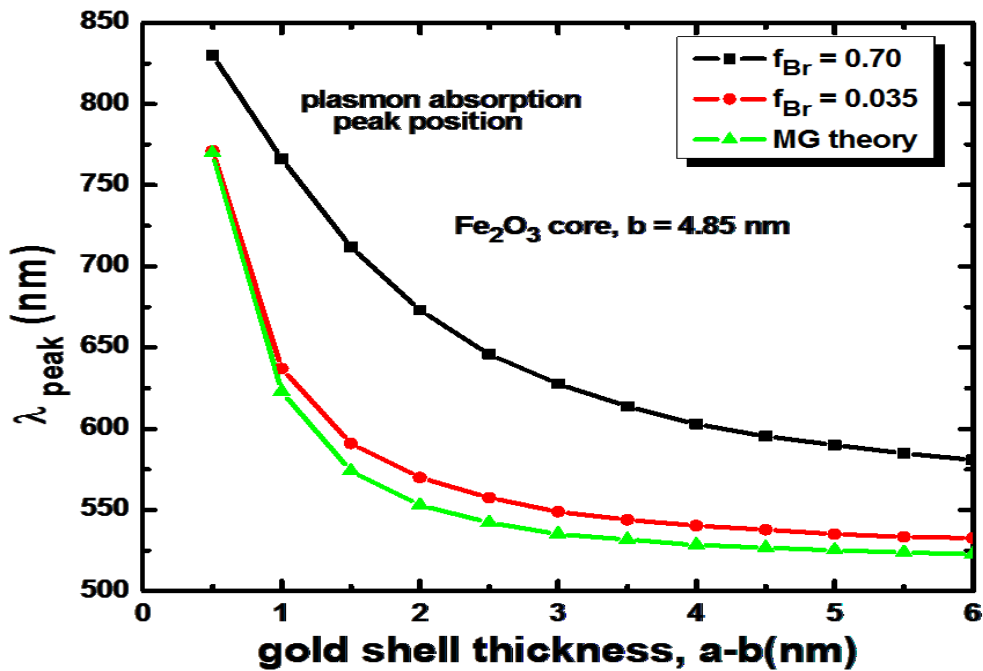
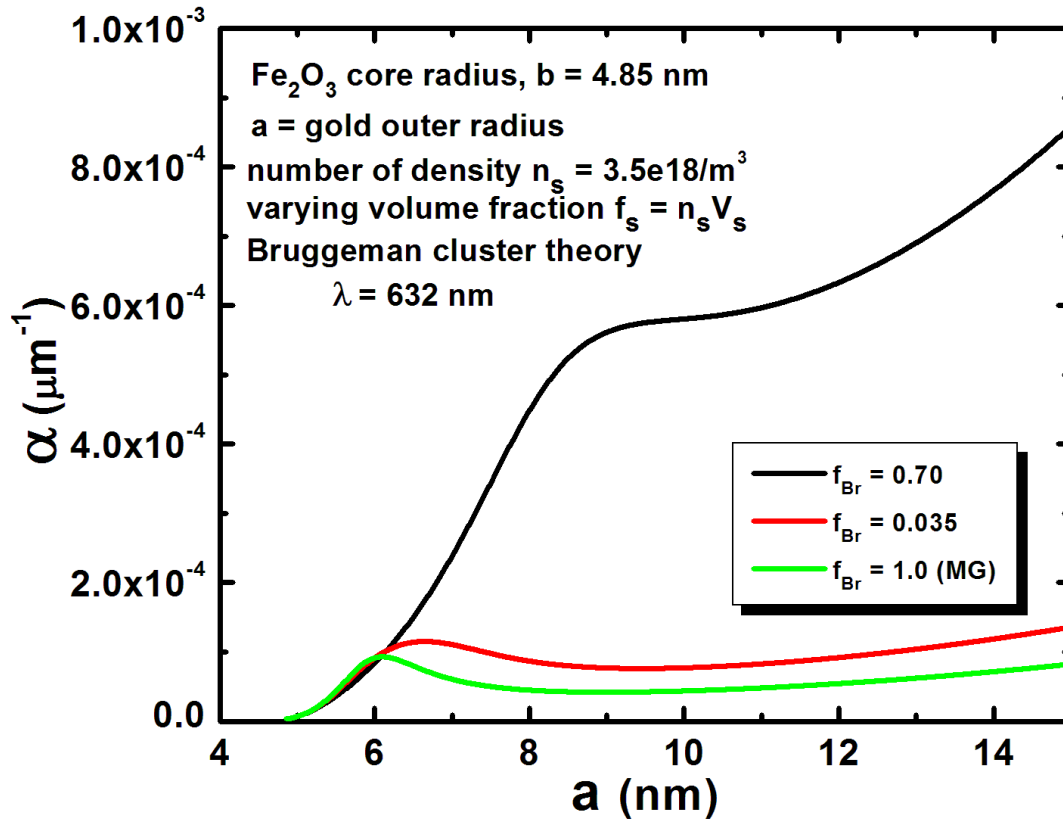Figure A.6(a).

Figure A.6(b).

Figure A.6 Comparison of different clustering levels, showing (a) the position of the gold plasmon absorption peak and (b) the absorption of nanoparticle solution at 633 nm with increasing gold shell thickness. The Maxwell Garnett theory does not include clustering effects.
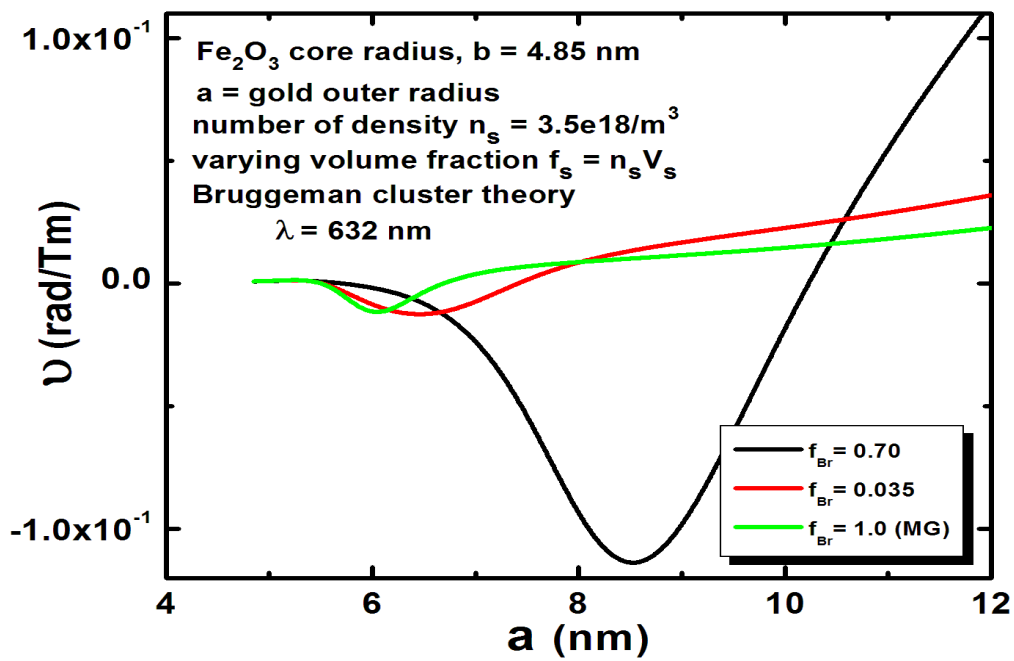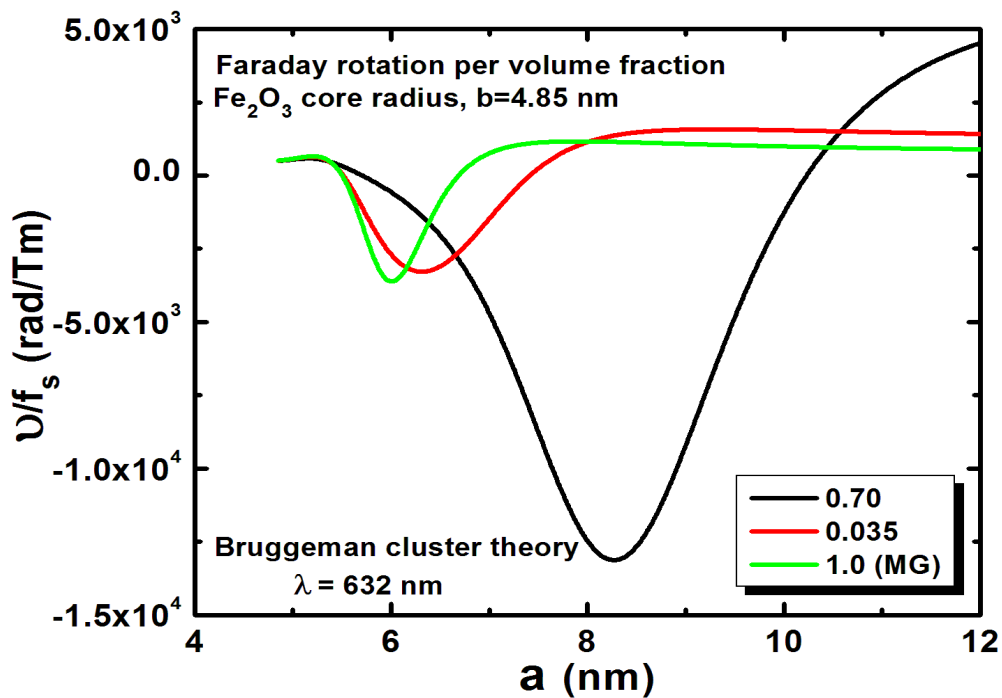
Figure A.7(a).

Figure A.7(b).

Figure A.7 Effect of clustering strength on Faraday rotation at 633 nm, using the Bruggeman theory. Part (a) shows the Verdet constant with increasing gold shell thickness. Part (b) shows the Verdet constant normalized by the volume fraction of spherical nanoparticles.

Further, the net Faraday rotation [Eq. (3)] and Verdet constant [Eq. (4)] are proportional to the particle volume fraction, f_s, when $f_s \ll 1$. Thus, some results are presented for the Verdet constant normalized by volume fraction, v/f_s, as shown in Figure A.7. The experimentally measured Faraday rotation seems to be more consistent with the clustering model at a fairly large packing fraction like 70%. However, probably a more complete description of nanoparticle interactions is needed to consistently describe both the absorption and Faraday rotation spectra of these nanoparticle solutions simultaneously.

Nevertheless, this calculation shows that the blue-shifting of the gold plasmon peak with increasing gold shell thickness is reflected in the Faraday rotation spectrum, as seen in the downward peak in Figure A.7. The strength of the clustering or other interparticle interactions or interference terms can be expected to modify the magnitude and width of this downward peak, but regardless of these details, it is ultimately linked to the blue-shifting of the gold plasmon mode.

In addition to the calculation above, the Faraday rotation spectra of the gold, Fe_2O_3 and gold coated Fe_2O_3 nanoparticles (See TEM image Figure A.9) are measured as shown in Figure A.8.
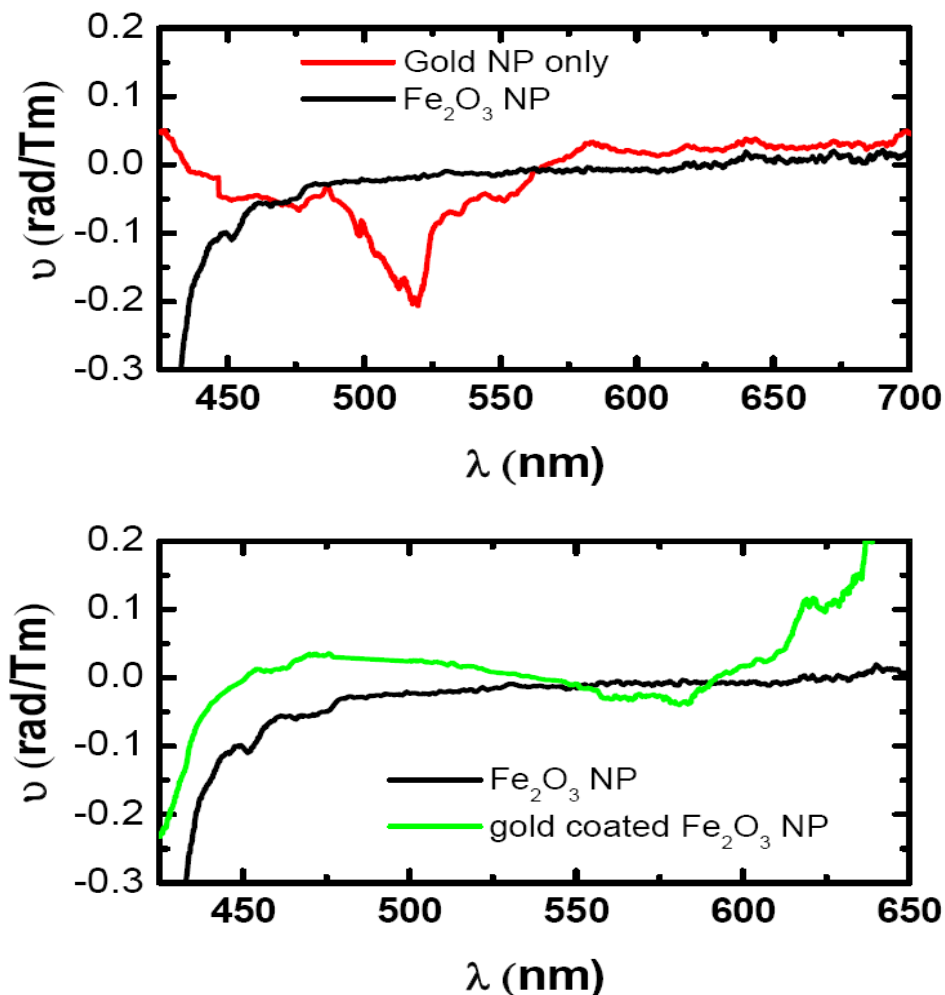
Figure A.8 TOP Faraday rotation spectrum of gold NP and Fe₂O₃ taken at 4.2 Tesla with a pulsed magnet BOTTOM Faraday rotation spectrum of gold coated Fe₂O₃ NP and Fe₂O₃ taken at 4.2 Tesla with a pulsed magnet.

The calculation accurately predicts the dip in the faraday rotation of the gold NPs at the plasmon resonance peak. This spectral feature is shifted for the gold coated nanoparticles to the red again as expected based on the calculation and in agreement with the original SuPREMO paper. The magnitude of the Faraday rotations is still larger than the predicted, but smaller than the experiments taken at 632 nm. We speculate the difference between the sets of experimental data could be the result of the relatively large magnetic field used to obtain the Faraday rotation

spectra (4.2 Tesla) compared to the 632 nm data (0.06 Tesla) and the faster speed (10 kHz vs 366 kHz).
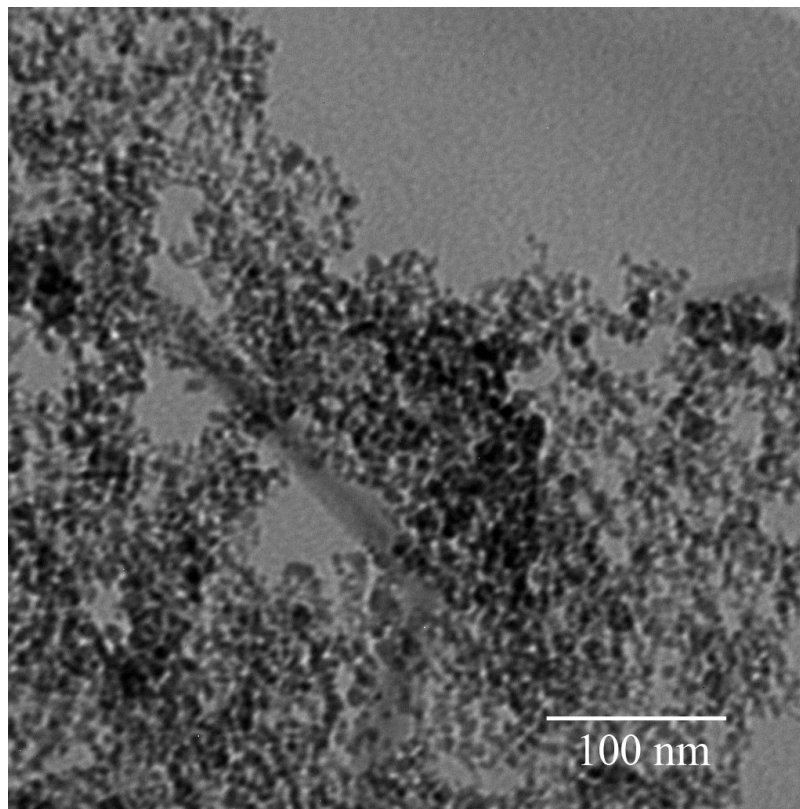
Figure A.9 Low resolution image of the gold coated Fe$_2$O$_3$ NP used in Figure A.8.

Supplemental References

1.   Hecht, E., Optics. **1997**, 366-368.

2.   Jones, L. L.; Eyring, H., A Model for Optical-Rotation. *J. Chem. Educ.* **1961,** 38, (12), 601-&.

3.   Xia, T. K.; Hui, P. M.; Stroud, D., Theory of Faraday-Rotation in Granular Magnetic-Materials. *Journal of Applied Physics* **1990,** 67, (6), 2736-2741.

4.   Palik, E. D.; Henvis, B. W., A Bibliography of Magnetooptics of Solids. *Appl. Opt.* **1967,** 6, (4), 603-603.

5.   Jackson, J. D., *Electrodynamics*. 1998.

6.   Scaffardi, L. B.; Tocho, J. O., Size dependence of refractive index of gold nanoparticles. *Nanotechnology* **2006,** 17, (5), 1309-1315.

7.   Antoine, R.; Brevet, P. F.; Girault, H. H.; Bethell, D.; Schiffrin, D. J., Surface plasmon enhanced non-linear optical response of gold nanoparticles at the air/toluene interface. *Chemical Communications* **1997**, (19), 1901-1902.

8.   Tepper, T.; Ilievski, F.; Ross, C. A.; Zaman, T. R.; Ram, R. J.; Sung, S. Y.; Stadler, B. J. H., Magneto-optical properties of iron oxide films. *Journal of Applied Physics* **2003,** 93, (10), 6948-6950.

9.   Mallet, P.; Guerin, C. A.; Sentenac, A., Maxwell-Garnett mixing rule in the presence of multiple scattering: Derivation and accuracy. *Phys. Rev. B* **2005,** 72, (1).

10.   Bruggeman, D. A. G., Berechnung verschiedener physikalischer Konstanten von heterogenen Substanzen. II. Dielektrizitätskonstanten und Leitfähigkeiten von Vielkristallen der... *Annalen der Physik* **1936,** 417, (7).

Appendix B - Operation and safety of pulsed magnets

Introduction

While continuing sinusoidal magnetic fields provide us with a set of convenient experiments currently available in our lab, more control over the shape, amplitude and carrier frequency of the magnetic fields is needed to achieve a better alignment of the nanoparticles with respect to magnetic field. Based on previous designs, our group has developed a pulsed magnet for the various experiments proposed in the proposal. Figure B.1 shows the experimental design of the RLC circuit to produce pulsed magnetic fields. The capacitor of circuit is charged up from a charger power supply up to10 kV. The capacitor then is discharged by means of a triggered high power switch based on a spark gap[82] switch capable of supporting large transient currents. The current rush (several tens of thousands of amps) from the capacitor discharge results in transient currents within the coil, which in turn produce strong magnetic pulses. The damping of the oscillatory behavior is controlled by the resistance of the RLC circuit, which allows manipulation of the magnetic field during the pulse duration. Resistance on the order of 1 Ω will result in an over damped case when oscillation no longer can be observed for the frequencies of interest (10-400 kHz). Our recently developed pulsed magnet can produce several Teslas magnetic field. The figure above shows the experimentally measured oscillatory magnetic field from Faraday rotation of water at a discharge potential of 2330 V.
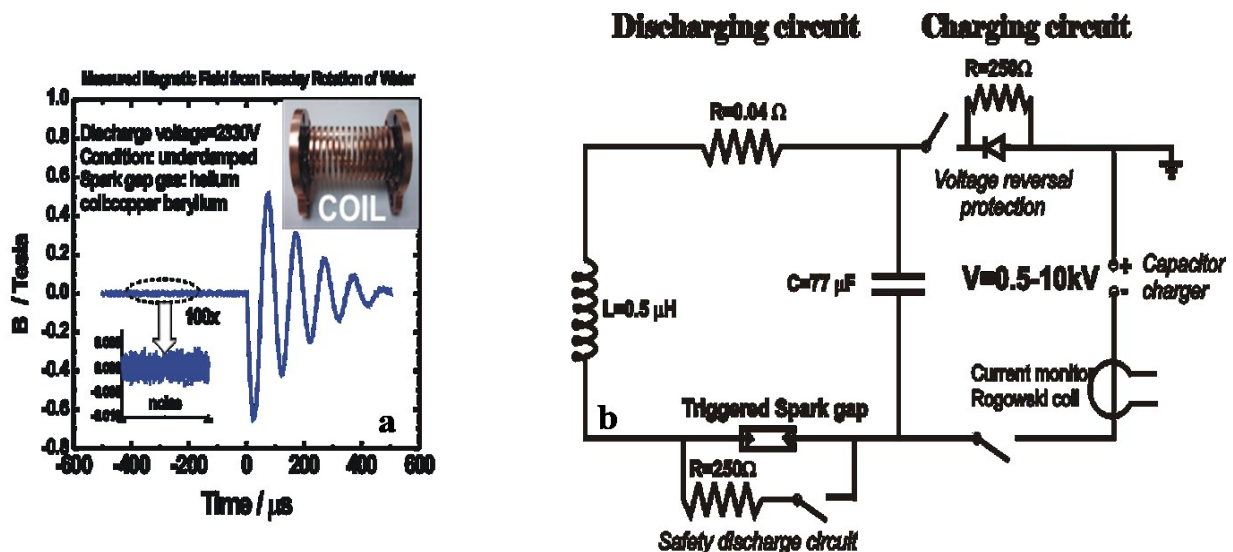
Figure B.1 LEFT Experimentally measured magnetic field of the pulsed magnet from a single shot of the Faraday rotation of water at 632 nm, INSET The picture of the helical copper beryllium coil manufactured at KSU, RIGHT Simplified electronic description of the pulsed magnetic field apparatus.

Safety concerns of pulsed magnets

1. **High Voltage:** The pulsed magnet utilizes a high voltage discharge capacitor that can store significant amount of energy. The capacitor can store energy as much $E=1/2CV^2$ where the C is the capacitance (77 μF) of the capacitor and V is the voltage (up to 10000 V in our case). **The energy stored in the capacitor is deadly to humans if the capacitor is discharged through the human body! Therefore it is very important to follow the safety steps to protect human life! High voltage electricity travels outside the cables, therefore it is important not to touch the electrical cables when the magnet operates.**

2. **Strong magnetic Field:** Magnetic fields can be dangerous to humans as well, especially to people who have peacemaker or medical implants. The magnet can produce up to 8 Tesla magnetic fields in close proximity, but it rapidly decreases I field strength away from the magnet. The magnet should not be operated when a person is present with a peacemaker. The operator should confirm with visitors, students etc. present if they have a peacemaker or similar electronic medical device.

3. **Mechanical failure of the magnet! The actual magnet is protected by a blast shield.**

4. **Induced transient currents in sensitive electronics!** The operating electronics is isolated from the electronics of the magnet. However, any new electronic equipment intended to be hooked up to in the vicinity of the magnet should be carefully considered!

5. **Loud noise!** The discharge of the magnet could produce very loud noise every 20 s, therefore the magnet should not be operated with the spark gap box being open (box reduces noise levels)!
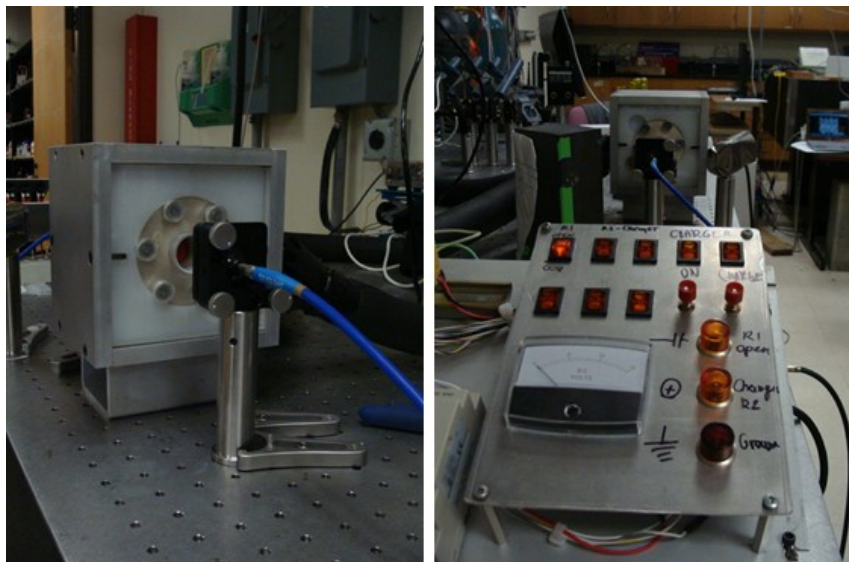
Figure B.2 LEFT Image of the magnet with the blast shield. RIGHT Control board of the magnet. The magnet is control with a single switch (LED light is on) on top left corner of the board

Operating instructions:

Turning on the magnet

Make sure all the knobs of controller board are in off position before doing anything.

1. Short the capacitor with the discharge bar!

2. Plug the high voltage trigger power supply in!

3. Turn the high voltage trigger gap receiver on!

4. Plug the high voltage fiber optic transmitter in!

5. Turn on (pull) the red button of controller board switch!

6. Turn both delay generators on!

7. Turn the voltmeter on!

8. Plug the high voltage power supply to the capacitor in!

Operating procedure

1. Turn the pulsed magnet on with the 1st switch of controller board (use high voltage glove)!

Pulsed magnet is now running indicated by the blinking light in the magnet controller board; don't touch anything on the table!

Turning off

1. Turn the pulsed magnet off when lights on the controller board are off by turning off the 1st switch of the controller board!

2. Unplug the high voltage trigger power supply!

3. Turn the high voltage trigger gap receiver off!

4. Unplug the high voltage fiber optic transmitter!

5. Turn off (push) the red button of controller board switch!

6. Turn both delay generators off!

7. Turn the voltmeter off!

8. Unplug the high voltage power supply to the capacitor!

9. Short the capacitor with the discharge bar!

Emergency stop

Push down the large red button on the controller board.

Safety Rules:

1. The capacitor must be discharged before and after operation with a discharge bar!

2. Even though the optical table is grounded; no metal parts should be touched during operation.

3. Stay at least 8 feet away from table, magnet and capacitor during operation.

4. Wear safety glasses at all times!

5. To start and stop the magnet, use the insulating gloves (rate 15000 V)!

6. During the operation, there are two snaps (high voltage trigger pulse) can be heard 4 seconds apart. After the second snap there is a 10 second break when all the lights are off on the control board of the magnet! This is the best time to stop the operation of the magnet!

7. In case of emergency push the red emergency button left of the control board! Disconnect all electrical power to the magnet (charger, trigger electronics etc.) and discharge the capacitor, before you investigate the emergency!

8. Alert other people in the lab when you start operating the magnet. Make sure they are at least 15 feet away during operation!

9. When visitors enter the lab, verify that no one with a pacemaker or medical implant is present when the pulsed magnet is turned on!

10. Do not remove the blast shield from the instrument!

11. Never leave the room while the instrument is running and make sure it is completely turned off and discharged before leaving!

Appendix C - Calculating the field strength of pulsed magnet

This calculation is for the magnetic field generated when discharge potential is 5000V and pathlength is 2.6 cm. All the calculations depend on the user manual provided by the manufacturer of the large-area balanced photoreceiver (New Focus).

To calculate the field strength of pulsed magnetic field, a large-area balanced photoreceicer is used. According to the user manual of the phtodetector, the large area of the photodetector makes it easy to couple light from a variety of sources (including diode lasers, broadband sources, and light from optical fibers) onto the detector without requiring precise optical alignment or focusing.

P_{in} and P_{out} are the input optical powers in Watts on the right and left photodiodes respectively, with equal amplitude but are out of phase by 90°. When magnetic pulsed is generated, the output powers will be changed to P'_{in} and P'_{out} because of the change in rotation of polarization of light as shown in following figure. The resultant vector P will never change ($P = P'$), only rotates. The symbol φ represents the rotation of P which is the Faraday rotation.
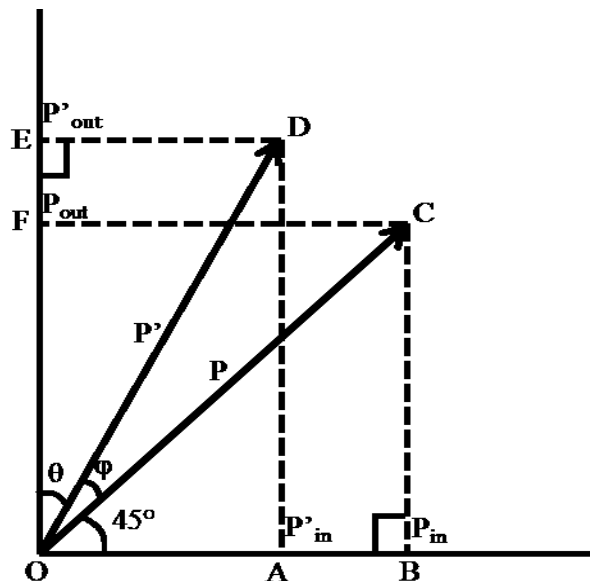
Figure C.1 A schematic representation of input, output optical power on the right and left photodiodes with resultant optical power.

To calculate the approximate output voltage for a given input optical power uses the relationship;

$$V_{out} = (P'_{in} - P'_{out}).R.G \tag{1}$$

, where P_{in} and P_{out} are the input optical powers in Watts on the right and left photodiodes respectively, R is the photodetector's responsivity (A/W), and G is the amplifier's trans-impedance gain (V/A).

Here, $P_{in} = 272\ \mu W$ $\qquad$ $P_{out} = 272\ \mu W$

$R = 0.36$ A/W $\qquad$ $G = 10^5$ V/A

$V_{out} = 0.08$ V, which is the amplitude of the pulsed.

Now,

Before the application of magnetic field,

$$P_{in}^2 + P_{out}^2 = P^2 \tag{2}$$

$$\therefore P^2 = (272 \times 10^{-6})^2 + (272 \times 10^{-6})^2 = 1.5016 \times 10^{-7}$$

After the application of magnetic field,

Equation (1) can be written as;

$$P'^2_{in} - P'^2_{out} = \frac{V_{out}}{R.G} \tag{3}$$

$$P'^2_{in} - P'^2_{out} = \frac{0.08}{2 \times 10^3 \times 0.4} = 1 \times 10^{-4} \tag{4}$$

And equation (2) can be written as;

$$P'^2_{in} + P'^2_{out} = P^2 \tag{5}$$

$$\therefore P'^2_{in} + P'^2_{out} = 1.5016 \times 10^{-7} \tag{6}$$

After solving equations (4) and (6), the values of P'_{in} and P'_{out} are obtained, which are;

$$P'_{in} = 0.2194 \times 10^{-3} = OE$$

$$P'_{out} = 0.3194 \times 10^{-3} = OA$$

Now, from ΔODE

$$\angle\text{ODE} = tan^{-1}\frac{OE}{DE} = tan^{-1}\frac{0.2194\times10^{-3}}{0.3194\times10^{-3}} = 55.51^\circ$$

Then,

$$\theta = 180^\circ - 45^\circ - 55.51^\circ = 34.49^\circ$$

Hence,

$$\varphi = 90^\circ - 45^\circ - 34.49^\circ = 10.51^\circ = 630.599 \, min.$$

Now, the magnetic field is given by;

$$B = \frac{\varphi}{vl},$$

, where v and l are Verdet constant of water and l is the path length of the medium.

$$= \frac{630.599}{0.0115\times2.6} = 21900.26 \, Gauss = 2.2 \, Tesla$$

The same calculation is repeated for the other measurement of magnetic field when 3500V discharge potential and 3.0 cm path length are used. The calculation ended up with 1.2 Tesla of pulsed magnetic field.

Appendix D - Programs used to analyze data

Following MatLab programs are used to analyze the data.

To analyze pulsed recorded on oscilloscope

```matlab
 function [x y] = pulsed()
%UNTITLED1 Summary of this function goes here
%   Detailed explanation goes here
%open the current file
file='00';
str1='C:\Documents and Settings\Viktor Chikan\My Documents\Data\newpulsed\';
str2=['C1wt000' file '.txt'];
str3=['C2wt000' file '.txt'];
str4=['C3wt000' file '.txt'];
str5=['F1wt000' file '.txt'];
file1=[str1 str2];
file2=[str1 str3];
file3=[str1 str4];
file4=[str1 str5];
laserpower=1;


%%%%%%%%%%%%%%%%%%%%%%%%%
%1st file
%%%%%%%%%%%%%%%%%%%%%%%%%

    fid= fopen(file2);
     %error check
    if fid == -1
        error('Data file cannot be open - ERROR!')
    end
    %move position to beginning of matrix, skipping the first two lines
    line1=fgetl(fid);

    %error check
    if (line1==-1)
      error('Error reading first line of data file.')
    end

    line2= fgetl(fid);

    %error check
    if (line2==-1)
      error('Error reading second line of data file.')
    end

        line3= fgetl(fid);

    %error check
    if (line3==-1)
      error('Error reading second line of data file.')
    end
```

```matlab
        line4= fgetl(fid);

    %error check
    if (line4==-1)
      error('Error reading second line of data file.')
    end
        line5= fgetl(fid);

    %error check
    if (line5==-1)
      error('Error reading second line of data file.')
    end

data1=[];
%%then read what you want
data1 = fscanf(fid, '%g %g',[2 inf]);

data1=data1';
%close file

fclose(fid);
%smooting the data

sdata1 = smooth(data1(:,2),30);
%removing zero
offset1=mean(sdata1(1:1000));
sdata1=sdata1-offset1;
%min1=min(sdata1)
%sdata1=sdata1/abs(min1);

%%%%%%%%%%%%%%%%%%%%%%%%%
%2nd file
%%%%%%%%%%%%%%%%%%%%%%%%%
    fid= fopen(file3);
     %error check
    if fid == -1
        error('Data file cannot be open - ERROR!')
    end
    %move position to beginning of matrix, skipping the first two lines
    line1=fgetl(fid);

    %error check
    if (line1==-1)
      error('Error reading first line of data file.')
    end

    line2= fgetl(fid);

    %error check
    if (line2==-1)
      error('Error reading second line of data file.')
    end

        line3= fgetl(fid);
```

183

```matlab
    %error check
    if (line3==-1)
      error('Error reading second line of data file.')
    end
        line4= fgetl(fid);

    %error check
    if (line4==-1)
      error('Error reading second line of data file.')
    end
        line5= fgetl(fid);

    %error check
    if (line5==-1)
      error('Error reading second line of data file.')
    end


data2=[];
%%then read what you want
data2 = fscanf(fid, '%g %g',[2 inf]);

data2=data2';
%close file

fclose(fid);
%smooting the data

sdata2 = smooth(data2(:,2),400);
%removing zero
offset2=mean(sdata2(1:1000));
sdata2=sdata2-offset2;
min2=min(sdata2);
%sdata1=sdata1/abs(min2);
sdata1=sdata1/laserpower;

vector=1:100:size(data1(:,1));
x=data1(vector,1);
y=sdata1(vector);
plot(x,y);


end
```

To analyze the signal of Faraday rotation

```matlab
function [] = signal( input_args )
%UNTITLED1 Summary of this function goes here
%  Detailed explanation goes here
str1='C:\Documents and Settings\Viktor Chikan\My Documents\Data\gold coate
Fe2O3 pusled faraday rotation\';
```

184

```matlab
file='C2wt00019';
str2=[file '.txt'];
file1=[str1 str2];
laserpower=130;%microwatt

fid= fopen(file1);
     %error check
     if fid == -1
         error('Data file cannot be open - ERROR!')
     end
     %move position to beginning of matrix, skipping the first two lines
     line1=fgetl(fid);

     %error check
     if (line1==-1)
       error('Error reading first line of data file.')
     end

     line2= fgetl(fid);

     %error check
     if (line2==-1)
       error('Error reading second line of data file.')
     end

         line3= fgetl(fid);

     %error check
     if (line3==-1)
       error('Error reading second line of data file.')
     end
         line4= fgetl(fid);

     %error check
     if (line4==-1)
       error('Error reading second line of data file.')
     end
         line5= fgetl(fid);

     %error check
     if (line5==-1)
       error('Error reading second line of data file.')
     end

data1=[];
%%then read what you want
data1 = fscanf(fid, '%g %g',[2 inf]);

data1=data1';
%close file

fclose(fid);
%smooting the data
sdata1 = smooth(data1(:,2),30);
```

```matlab
%removing zero
offset1=mean(sdata1(1:1000));
sdata1=sdata1-offset1;

vector=1:50:size(sdata1);
x=data1(vector,1);
y=sdata1(vector);
plot(x,y);
max(y)
y=y/max(y);
plot(x,y);
vector2=1:4000;
vector3=6000:10000;
fitx=[x(vector2); x(vector3)];
fity=[y(vector2); y(vector3)];
intery=interp1(fitx,fity,x);
y=y-intery;
plot(x,y);
max(y)
min(y)
```

To determine the area under the fluorescence peak

```matlab
function [ output_args ] = area( input_args )
%UNTITLED7 Summary of this function goes here
%   Detailed explanation goes here
str1='C:\Documents and Settings\Raj Kumar Dani\My Documents\lab
data\Liposome\DPPC\fe3o4 5hr\'
str2='LIPTRIT.prn';
file1=[str1 str2];
data=load(file1);
%plot(data(:,1),data(:,2));
X=data(:,1);
y=data(:,2);
Y=y-mean(y(end-100:end));
plot(X,Y);
area=trapz(X(1:263),Y(1:263))
end
```